

ABSTRACT

Title of Dissertation: ANALYZING TIME-VARYING
SEISMICITY AND AFTERSHOCK
BEHAVIOR IN CENTRAL AND EASTERN
UNITED STATES

Karen Melinda Pearson, Doctor of Philosophy,
2021

Dissertation directed by: Dr. Vedran Lekić, Department of Geology

Central and Eastern United States (CEUS) earthquakes are far less common than those in the tectonically active west coast, but the significance is elevated for a few reasons. Due to older, harder, and often denser rocks making up the bedrock geology east of the Rockies, seismic waves can travel much further without losing energy. Poor construction, efficient transmission of seismic waves, and site amplification effects can make even light to moderate earthquakes pose high risk within the CEUS. The CEUS has significant aging infrastructure and some of the highest population densities in the country, which would lead to great economic losses and even the potential for human injury if hazards are not properly identified and communicated.

Aftershock sequences are governed by several descriptive statistical “laws,” each with one or more characteristic parameters. These parameters are used to illustrate factors such as the overall productivity, the rate of decay, and the relative frequency of larger and smaller magnitude aftershocks. Variations in these parameters can relate

to the geologic region being studied, the tectonic environment, the driving force of seismicity (i.e. induced earthquakes, volcanic, or geothermal-related), and more.

This work discusses the aftershock sequences of two unusual CEUS earthquakes from the past five years. The first earthquake I study is a M4.2 earthquake that occurred east of Dover, DE, in late 2017. I continue by studying the aftershocks in the six weeks following a M5.8 earthquake that occurred near Pawnee, OK, in autumn 2016. Both of these earthquakes experienced below-normal aftershock productivities. I explore the challenges of analysis when station coverage is heterogeneous for the period of aftershock analysis. From there, I discuss the limitations of some statistical tests for special cases such as aftershock decay. The work concludes by highlighting additional CEUS earthquakes exceeding M4 that have occurred in the past 20 years and discussing some preliminary analytical findings.

ANALYZING TIME-VARYING SEISMICITY AND AFTERSHOCK
BEHAVIOR IN CENTRAL AND EASTERN UNITED STATES

by

Karen Melinda Pearson

Dissertation submitted to the Faculty of the Graduate School of the
University of Maryland, College Park, in partial fulfillment
of the requirements for the degree of
Doctor of Philosophy
2021

Advisory Committee:
Professor Vedran Lekić, Chair
Professor Mong-Han Huang
Professor Karen Prestegard
Dr. Lara Wagner
Professor Maria Cameron

© Copyright by
Karen Melinda Pearson
2021

Dedication

To Ved, whose patience and belief in me kept me going through family trauma, political turmoil, and a world health crisis.

Acknowledgements

My research was supported by the Packard Fellowship for Science and Technology, teaching assistantship from the Department of Geology, and most importantly by the Southern Regional Education Board Dissertation Fellowship. My travel for conferences was variously supported by the Earth System Science Interdisciplinary Center Travel Awards, Seismological Society of America Global Travel Grant, and Eastern Section Seismological Society of America Travel Grant.

Table of Contents

Dedication.....	ii
Acknowledgements.....	iii
Table of Contents.....	iv
List of Tables.....	vi
List of Figures.....	viii
List of Abbreviations.....	xiii
Chapter 1: Background: Intraplate Seismicity and Aftershocks.....	1
1. Central and Eastern United States Seismicity.....	1
2. Aftershock parameters.....	3
1. Gutenberg-Richter Law.....	3
2. Omori's Law and Omori-Utsu decay.....	5
3. Båth's Law.....	6
2. Stress drop.....	7
1. Stress drop modeling.....	7
2. Typical stress drops.....	9
3. Stress orientation relation to fault orientation.....	9
4. Introduction of this work.....	10
Chapter 2: November 2017 Delaware M4.2.....	12
1. Background.....	12
1. Introduction.....	12
2. Regional Geology and Tectonics.....	12
3. Regional Stress and Seismicity.....	14
4. Overview of Chapter 2.....	15
2. Data.....	16
3. Methods.....	19
1. Waveform cross-correlation for detection.....	19
2. Earthquake Locations.....	22
3. Source Parameters.....	25
3. Results.....	26
1. Aftershock Detection.....	26
2. Aftershock Locations.....	29
3. Aftershock Magnitudes.....	32
4. Stress Parameter Estimation.....	34
4. Discussion.....	37
1. Productivity.....	37
2. Potential Causes.....	40
5. Conclusions.....	42
Chapter 3: November 2016 M5.8, Pawnee, Oklahoma.....	44
1. Background.....	44
1. Enhanced Oil Recovery and hydrofracturing.....	44
2. Previous moderate magnitude earthquakes in Oklahoma.....	51
2. Introduction.....	51

1. Summary	51
2. Data	52
3. Methods.....	52
1. Waveform correlation	52
2. Location Search	57
3. Local magnitude determination	58
4. Results.....	59
1. Locations.....	59
2. Frequency-magnitude distributions	61
2. Aftershock decay	64
5. Discussion	66
6. Conclusions.....	68
Chapter 4: Determining Periodicity in Non-Homogeneous Catalogs.....	69
1. Introduction.....	69
2. Classic Periodicity Analysis	71
3. Expected $\ln(p)$ values of Schuster Test	76
4. Discussion.....	79
5. Conclusions.....	81
Chapter 5: Moderate Magnitude CEUS Earthquakes	82
1. Summary on other locations	82
1. 2015 Michigan M4.2.....	82
2. Highlights of all M4+ since 2000	82
2. Areas for future research.....	83
1. Aftershock statistical parameters (b, a, c, p).....	83
2. Waveform cross correlation to expand detection of aftershocks	84
3. Categorizing CEUS events	84
3. Conclusions.....	89
Appendix 1: Tables of P- and S-picks: M4.2 Delaware Aftershocks	90
Appendix 2: Bayesian Markov Chain Monte Carlo Algorithm.....	100
Appendix 3: Synthetic Catalog Generation	105
Appendix 4: Derivation of Expected Schuster $\ln(p)$ Value	107
References.....	119

List of Tables

Table 1.1: Summary of commonly-used coefficient k-values used for calculating stress drop, with their respective body wave spectra for use and the source of each.	9
Table 2.1: Locations of the local network stations with the end of service date. Station codes: DVB: compact broadband seismometer; DVN: 5 Hz nodal seismometer. Recordings began late on 1 December 2017; all times are in UTC. †DVB3 had a gap in data between 26 December 2017 07:58:26 and 08 January 2018 00:00:00.	18
Table 2.2: Velocity model used for determining aftershock locations and generating synthetics used for moment tensor inversion. The top two km are derived from Cunningham and Lekic receiver function modeling of crustal sediment at the nearest TA station and the basement layers are from Dreiling et al. (2017).	23
Table 2.3: Dates, times (UTC), epicentral locations, depths, and local magnitudes of 38 located aftershock events.	31
Table 2.4: Main shock corner frequencies for regional stations listed by distance to mainshock, with corresponding circular fault radius and stress drop estimate using k parameters for P-wave and S-wave (above and below heave line, respectively) from Kaneko and Shearer (2014) and the moment derived by Kim et al (2018) (2.6e15 Nm). The shear wave velocity used was 3.46 km/s (Table 2.2). LD: Lamont-Doherty Cooperative Seismographic Network, PE: Pennsylvania State Seismic Network.	35
Table 2.5: Mean and 95% confidence interval ($\pm 2\sigma$) for the ensemble of model solutions for parameters {a, b, p}, compared with results from Page et al. (2016) and Ebel (2009).	38
Table 3.1: Fraction of day each local network station was operational for the duration of the temporary deployment. Total fraction of the array operational per day is calculated by summing the proportion of operational time for all 16 stations on a day and dividing by 16. Numbers in bold are stations that were operational for less than 90% of a day. In the last column, numbers in bold indicate days with less than 60% of the array time operational, approximately equal to fewer than 10 out of 16 stations operating.	53
Table 3.2: Crustal velocity model for central Oklahoma.	58
Table 3.3: Mean and 95% confidence interval for the ensemble solution for parameters {a, b, p}. Left column is solution including all detected aftershocks; right column excludes those detected and located on the grid search boundary (Figure 3.5).	66

Table 5.1: Magnitudes and hypocentral locations of 25 CEUS earthquakes plotted in Figure 5.1, excluding M4+ aftershocks of larger events in this list, as well as the Guy-Greenbrier, AR, sequence and the 2017 Delaware earthquake (previously analyzed). Shaded events are in duplicate regions and would serve to improve understanding and resolve bounds on aftershock parameters, but studies of the first 14 events to encompass a wide variety of regions are recommended first. 87

Table 5.2: CEUS earthquakes with $M \geq 0$ since 2010, shown with respective depth, magnitude, largest aftershock magnitude, and number of aftershocks in ComCat. 88

List of Figures

- Figure 1.1: “Did You Feel It?” data from four U.S. earthquakes in the past decade shows how comparable magnitudes are felt over a much broader area in the CEUS, with a M5.8 in Virginia felt up to 600 miles away compared to a M6.0 in California felt only to about 250 miles, despite it having released around twice as much energy with the difference in magnitude. In contrast, a M4.1 earthquake in Delaware was felt approximately 200 miles from the epicenter, close to that of the California earthquake, even though the California event released 700 times as much energy (Pratt & Fitzpatrick, 2018). Figure by Jones (2018). 2
- Figure 1.2: Frequency-magnitude distribution of CEUS earthquakes 2001-2020 in the ComCat catalog (Various, 2021). The best-fit Gutenberg-Richter relation has a b -value of 1.01 and shows that the magnitude of completeness is $M_C \cong 2$ 3
- Figure 2.1: Geologic terrane map of the Mid-Atlantic region of the United States with historic seismicity, regional stations, and local temporary stations. Permanent regional 3-component stations at the time of the 2017 Delaware earthquake are shown with black squares. Temporary nodal seismometers are shown with filled red triangles and temporary broadband seismometers are shown with filled dark gray triangles. White circles indicate the locations of all M3+ earthquakes in ComCat since 1980, scaled by magnitude. The epicenter of the 30 November 2017 earthquake is a green circle. In Delaware (DE), the green is the Carolina Superterrane, gold is the Brunswick terrane, and black shows the extent of Pangaeon rifting. Terranes from Hatcher Jr. et al. (Hatcher Jr. et al., 2007). Historic seismicity from ComCat (Various, 2021). 13
- Figure 2.2: Local portable seismographic station deployment from 1 December 2017 – 11 January 2018. Stations with broadband sensors are plotted by white triangles and designated “DVB”; short-period sensors (nodals) are plotted by red triangles and designated “DVN”. The epicenter of the 30 November 2017 earthquake is a magenta circle. The red box indicates the region where aftershocks were detected and the borders of the map shown in Figure 4. Note the coast includes significant tidal wetlands and so the sea level topography does not exactly align with marked state boundaries (black). 17

Figure 2.3: Local station waveforms by distance from event. Event-to-station distance is given for each station at the start of the trace. The pattern of P, sP, and S arrivals (short gray lines) is exhibited on each station, with the best visibility on the nearer stations. The time between sP and S is nearly constant for all distances and the time between P and sP lengthens with distance, supporting the interpretation of an S-wave converting to a P-wave at the sediment layer. The continuous gray line indicates the event origin time. Some marked arrivals are estimated and not used for location determination (Appendix 1). Amplitudes for each station are normalized to the maximum recorded for the respective station. 21

Figure 2.4: Waveforms for the five template events at station DVB2, the station nearest to the mainshock, showing transverse in black, radial in blue, and vertical in red. All amplitudes are scaled to the maximum for each event, which may be either vertical or horizontal. Each event is aligned to have the P-arrival at time 0; the sP converted wave arrival is clear on the vertical channel for each of the five templates at approximately time 0.25 seconds. Each phase arrival is marked in gray; arrivals are slightly different for each template due to different source locations. Amplitudes for each aftershock are normalized to the maximum recorded for the respective event. 27

Figure 2.5: Predicted travel times curves (solid lines) for an earthquake at the location and depth of the 17 December 2017 14:58 M_L 1.4 aftershock, shown with measured phase arrival times for that event (open markers). The thinning of the sediment layer of the ACP getting further from the coast shows up in the closer spacing between the black (diamond) and red (circle) observations for the SP and S phase arrivals, as the sediment layer is thinner further west (see Figure 2.2 and Figure 2.3 for station location reference). 28

Figure 2.6: Locations of aftershocks. Shading corresponds to depth of the event, with magenta corresponding to the shallowest events (0.5 km) and yellow corresponding to the deepest event (6.5 km). Size of the marker is proportional to event local magnitude; see key for scale. Diamond-shaped markers indicate the events used as templates for aftershock detection and are shown with their one-sigma horizontal error contour. The approximate proposed fault is drawn in blue. The mainshock had an approximate depth of 3 km (Kim et al. 2018). Only the two nearest stations of the local deployment are visible in this projection; see Figure 2.2 for context of location in Delaware. 30

Figure 2.7: Gutenberg-Richter relation showing relative frequency versus magnitude of located aftershocks during the deployment period of the local network. Local magnitudes are calculated using Kim (1998) formula for ENA. The best-fit least-squares model is $\log(N)=1.57-0.94m$, with the shaded region indicating the 95% confidence of the fit. 32

Figure 2.8: Gutenberg-Richter relation showing relative frequency versus magnitude of all detected aftershocks during the deployment period of the local network. Local magnitudes are calculated using Kim (1998) formula for ENA. The best-fit least-squares model is $\log(N)=1.68-1.03m$, with the shaded region indicating the 95% confidence of the fit. 34

Figure 2.9: (a) Brune model fit to mainshock (“MS”) P-wave spectral power (solid lines) and $M_L 1.6$ aftershock (“AQ”) on 17 December 14:58 (dashed lines) at station GEDE. For both events, blue is east, red is north, and green is vertical channel data. Noise windows prior to each event are in gray. (b) Mainshock spectral power to aftershock spectral power ratio is shown in solid black. The best-fit spectral ratio model using these two events is fit in red. Thin gray lines indicate the two corner frequencies. (c) The spectral ratio tradeoff between mainshock and aftershock corner frequencies for the optimal coefficient a 36

Figure 2.10: a-d) Histograms showing the distribution of values for each parameter in the ensemble of model solutions for the rate equation. 39

Figure 2.11: Tradeoffs between each pair of parameters. Although b does not have as defined a distribution as a , the two share a strong correlation. Parameters a and p are individually better defined (Figure 2.10) but only have a slight correlation. . 39

Figure 3.1: Primary energy production in the US since 1950. NGPL: Natural gas plant liquids..... 45

Figure 3.2: Count of earthquakes above the magnitude of completeness ($M_{3.0}$) in Oklahoma by year. 49

Figure 3.3: Oklahoma geologic provinces with known faults and seismicity $M_{3.0}$ and greater prior to 2007 (red) and after 2008 (blue). Magnitude $M \geq 5$ earthquakes are shown in yellow with the $M_{5.8}$ Pawnee event depicted with a star. Clockwise from west: Fairview ($M_{5.1}$), Cushing ($M_{5.0}$), and Prague ($M_{5.7}$). Faults from USGS (mrdata.usgs.gov). Geologic model from Whitmeyer and Karlstrom (2007)..... 49

Figure 3.4: Map of detected aftershocks for the $M_{5.8}$ Pawnee earthquake. The mainshock is shown with a yellow star. Stations are shown as red inverted triangles. Aftershocks used as template events are shown with large blue circles. The shading reflects the density of detected events in an area on the map; thus, the magenta region in the center has the largest concentration of aftershocks. The bounds of the grid used for location search are evident from earthquakes with locations placed on the outer edges. These events are likely located at greater distances in truth..... 60

Figure 3.5: Frequency-magnitude distribution of detected aftershocks to the $M_{5.8}$ Pawnee earthquake in November 2016..... 61

Figure 3.6: Histogram of aftershock time of day in UTC (top) and local time (bottom) for all aftershocks detected on at least 4 stations in the 33-day deployment. 63

Figure 3.7: FMD for local night (black diamonds) and local day (red squares). Both have $M_c=0.2$, but the night time figure shows slightly higher detections for $M<0$ and for $2.2<M<3.2$ 64

Figure 3.8: Daily count of detected aftershocks per broadband station (colored markers) and scaled (see text) daily count of aftershocks detected on at least 4 stations (black markers). The daily count of aftershocks detected at ≥ 4 stations is smoothed by the scaling to account for nonoperational stations and stations with partial days of operation, such as stations OK044, OK050, and OK051 on day 25 of the deployment. The raw counts for these three stations appears low on day 25 reflecting the data gap that prohibited detection for much of the day. 65

Figure 4.1: Example histograms of phase angle distributions for (a) non-periodic and (b) periodic synthetic catalogs. The non-periodic catalog has approximately equal distribution of phase angles for events and the net random walk will end near the origin. The periodic catalog has a bias toward a phase angle of $11\pi/6$ radians, resulting in the net random walk from all events ending some distance from the origin in that direction. 72

Figure 4.2: A synthetic catalog with a homogenous Poisson process earthquake rate has no significant periodicities detected at any period tested. The catalog has no background rate change and no periodic signature. 74

Figure 4.3: A synthetic catalog with an exponentially increasing background earthquake rate has numerous significant periodicities detected for long periods, despite known random non-periodic generation of event times. 75

Figure 4.4: Sample $eln p$ for different event rates. The rates of growth for the linear event rate, α , and the exponential event rate, β , are fixed for each given synthetic data set. Values for these parameters are for demonstration purposes, as is the selection of a sinusoid at $T=80$ days. All four synthetic catalogs are generated with the same number of events, N . The driver to the growth in $E[\ln(p)]$ is therefore the period being tested, T (equations 5.7 and 5.9). 79

Figure 5.1: $M \geq 4$ earthquakes in the Eastern US and Canada from 2001-2020 (Various, 2021). Size of marker is proportional to magnitude of event, with cyan circles showing $M5$ and greater events and blue squares showing $4 \leq M < 5$ events. Inverted triangles show 3-component network stations within 2 degrees of earthquakes selected for template matching analysis. Shading on the map indicates the 2% probability of exceedance in 50 years peak ground accelerations for site class D from the National Hazard model (Rukstales & Petersen, 2019). Full names of region abbreviations appear in Table 3. 85

Figure A2.1: Flowchart of MCMC algorithm..... 104

Figure A3.1: Comparison of means and standard deviations observed in simulated linearly increasing catalogs with those derived analytically and calculated for the applicable period and catalog length tested. The “zig-zag” feature seen here is an artifact of the event times included fitting to include only an integer number of cycles of T for each period tested. Therefore, as the catalog becomes long enough such that $\text{mod}(t/T)$ fits another complete cycle, the endpoint Y of the random walk becomes more predictable..... 112

Figure A3.2: Comparison of means and standard deviations observed in simulated exponentially increasing catalogs with those derived analytically and calculated for the applicable period and catalog length tested. 115

List of Abbreviations

1D	1 dimensional
ACP	Atlantic Coastal Plain
BTU	British Thermal Units
CA	California
CEUS	Central and Eastern United States
CI	Confidence Interval
ComCat	Comprehensive Earthquake Catalog
CVSZ	Central Virginia Seismic Zone
DE	Delaware
Delmarva	Delaware-Maryland-Virginia [peninsula east of Chesapeake Bay]
E	East
ENA	Eastern North America
ENE	East-northeast
f_0	Fundamental frequency
f_c	Corner frequency
FMD	Frequency-Magnitude Distribution
GR	Gutenberg-Richter [Law]
Hz	Hertz
km	kilometers
m	meters
m/My	meters per million years
M	Magnitude
M ₀	Moment
M _c	Magnitude of completeness
M _L	Local Magnitude
M _w	Moment Magnitude
MCMC	Markov Chain Monte Carlo

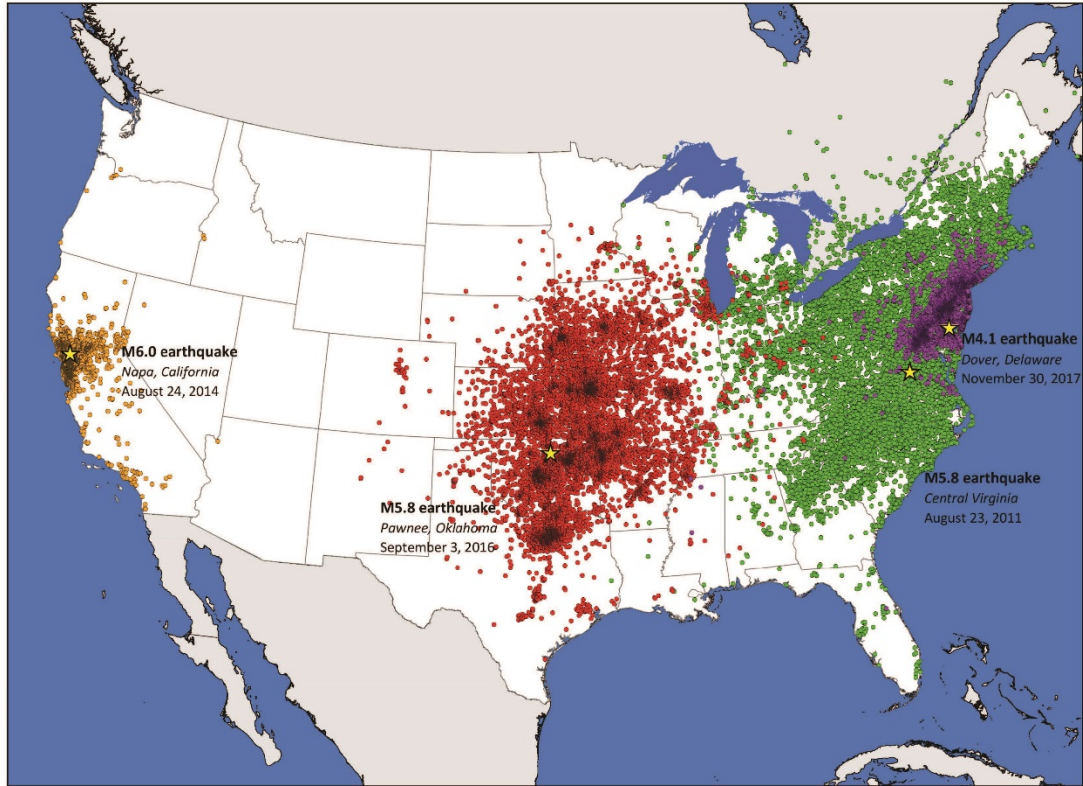
MD	Maryland
MI	Michigan
MPa	Mega Pascal
NE	Northeast
NNE	North-northeast
NJ	New Jersey
P-wave	compressional wave
S-wave	shear wave
SCR	Stable Continental Region
sP	S-to-P converted wave phase
SSW	South-southwest
SW	Southwest
W	West
WSW	West-southwest
TA	Transportable Array
USGS	United States Geological Survey
U.S.	United States
V_s	Shear wave velocity
V_p	Compressional wave velocity
VA	Virginia

Chapter 1: Background: Intraplate Seismicity and Aftershocks

1. Central and Eastern United States Seismicity

Although intraplate Central and Eastern United States (CEUS) earthquakes are far less common than those in the tectonically active west coast and Alaska, the significance is elevated for a few reasons. Due to older, harder, and often denser rocks making up the bedrock geology east of the Rockies, seismic waves can travel much further without losing energy (Pratt & Fitzpatrick, 2018). This results in earthquakes of similar magnitudes being felt at significantly greater distances for the CEUS (Figure 1.1; Pratt & Fitzpatrick, 2018).

Poor construction, efficient transmission of seismic waves, and site amplification effects can make even light to moderate earthquakes pose high risk within the CEUS (Hough, 2012; Pratt et al., 2017). The aftershocks of these earthquakes can be particularly hazardous because they occur while response efforts for the mainshock are underway. Furthermore, structures may be damaged from the mainshock and suffer additional damage during aftershocks (Reasenberg & Jones, 1989). The CEUS has significant aging infrastructure and some of the highest population densities in the country (“Gridded Population of the World, Version 4 (GPWv4): Population Density, Revision 11,” 2018; Nagarajaiah & Erazo, 2016), which would lead to great economic losses and even the potential for human injury if hazards are not properly identified and communicated.



U.S. Department of the Interior
U.S. Geological Survey

Figure 1.1: “Did You Feel It?” data from four U.S. earthquakes in the past decade shows how comparable magnitudes are felt over a much broader area in the CEUS, with a M5.8 in Virginia felt up to 600 miles away compared to a M6.0 in California felt only to about 250 miles, despite it having released around twice as much energy with the difference in magnitude. In contrast, a M4.1¹ earthquake in Delaware was felt approximately 200 miles from the epicenter, close to that of the California earthquake, even though the California event released 700 times as much energy (Pratt & Fitzpatrick, 2018). Figure by Jones (2018).

¹ The USGS-reported moment magnitude for the Dover, DE, is M4.1. Later work by Kim et al. (2018) determined a moment magnitude of M4.2, and magnitude M4.2 shall be used through the duration of this work.

2. Aftershock parameters

1. Gutenberg-Richter Law

Earthquakes and their aftershocks have a few basic governing statistical properties that have been well-recognized for many decades. The Gutenberg-Richter relationship describes the distribution of different magnitude earthquakes within a given region over a certain period of time (Gutenberg & Richter, 1944). This relationship, written as $\log_{10} N(\geq m) = a - bm$ shows that the log of the cumulative number of earthquakes greater than a given magnitude versus magnitude has a linear relation (Figure 1.2). In this formulation, a models the overall productivity of an aftershock sequence and b models the relative frequency of larger or smaller magnitude aftershocks. The slope of this distribution is generally close to 1, known as the b -value (Gutenberg & Richter, 1944). A slope of 1 indicates that there are 10 times as many earthquakes for one unit decrease in magnitude.

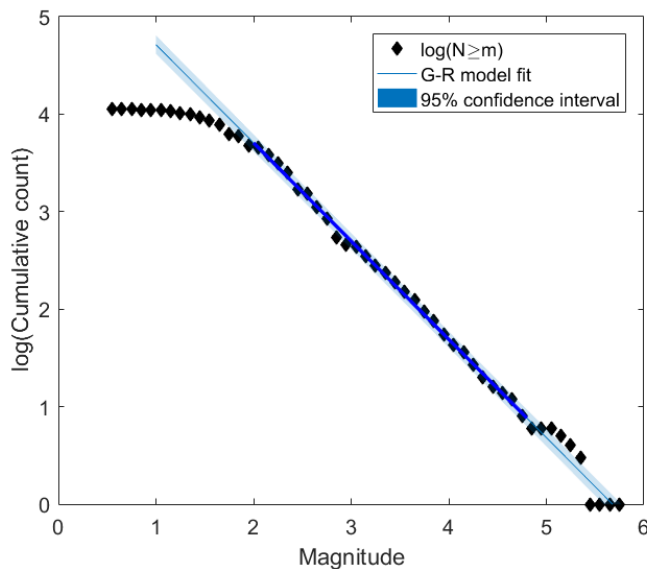


Figure 1.2: Frequency-magnitude distribution of CEUS earthquakes 2001-2020 in the ComCat catalog (Various, 2021). The best-fit Gutenberg-Richter relation has a b -value of 1.01 and shows that the magnitude of completeness is $M_C \cong 2$.

Because of limitations with the detection of earthquakes at both the high and low end of the magnitude scale, only a portion

of magnitudes will fit this relationship well. Large magnitude earthquakes are rare and regardless of the size of a region being studied or the duration of data collected, there will inevitably be statistical variability present in the counts for the largest magnitude earthquakes, whether the study is global and reaches to M9 or regional and peaks at M5 or M6. This variability is evident in Figure 1.2 between M5 and M6. On the other end of the scale, instrumental limitations prevent complete detection of the smallest earthquakes that occur at high frequency. This limitation is seen in Figure 1.2 where the count flattens from the linear relation for the smallest magnitudes.

The b -value of the GR distribution is one of the most commonly cited parameters for earthquakes. Variations in this value can relate to a region being studied, the tectonic environment, the driving force of seismicity (i.e. induced earthquakes, volcanic, or geothermal-related), and more (Goebel et al., 2019; Schorlemmer et al., 2005; Wiemer & Wyss, 2002). The most common method of estimating a population b -value is through the maximum likelihood estimator

$$\beta = \frac{1}{\frac{1}{N} \sum_{i=1}^N M_i - M_C} \quad 1.1$$

where N is the number of earthquakes in the catalog, M_C is the catalog magnitude of completeness, and M_i are the individual earthquake magnitudes (Aki, 1965). The estimator β is related to the GR b -value as

$$\beta = b \ln 10 \quad 1.2$$

or, through change of base,

$$b = \beta \log e \tag{1.3}$$

(Aki, 1965). Aki (1965) also showed that the confidence on the β value can be expressed as

$$\frac{1 - \frac{z}{\sqrt{N}}}{\frac{1}{N} \sum_{i=1}^N M_i - M_C} \leq \beta \leq \frac{1 + \frac{z}{\sqrt{N}}}{\frac{1}{N} \sum_{i=1}^N M_i - M_C} \tag{1.4}$$

where z is the z-score from standard normal distribution at the desired confidence level.

It has been shown that the estimator is more accurate when used on unrounded magnitudes, rather than those rounded to the nearest 0.1 magnitude units (or larger) (Nava et al., 2017). Similarly because the estimator and its confidence interval depend on the number of observations in a catalog, it will be more accurate to the true b-value for $N \geq 100$, with errors estimated to be up to 0.1 units with $N \approx 10$ (Nava et al., 2017).

2. Omori's Law and Omori-Utsu decay

The number of aftershocks was first found to decay with time since the mainshock as a hyperbolic following $1/t$ (Omori, 1895a). This decay relation was later refined by Utsu (1961) and is now known sometimes as the modified Omori's Law, the Omori-Utsu Law, or colloquially still as Omori's Law. Utsu expressed this modification as $n(t) = A(t + c)^{-p}$ where the exponent p governs the speed of decay and the constant c is a time offset from the time of the mainshock. Later researchers beginning with

Reasenberg and Jones (1989) modified the expression to clarify the coefficient A , such that the number of aftershocks changes with time as

$$\lambda(t, M_{min}) = 10^{a+b(M_{main}-M_{min})}(t+c)^{-p} \quad 1.5$$

This gives the rate of aftershocks with magnitude M_{min} or higher for a mainshock with magnitude M_{main} . The additional parameters a and b follow from the Gutenberg-Richter frequency-magnitude distribution for the aftershocks. In this formulation, M_{min} is often taken to be the magnitude of completeness for detection of a sequence, but it could also be used to consider the rate of aftershocks above any specified magnitude of interest, such as felt earthquakes ($\sim M2.5$) or earthquakes that may cause damage ($\sim M4$).

We use a Bayesian Markov Chain Monte Carlo approach to jointly invert for the log-likelihood of the parameters a , b , c , and p as

$$\log L(a, p) = \sum_{i=1}^N \log \lambda(t_i, M_{min}) - \int_{t_{beg}}^{t_{end}} \lambda(t, M_{min}) dt \quad 1.6$$

where t_{beg} and t_{end} are the beginning and end of the time period in which aftershocks are observed (Page et al., 2016).

3. Båth's Law

Båth's Law predicts that the difference between the main shock magnitude and the magnitude of the largest aftershock is near 1.2 magnitude units, regardless of mainshock magnitude (Båth, 1965; Richter, 1958). This relation has generally been

confirmed in numerous studies (e.g. Console et al., 2003; Felzer et al., 2002; Shcherbakov et al., 2005). These studies have covered areas including California and Nevada, Japan, Greece, and New Zealand, all of which are plate boundary or active tectonic regions, or they include global studies that are naturally dominated by the behavior of plate boundary earthquakes. Few studies have looked at the validity of Båth's Law for mainshocks with light to moderate magnitudes; most studies use M5 or M6 as a lower limit for inclusion.

Exceptions to Båth's Law have been noted for cluster-type sequences with multiple mainshock events (Console et al., 2003; Vere-Jones, 1969). A famous example of this in the CEUS is the 1811-12 New Madrid sequence of three earthquakes of M7.3-M7.5 over two months. These exceptions to Bath's Law, however, tend toward a smaller value of Δm than the typical 1.2 units, rather than larger.

2. Stress drop

1. Stress drop modeling

Earthquake modeling relies on an understanding of the stresses a system is subject to. In 1970, J. N. Brune developed a method to use seismic spectra to determine effective stress and stress drop, assuming a circular fault rupture (Brune, 1970). By finding the corner frequency of the source spectrum, the fault radius r as well as stress drop $\Delta\sigma$ can be estimated, using the following equations:

$$r = k\beta/f_c \quad 1.7$$

$$\Delta\sigma = \frac{7}{16} \left(\frac{f_c}{k\beta} \right)^3 M_0 \quad 1.8$$

where M_0 is the moment of the earthquake, β is the shear wave velocity, and k is a constant that varies depending on the particular model used (Brune, 1970; Shearer, 2009).

Various values for k have been presented, first by Brune (1970) and later by Madariaga (1976) and by Kaneko and Shearer (2014). For many years, the most commonly used values were those by Madariaga (1970) (Kaneko & Shearer, 2014; Shearer, 2009). Each of these coefficients was developed with slightly different modeling for the nature by which the rupture occurs. However, due to the fact that the $1/r$ term is cubed in equation 1.8, stress drop is sensitive to the model selected (Shearer, 2009). Stress drop is similarly sensitive to an accurate crustal velocity model at source depth, as that is also cubed. The shear wave velocity may be fixed to velocity at an average depth for a study of stress drops for multiple earthquakes within a region, or it may be chosen as V_s at the event depth for each earthquake (Sumy et al., 2017).

The corner frequency may be obtained from the spectrum of either a portion of the waveform around the P-wave arrival or the S-wave arrival and different k -values are presented for each of these cases. A summary of the different values for k for either P or S spectra for the different authors is presented in Table 1.1.

Spectrum used	k-value	Source
S-arrival	0.36	Brune (1970)
S-arrival	0.21	Madariaga (1976)
S-arrival	0.26	Kaneko & Shearer (2014)
P-arrival	0.32	Madariaga (1976)
P-arrival	0.38	Kaneko & Shearer (2014)

Table 1.1: Summary of commonly-used coefficient k-values used for calculating stress drop, with their respective body wave spectra for use and the source of each.

2. Typical stress drops

Typical stress drops for plate boundary earthquakes are usually around 5-10 MPa (Allmann & Shearer, 2007, 2009; Brune, 1970; Kanamori & Anderson, 1975).

Intraplate earthquakes usually have somewhat higher stress drops, around 10-20 MPa (Allmann & Shearer, 2009; Kanamori & Anderson, 1975; Scholz et al., 1985).

Studies have shown that high stress drop is linked to lower aftershock productivity (e.g. Wetzler et al., 2016).

3. Stress orientation relation to fault orientation

The optimal orientation of for fault failure is 30 degrees from the maximum horizontal stress direction. Faults oriented within ± 15 degrees from that optimal orientation are considered well-aligned for failure (Cochran et al., 2020). Other faults can fail, particularly with the influence of added fluid pressure, or those faults may slip aseismically (Cochran et al., 2020).

Hardebeck (2010) found that aftershock focal mechanisms generally align well with the background stress orientation. This indicated that the general stress field has predominance over aftershock occurrence. Small scale stress changes due to Coulomb failure, which can be heterogeneous over small distances, are less significant to the overall stress state. These smaller scale changes can affect the relative location of aftershocks, but aftershocks overall remain well-aligned with background stress (Hardebeck, 2010).

4. Introduction of this work

In this work I will investigate the aftershock sequences of two unusual CEUS earthquakes from the past five years. The first earthquake I study is a M4.2 earthquake that occurred east of Dover, DE, in late 2017 (Chapter 2:). For this event, I joined with University of Maryland and other colleagues to install a network of temporary three-component seismometers to record aftershock activity for approximately five weeks beginning the day after the mainshock. Although the mainshock was a light event, due to the CEUS geology it was felt from Washington, D.C., to New York City. It rapidly became evident, however, that this earthquake was not to be followed by any aftershocks of felt magnitudes.

In this study, we used data from the local network of seismometers to identify and locate a few dozen aftershocks in the month following the mainshock. None of these aftershocks exceeded a local magnitude 1.5. The investigation seeks to explore the ways in which this aftershock sequence fits with and violates expectations given by the

laws described in Section 2 of this chapter. In the conclusion of Chapter 2, I discuss possible reasons for this unusual behavior and the need for additional examples.

In Chapter 3: I continue by studying the aftershocks in the six weeks following a M5.8 earthquake that occurred near Pawnee, OK, in autumn 2016. Faculty and students at Cornell University led the deployment of several additional local additional local broadband seismic stations after this moderate earthquake. Using data from this deployment, I have identified and located several thousand small aftershocks. Contrary to Båth's Law (Section 1.3), this earthquake also had an unusually low maximum magnitude aftershock (McGarr & Barbour, 2017). Due to a slower station deployment compared to Delaware and other station heterogeneities, the analysis of aftershock parameters for this mainshock required a combined approach to study both network-wide detections and per-station detections.

Chapter 4: discusses the limitations of some statistical tests for special cases such as aftershock decay. Chapter 5: highlights additional CEUS earthquakes exceeding M4 that have occurred in the past 20 years and discusses some preliminary analytical findings.

Chapter 2: November 2017 Delaware M4.2

1. Background

1. Introduction

On 30 November 2017, a magnitude 4.2 earthquake occurred east of Delaware's capital city of Dover. The region has minimal historic seismicity (W. Kim et al., 2018; Stover & Coffman, 1993) and is in an intraplate location outside of known east coast seismic areas, 300 km from the Central Virginia Seismic Zone (CVSZ) and 750 km from the Eastern Tennessee Seismic Zone (Figure 2.1). This event's epicenter within the Salisbury Embayment of the Atlantic Coastal Plain (ACP) makes it unusual even among east coast earthquakes. Delaware and the Salisbury Embayment have no faults recorded in the USGS Quaternary fault database, and any earthquake that occurs in this region would be due to reactivation of historic faults.

2. Regional Geology and Tectonics

East-central Delaware is situated near the northeast end of the estimated extent of the Taylorsville Rift basin, part of the Newark Supergroup of rift basins. This half-graben strikes SW-NE and dips seaward, a result of Triassic rifting (Withjack et al., 1998). The normal faults during initial rifting of Pangaea shifted to reverse motion during the transition to drifting in the Early Jurassic (Withjack et al., 1998). The southern end of the Taylorsville Rift is exposed in the Piedmont region of central Virginia and

additional extent is inferred from borehole studies, water wells, and geophysical studies (LeTourneau, 2003; Olsson et al., 1988). Seismic surveying in Eastern Maryland to the southwest of the mainshock epicenter identified rift basin rocks dipping eastward to the

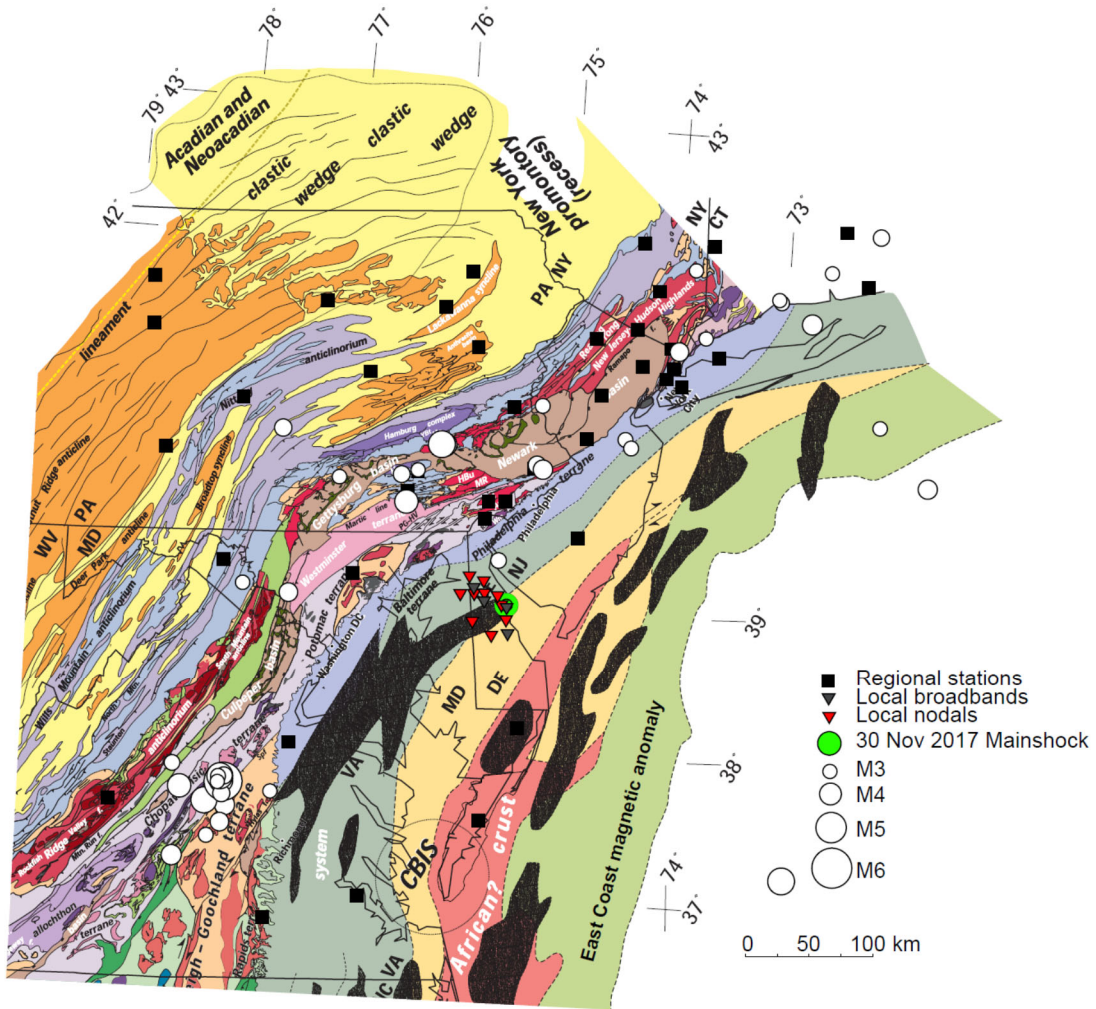


Figure 2.1: Geologic terrane map of the Mid-Atlantic region of the United States with historic seismicity, regional stations, and local temporary stations. Permanent regional 3-component stations at the time of the 2017 Delaware earthquake are shown with black squares. Temporary nodal seismometers are shown with filled red triangles and temporary broadband seismometers are shown with filled dark gray triangles. White circles indicate the locations of all M3+ earthquakes in ComCat since 1980, scaled by magnitude. The epicenter of the 30 November 2017 earthquake is a green circle. In Delaware (DE), the green is the Carolina Superterrane, gold is the Brunswick terrane, and black shows the extent of Pangaeian rifting. Terranes from Hatcher Jr. et al. (Hatcher Jr. et al., 2007). Historic seismicity from ComCat (Various, 2021).

east of the Chesapeake Bay (Hansen, 1988). A graben with a NNE strike was also identified about 50 km north of the mainshock location near Delaware City, DE (Spoljaric, 1973).

The strata infilling the Taylorsville Basin generally have three layers: a fluvial base, an intermediate lacustrine layer, and an upper layer of shallow lacustrine to fluvial sediments (Olsen, 1990). These strata form 50 m of siltstone interbedded with sandstone with evidence of bioturbation of sediments (Olsen, 1990; Pazzaglia & Gardner, 1994). These strata experienced an uplift of at least 2 km followed by erosion through the early Cretaceous (Withjack et al., 1998).

In the Mid-Atlantic region, the Piedmont is upwarping due to isostatic rebound from erosion while the ACP is subsiding from sedimentation at a rate of 10 m/My (Pazzaglia & Gardner, 1994). The flexural bend between these two regimes is at its steepest and narrowest in the Mid-Atlantic and contributes to the Appalachian Piedmont basement rocks of the Salisbury Embayment having a steeper dip than any other part of the ACP (Pazzaglia & Gardner, 1994).

3. Regional Stress and Seismicity

The maximum horizontal compressive forces in this area strike NE-SW (Heidbach et al., 2018; Withjack et al., 1998; Zoback & Zoback, 1989). This both follows the strike of rift structures such as the bounding faults of the Taylorsville basin and is consistent with the general stress across most of the Central and Eastern United States (CEUS), which exhibits a broadly uniform stress field in both magnitude and direction

(Heidbach et al., 2018; Zoback & Zoback, 1989). Because the North American plate lacks a subducting edge, the dominant driver of this stress likely comes from ridge push and/or basal drag; Zoback and Zoback argue that ridge push is the more likely cause of the stress field in the CEUS (1989).

Explanations for seismicity along the east coast of North America has been variably attributed to isostatic rebound from glacial retreat, continental denudation, sediment loading, thermal deformation, plate tectonic sources, crustal thickness variations, and more (see Gardner, 1989 and sources therein; Soto-Cordero et al., 2018). Faults are often attributed to preexisting crustal weakness or faults from pre-Quaternary ages (Gardner, 1989).

4. Overview of Chapter 2

The M4.2 mainshock on 30 November 2017 had only one aftershock identified by ComCat, occurring on 13 December 2017 at 00:45:27 with an estimated magnitude 1.3 (“Event Page M4.1 - 9km ENE of Dover, Delaware,” n.d.). Preliminary analysis using the regional network and reported in Kim et al. (2018) identified six aftershocks during the deployment period. Kim et al. (2018) additionally identified one small foreshock ten days prior to the main shock, one aftershock on 1 December 2017 before the temporary deployment was in place, and one additional aftershock on 2 February 2018 after the temporary local deployment was removed. The local magnitudes determined for these events ranged from $M_L0.9$ to $M_L1.9$.

In this paper, we analyze data from a temporary seismic network deployed to detect aftershocks of the 2017 M4.2 Delaware earthquake in order to identify how the aftershock behavior in the ACP province compares to typical parameters developed based on global tectonic models. We find low productivity overall with magnitudes consistent with those found by Kim et al. (2018). We see deviations from expected behavior in the low Gutenberg-Richter a -value and the unusually large magnitude difference between the mainshock and largest aftershock.

Various hypotheses have been proposed to explain variations in aftershock productivity. These include fault alignment with the prevailing stress field and low productivity after a high stress drop (Wetzler et al. 2016). We investigate these hypotheses in relation to the 2017 Delaware earthquake aftershocks and discuss which may be relevant factors for the lower-than-normal productivity observed.

2. Data

The nearest permanent seismic station (GEDE/LDSN) is 70 km from the epicenter of the main shock and only five stations are within 100 km (Figure 2.1). In order to enable detection of smaller magnitude aftershocks that would not register at those distances, personnel from the Department of Terrestrial Magnetism of the Carnegie Institution for Science, the Department of Geology of the University of Maryland, and the U.S. Geological Survey mobilized the day after the earthquake to install a temporary local network in the epicentral area using a mix of instruments. A total of 14 instruments were installed in central Delaware and eastern Maryland, covering an area approximately 40 km in diameter. We deployed the stations over a relatively broad area

for a moderate magnitude mainshock. This allowed for location uncertainty in the mainshock location and for no prior expectations on where aftershocks might be located, without defined faults known. The deployment remained in place until 11 January 2018. The temporary local stations that were deployed on 1 December 2017 are shown in detail in Figure 2.2.

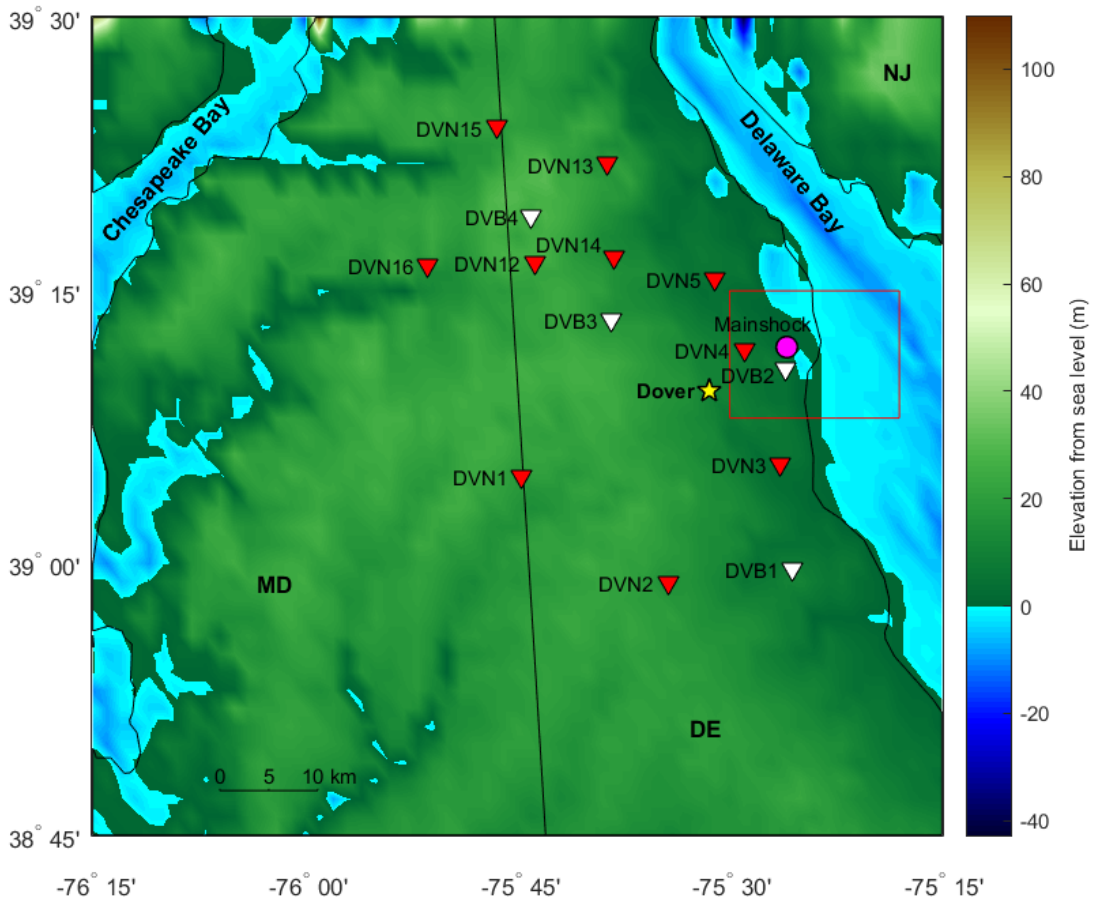


Figure 2.2: Local portable seismographic station deployment from 1 December 2017 – 11 January 2018. Stations with broadband sensors are plotted by white triangles and designated “DVB”; short-period sensors (nodals) are plotted by red triangles and designated “DVN”. The epicenter of the 30 November 2017 earthquake is a magenta circle. The red box indicates the region where aftershocks were detected and the borders of the map shown in Figure 4. Note the coast includes significant tidal wetlands and so the sea level topography does not exactly align with marked state boundaries (black).

Instrumentation included ten Fairfield Nodal ZLand nodes containing three-component 5 Hz geophones provided by the University of Maryland Department of Geology and four Nanometrics Trillium 120 Compact Posthole broadband seismometers provided by the Department of Terrestrial Magnetism of the Carnegie Institution for Science. Further details on the deployment are available in Kim et al. (2018). Three of the four solar powered compact broadbands, recording 200 samples per second, remained operational until the end of the deployment on 11 January 2018. The ten nodal seismometers, recording 100 samples per second, were battery operated, with a typical operational period of 36 days. Although temperatures in January 2018 were very cold, the batteries powering the nodes remained operational for 37-40 days; the exact end times for recording on each station are listed in Table 2.1.

Station	Latitude	Longitude	End of Recording
DVN1	39.08	-75.74	1/8/2018 23:12:00
DVN2	38.98	-75.57	1/8/2018 09:20:00
DVN3	39.09	-75.44	1/8/2018 21:16:00
DVN4	39.20	-75.48	1/8/2018 11:26:00
DVN5	39.26	-75.52	1/8/2018 14:10:00
DVN12	39.28	-75.73	1/9/2018 02:30:00
DVN13	39.37	-75.64	1/9/2018 11:46:00
DVN14	39.28	-75.64	1/10/2018 15:20:00
DVN15	39.40	-75.77	1/8/2018 07:50:00
DVN16	39.27	-75.86	1/8/2018 11:30:00
DVB1	38.99	-75.43	1/11/2018 21:18:19
DVB2	39.18	-75.43	1/11/2018 20:18:31
DVB3	39.22	-75.64	1/11/2018 18:55:34†
DVB4	39.32	-75.73	12/30/2017 06:31:37

Table 2.1: Locations of the local network stations with the end of service date. Station codes: DVB: compact broadband seismometer; DVN: 5 Hz nodal seismometer. Recordings began late on 1 December 2017; all times are in UTC. †DVB3 had a gap in data between 26 December 2017 07:58:26 and 08 January 2018 00:00:00.

3. Methods

1. Waveform cross-correlation for detection

We used a matched filter waveform correlation technique to identify aftershocks in data from the temporary deployment (Gibbons & Ringdal, 2006; Schaff & Waldhauser, 2010; Yoon et al., 2015). The largest of the aftershocks detected by Kim et al. (2018), an estimated $M_L 1.6$ on 17 December 2017 at 14:58, was selected as the initial template event.

Using the raw, uncorrected instrument data, we analyzed the power spectra on each instrument type for a period of 8 seconds before, during, and after our selected primary template event in order to ascertain the optimal filtering window, and found that the period during each aftershock event had elevated power between 4 and 40 Hz relative to non-event periods. We therefore used a bandpass filter at 4-40 Hz for raw data from each instrument type. We found the uncorrected waveforms to be more effective at template matching for the high frequency energy generated by the very small aftershocks we were detecting at close range.

The time series for each component (north, east, and vertical) were treated individually in this stage of analysis. We cut a 6-second template including the P- and S-arrivals from each of the three components of data for each station to use as our template waveform. Templates were correlated for each of the north, east, and vertical components against all available data from the deployment, and the algorithm required

two components from a station to have a positive match to be identified as an aftershock.

Thresholds for each component of data were determined by comparing the distribution of correlation coefficients obtained when correlating the time-reversed template with a day of data, with the distribution of coefficients obtained when correlating the forward, or original, template (Slinkard et al., 2014). In this method, the point at which divergence between the tails of the two distributions is observed is considered to be the threshold level for a satisfactory false alarm rate, by removing the false correlations due to noise (which can happen when correlating a waveform in either direction) but retaining the true correlated waveforms of events. Positive matches are therefore recorded whenever the correlation coefficient exceeds this threshold of divergence from the noise detections. We selected a unique correlation threshold was selected for each component and station based on the unique observed noise characteristics.

In the case of multiple positive matches triggered on a channel within 3 seconds of each other, the mean time of detection is used as a preliminary event time. We then compare channels to determine when at least two channels on a station had detections triggered within 6 seconds of each other, and count these as detections. Detection capability was significantly better on the station DVB2 than any other in the local network, likely due to a high signal-to-noise ratio related to a combination of instrument type, low ambient noise at install location, and proximity to aftershocks.

A complete record of the 14 stations for the primary template event on 17 December 14:58 is shown in Figure 2.3. Analysts manually picked visible P- and S-arrivals for each of the 88 aftershocks at all temporary local stations. A subset of 38 events were identified as locatable, defined as having at least three stations with waveforms that allowed a seismic analyst to pick body wave arrival times, with a minimum of three P-arrival times and one S-arrival time. The stations most distant from the aftershock locations only detected the largest few aftershocks, with some stations recording too low signal-to-noise to pick a P-arrival and only the S-wave visible (e.g., DVB1, Figure 2.3).

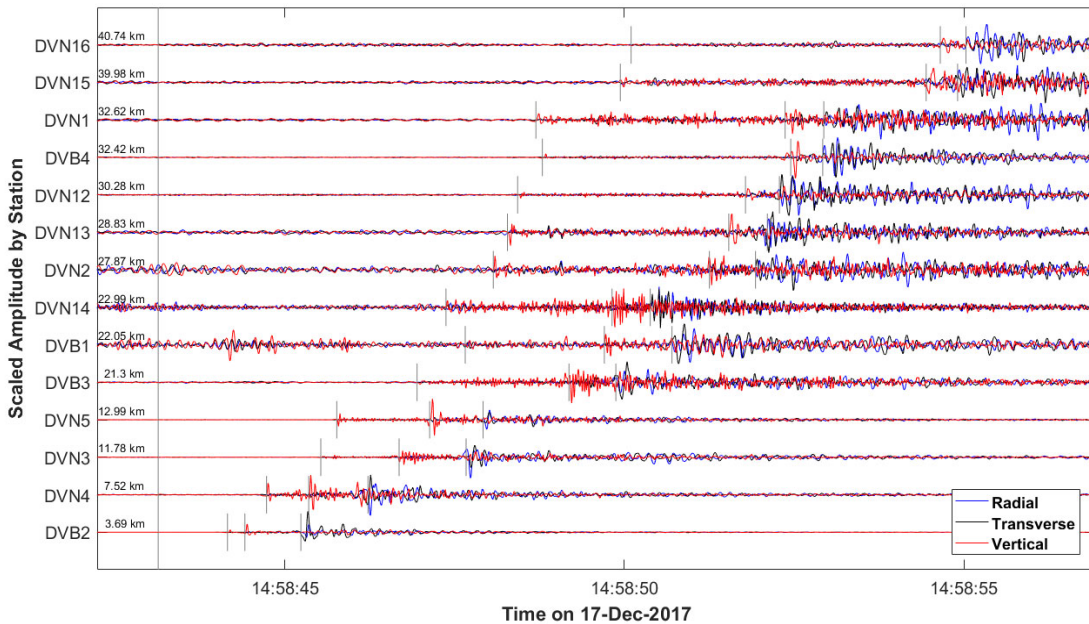


Figure 2.3: Local station waveforms by distance from event. Event-to-station distance is given for each station at the start of the trace. The pattern of P, sP, and S arrivals (short gray lines) is exhibited on each station, with the best visibility on the nearer stations. The time between sP and S is nearly constant for all distances and the time between P and sP lengthens with distance, supporting the interpretation of an S-wave converting to a P-wave at the sediment layer. The continuous gray line indicates the event origin time. Some marked arrivals are estimated and not used for location determination (Appendix 1). Amplitudes for each station are normalized to the maximum recorded for the respective station.

2. Earthquake Locations

Previous geophysical work on the Atlantic Coastal Plain (ACP) is limited and has not generated a satisfactory near-surface crustal velocity model for central Delaware that would allow for the most accurate location estimates for the 38 locatable events. Preliminary aftershock identification for the Delaware earthquake done by Kim et al. (2018) used the crustal earth model presented by Herrmann (1979), intended for the Central United States and including a 1-km surface layer with moderately low velocity. Other models identified for the CEUS and ACP include work done by Dreiling et al. (2017), which established P- and S-wave crustal velocities for the ACP but identified the need to separately account for surface site conditions.

Work by Pratt (2018) developed a model for Vs in the ACP strata from the fundamental frequencies of horizontal spectral ratios, but is derived from arrays located several hundred kilometers south of Delaware and has a depth to basement of 600 m. Studies in the Delmarva region using varied sources including seismic profiles and well data found depth to the crystalline, pre-Cretaceous basement is about 2350 m at Ocean City, MD, to the south on the Atlantic Coast (Miller et al., 2017; Olsson et al., 1988). At Island Beach, NJ, to the north and on the Atlantic Coast, depth to basement is about 1100 m (Olsson et al., 1988) and near Lewes, DE, about 50 km south of the aftershock locations, is about 2 km (Olsson et al., 1988). In addition, receiver function modeling by Cunningham and Lekic (2020) at the TA stations nearest to the epicenter of the main shock east of Dover, DE, found the thickness of the surface sediment layer is 2 km. We

therefore chose 2 km as an approximate depth to basement for our location and then determined the appropriate crustal velocities for the upper sediment layers.

We developed a velocity model for use in the location search using the base from the work of Dreiling et al. (2017). We reduced the top layer of Dreiling et al.'s model by 2 km corresponding to our surface sediment layer. The specific velocities and densities for the surface sediment layer were further refined using the modeling from Cunningham and Lekic (2020) by optimally dividing that 2 km of surface sediments into four layers of increasing seismic velocities.

The model was verified by matching waveforms from the M4.2 main shock observed at the regional station R61A in southern Delaware with synthetic waveforms generated using frequency-wavenumber integration with the 1D velocity model given in Table 2.2.

Thickness (km)	V_P (km/s)	V_S (km/s)	Density (g/cm³)
0.030	1.648	0.234	1.7
0.092	2.103	0.549	1.9
0.372	2.611	1.059	2.1
1.506	3.621	1.932	2.3
18	6.0	3.46	2.3
16	6.7	3.87	3.0
∞	8.1	4.68	3.4

Table 2.2: Velocity model used for determining aftershock locations and generating synthetics used for moment tensor inversion. The top two km are derived from Cunningham and Lekic receiver function modeling of crustal sediment at the nearest TA station and the basement layers are from Dreiling et al. (2017).

In order to determine event locations, an iterative grid search method was used. A preliminary search was centered on the estimated epicenter of the main shock and

extended 25 km in each direction, using grid spacing of 150 m and depth increments of 500 m between 1 and 10 km depth. For each grid location (latitude, longitude, depth), we used our velocity model to predict the P- and S- travel times from the grid point to each network station. We use a temporary origin time based on the mean difference between the observed P-pick times and predicted P-wave travel times for each station, as

$$t_{orig} = \frac{1}{n} \sum_{i=1}^{n_p} (p_{obs,i} - tt_{pred,i}^p) \quad 2.1$$

Optimal locations were determined based on the minimum residual between the observed travel times from P- and S-picks and the predicted travel times from each grid location to a station using our crustal velocity model. The residual was calculated for each grid point as follows:

$$R = \sum_{i=1}^{n_p} \left((p_{obs,i} - tt_{pred,i}^p) - t_{orig} \right)^2 + \sum_{k=1}^{n_s} \left((s_{obs,k} - tt_{pred,i}^s) - t_{orig} \right)^2 \quad 2.2$$

where n_p and n_s are the number of stations with P- and S-picks, respectively; p_{obs} and s_{obs} are the arrival times for P- and S-picks in seconds of day, and $tt_{pred,i}^p$ and $tt_{pred,i}^s$ are the predicted travel times for P- and S-waves in seconds. The horizontal location with the least residual is determined for each depth increment, and that interim optimal location is stored in an array with the corresponding observed and predicted travel times. The temporary origin time for that grid location at that depth is retained as the origin for that depth increment. Finally, the residuals for all depth increments are

compared and the depth with the least residual is determined to be the optimal event depth. The corresponding location and origin time for that depth are then identified as the final event location.

After preliminary locations were identified, mostly clustered with hypocenters just offshore beneath the Delaware Bay a few kilometers to the southeast of the main shock epicenter, the grid center was shifted southeast by about 3 km. In order to improve location accuracy, we reduced grid spacing to 100 m laterally and 100 m in depth, and reduced the overall search region to 15 km in each direction.

3. Source Parameters

For all events large enough to locate, we determined a local magnitude by converting the measured maximum horizontal component body wave amplitudes A to the equivalent Wood-Anderson amplitude (in mm) and using the relation for M_L calibrated for Eastern North America (ENA) intraplate events (W. Kim, 1998):

$$M_L = \log_{10} A + 1.55 \log_{10} X - 0.22 + C \quad 2.3$$

where C is a station correction term and X is the epicentral station-to-event distance in kilometers.

To test the hypothesis of high stress drop causing the low productivity observed for the Delaware aftershock sequences, we determined the Brune stress parameter (stress drop estimate) for the $M_w 4.2$ mainshock. We use the Brune model (Brune, 1970) as expanded by Kaneko & Shearer (2014) for a circular rupture (Chapter 1.2.1). We fit

the model to the P-wave and S-wave spectra for the main shock and our primary template aftershock at regional stations. We compute the corner frequency for the main shock model fit by modeling the best-fit power spectral ratio between the main shock and largest aftershock as follows:

$$\left(\frac{a \left(1 + \left(\frac{f}{f_{c2}} \right)^2 \right)}{\left(1 + \left(\frac{f}{f_{c1}} \right)^2 \right)} \right)^2 \quad 2.4$$

3. Results

1. Aftershock Detection

Using a single template, we identified 76 potential aftershocks, which were few enough to allow manual inspection of the waveforms for each. Because the local stations operated in near-field to the aftershock epicenters, small changes in aftershock epicenters result in a comparatively large difference in azimuth, affecting the detected waveform shape.

In addition to the typical variation in waveform shape, we observed a strong secondary arrival on the vertical component prior to horizontal arrivals, which we interpreted to be an S-to-P (sP) wave arriving due to conversion at the ray path transition for the sediment layer occurring in the Atlantic Coastal Plain (Figure 2.3). This wave conversion at the sediment layer has previously been reported in the Mississippi

Embayment by Chen et al. (1996). Daniels et al. (2020) observed a similar wave conversion in South Carolina due to the upgoing S-wave converting to a horizontally propagating P-wave; however, we do not find the same physics in our case, as our sP arrival is strongest on the vertical channel rather than the radial throughout the array (Figure 2.4). Furthermore, the time between arrival of the sP and S phases is more consistent than that of P and sP, suggesting the upgoing ray travels as an S-wave until it converts and traverses the shallow sediment layer as a P-wave (Figure 2.5).

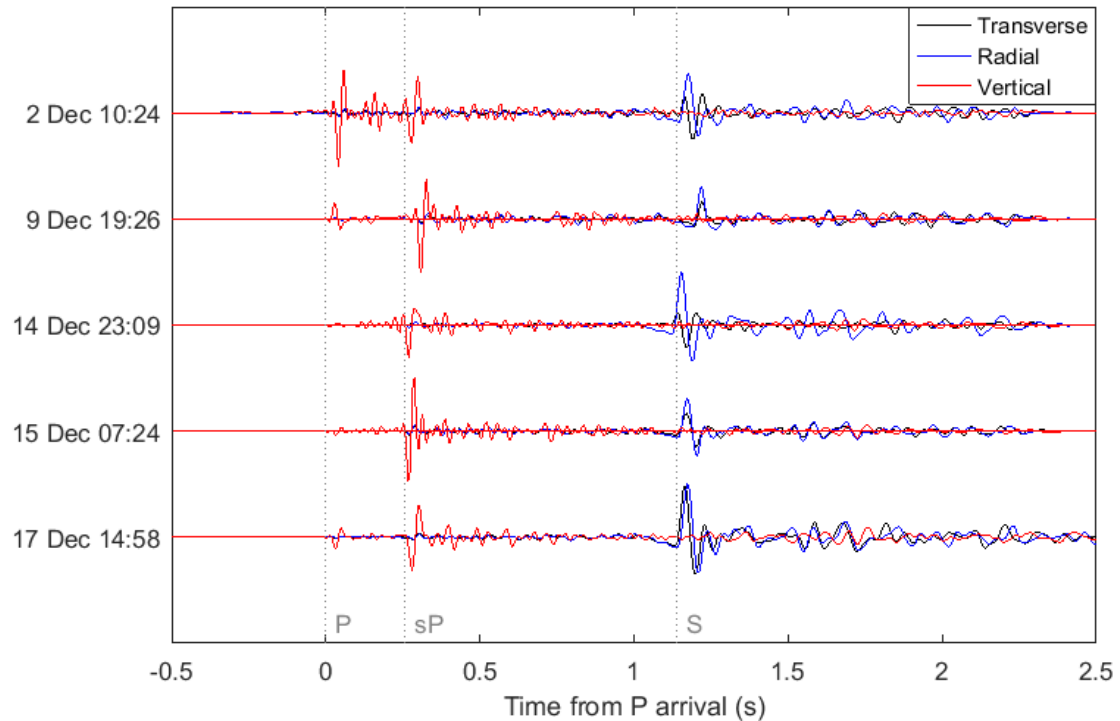


Figure 2.4: Waveforms for the five template events at station DVB2, the station nearest to the mainshock, showing transverse in black, radial in blue, and vertical in red. All amplitudes are scaled to the maximum for each event, which may be either vertical or horizontal. Each event is aligned to have the P-arrival at time 0; the sP converted wave arrival is clear on the vertical channel for each of the five templates at approximately time 0.25 seconds. Each phase arrival is marked in gray; arrivals are slightly different for each template due to different source locations. Amplitudes for each aftershock are normalized to the maximum recorded for the respective event.

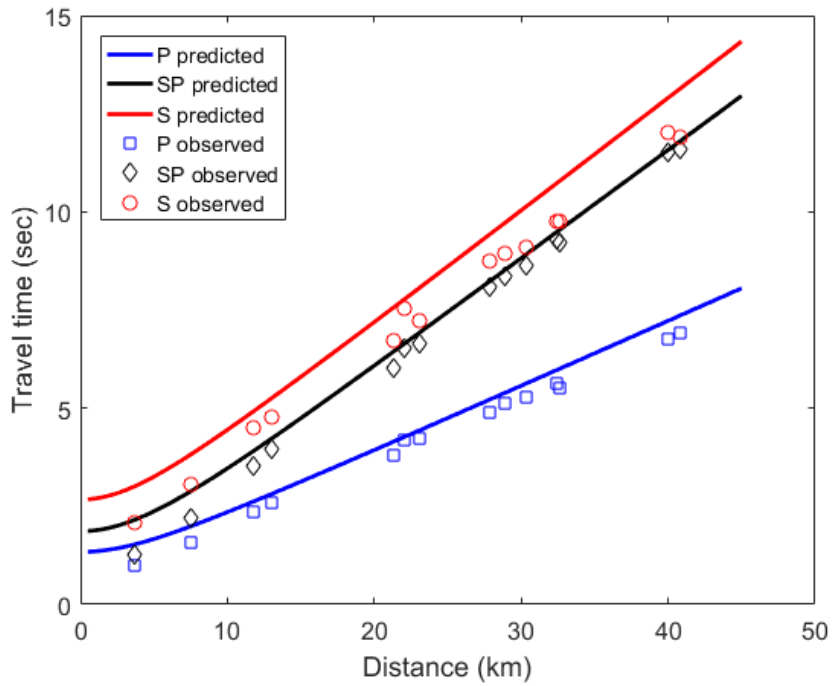


Figure 2.5: Predicted travel times curves (solid lines) for an earthquake at the location and depth of the 17 December 2017 14:58 M_L 1.4 aftershock, shown with measured phase arrival times for that event (open markers). The thinning of the sediment layer of the ACP getting further from the coast shows up in the closer spacing between the black (diamond) and red (circle) observations for the SP and S phase arrivals, as the sediment layer is thinner further west (see Figure 2.2 and Figure 2.3 for station location reference).

Because of these variabilities, we selected four additional templates to encompass different traits of the observed waveforms and improve detection through template matching with these variable waveforms (Figure 2.4). Because of diminishing gains with subsequent templates, no further templates were used.

Using four additional templates for detection, we increase the total detection count to 91 potential aftershock events. We subsequently eliminated three false detections after visual inspection of waveforms at each station, leaving a total of 88 events detected.

Over half of the 88 aftershocks were detected only at station DVB2, where the signal-

to-noise ratio was highest. This station was located closest to the main shock epicenter (Figure 2.2).

2. Aftershock Locations

Aftershocks are located primarily just offshore and below the Delaware Bay, with depths ranging from 0.5 to 6.5 km (Table 2.3; Figure 2.6). There did not appear to be any temporal progression in aftershock locations. There is a distinction between the larger magnitude and deeper events falling along the central portion of the fault, and smaller magnitude events occurring at shallower depths to either end (Figure 2.6). The SW end has aftershocks with depths from 0.5-2 km. The NE end aftershocks are almost exclusively 2.1 km in depth. The few aftershocks to the south of the main group (Figure 2.6) include three very shallow aftershocks similar to the other southern events as well as two deeper aftershocks.

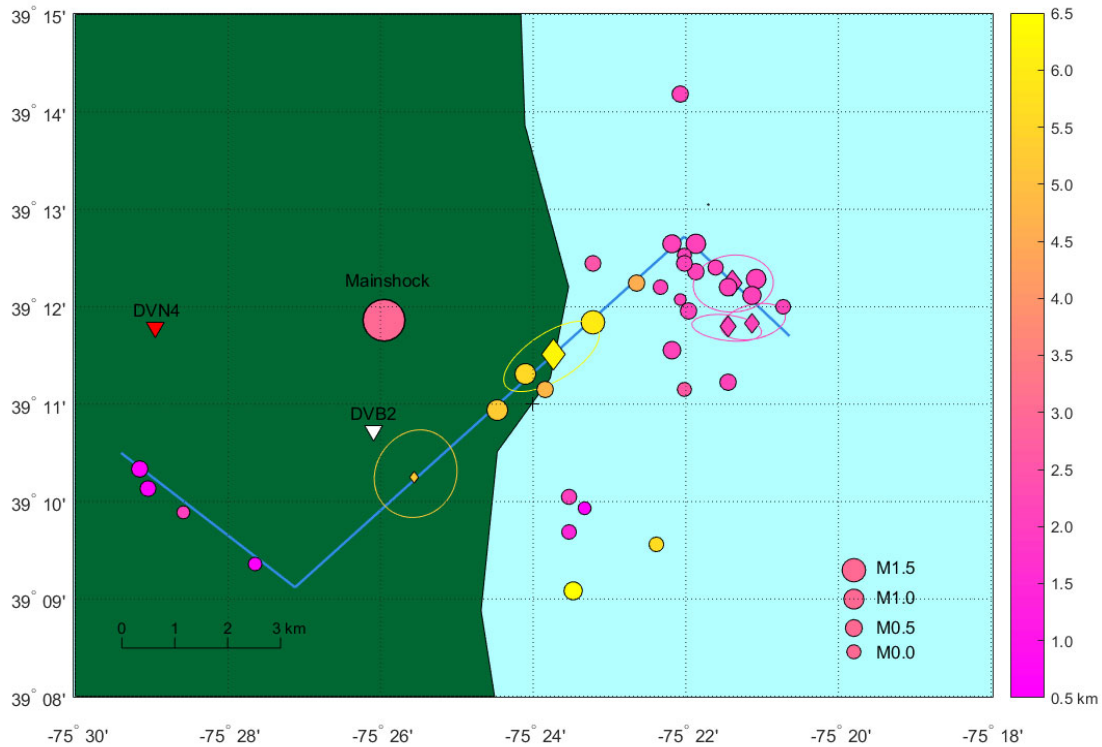


Figure 2.6: Locations of aftershocks. Shading corresponds to depth of the event, with magenta corresponding to the shallowest events (0.5 km) and yellow corresponding to the deepest event (6.5 km). Size of the marker is proportional to event local magnitude; see key for scale. Diamond-shaped markers indicate the events used as templates for aftershock detection and are shown with their one-sigma horizontal error contour. The approximate proposed fault is drawn in blue. The mainshock had an approximate depth of 3 km (Kim et al. 2018). Only the two nearest stations of the local deployment are visible in this projection; see Figure 2.2 for context of location in Delaware.

Figure 2.6 shows the one-sigma error for the aftershocks used as templates as a representative example of typical errors for location accuracy. However, we also observed that for small earthquakes, the location error was at times smaller than the pictured marker. There was an inconsistency in predicted location errors, with smaller errors present for the aftershocks with fewer picks used to resolve the location. Although the χ -square function used to determine the one-sigma error accounts for the number of data going into it (in this case, the number of valid P- or S-picks), we find there is additional unmodeled error that grows with additional data used from the more

Date	Time	Latitude	Longitude	Depth (km)	M_L
12/01/17	21:41:33.6	39.2175	-75.3618	2.1	-2.83
12/01/17	23:27:32.1	39.2013	-75.3679	2.1	-0.46
12/02/17	00:57:40.1	39.1648	-75.4764	2.0	-0.35
12/02/17	10:24:44.6	39.1973	-75.3522	2.1	0.09
12/02/17	14:36:14.6	39.1993	-75.3661	2.1	0.34
12/02/17	18:38:43.0	39.2047	-75.3514	2.1	0.82
12/04/17	02:31:26.2	39.2364	-75.3679	2.1	0.31
12/04/17	12:13:39.5	39.1925	-75.3696	2.1	0.60
12/05/17	01:23:59.3	39.2060	-75.3644	2.1	0.33
12/06/17	03:30:09.0	39.1655	-75.3887	0.5	-0.32
12/07/17	00:09:27.2	39.1594	-75.3731	5.7	0.01
12/07/17	00:44:01.6	39.2033	-75.3722	2.1	0.09
12/07/17	01:49:05.9	39.1513	-75.3913	6.5	0.61
12/07/17	18:53:52.7	39.1871	-75.3575	2.1	0.25
12/07/17	19:39:39.2	39.2108	-75.3644	2.1	0.77
12/08/17	12:17:48.4	39.2020	-75.3522	2.1	0.70
12/08/17	14:19:49.3	39.1722	-75.4859	0.5	0.31
12/09/17	19:26:58.6	39.2040	-75.3566	2.1	0.80
12/09/17	20:26:18.2	39.1615	-75.3922	1.4	-0.04
12/11/17	22:02:40.0	39.1824	-75.4078	5.3	1.09
12/12/17	04:24:57.9	39.1560	-75.4607	0.5	-0.20
12/13/17	00:45:24.4	39.1973	-75.3870	6.0	1.41
12/14/17	17:50:51.3	39.1675	-75.3922	2.0	0.11
12/14/17	23:09:50.9	39.1709	-75.4260	5.2	-1.00
12/15/17	07:24:09.8	39.1966	-75.3575	2.1	0.13
12/17/17	14:58:43.1	39.1919	-75.3957	6.3	1.39
12/17/17	16:07:04.8	39.1885	-75.4017	5.6	1.00
12/19/17	10:34:59.3	39.2067	-75.3601	2.1	0.04
12/23/17	00:57:46.0	39.2000	-75.3453	2.1	-0.08
12/23/17	13:29:50.9	39.1858	-75.3974	4.8	0.29
12/23/17	16:21:51.6	39.2074	-75.3870	2.5	0.34
12/27/17	14:11:44.7	39.2108	-75.3696	2.1	0.55
12/27/17	14:32:23.0	39.1689	-75.4842	0.5	0.16
12/28/17	05:39:22.7	39.1858	-75.3670	2.6	-0.17
12/28/17	09:42:24.9	39.2087	-75.3670	2.1	-0.15
12/31/17	00:11:18.9	39.2033	-75.3575	2.1	0.62
01/01/18	22:37:39.2	39.2040	-75.3774	4.6	0.31
01/02/18	05:36:19.3	39.2074	-75.3670	2.1	0.24

Table 2.3: Dates, times (UTC), epicentral locations, depths, and local magnitudes of 38 located aftershock events.

distant stations. These larger aftershocks using more arrival times from more distant stations are more sensitive to errors in the 1D crustal velocity model, as well as having greater sensitivity to human error in arrival time picking with lower signal-to-noise ratios.

3. Aftershock Magnitudes

Local magnitudes for these aftershocks are included in Table 2.3. Using these magnitudes, we obtained the Gutenberg-Richter relation between magnitude and number of events detected while the local network was deployed (Figure 2.7). The

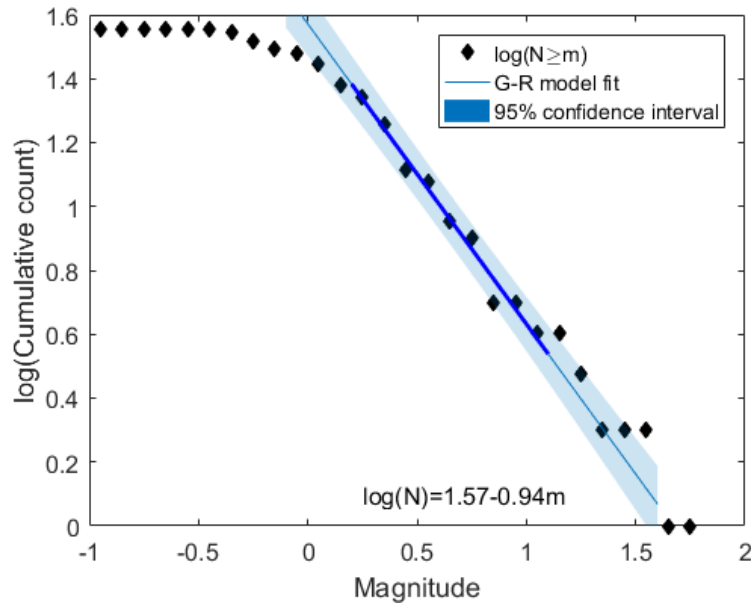


Figure 2.7: Gutenberg-Richter relation showing relative frequency versus magnitude of located aftershocks during the deployment period of the local network. Local magnitudes are calculated using Kim (1998) formula for ENA. The best-fit least-squares model is $\log(N)=1.57-0.94m$, with the shaded region indicating the 95% confidence of the fit.

detection magnitude of completeness is approximately $M_C=0.2$ and the b -value of the best-fit least squares model of the population is 0.94, near to the nominal value 1.0. Using the Aki (1965) method of estimating the b -value for the 38 located earthquakes, we obtain a value of 0.877 ± 0.365 , and the least-squares model of $b=0.94$ and Aki model estimates overlap.

We extrapolated magnitudes for the remaining 50 detected aftershocks first by determining the relationship between S-P arrival time vs event-to-station distance for located events. We used this relationship and the P- and S-phase picks for station DVB2, the only station to reliably detect all 88 aftershocks to estimate an event-to-station distance for that single station. The maximum amplitude required for equation 2.3 was determined, and then that equation was applied to get an estimate of the local magnitude. Because this method uses only one station and a location with higher error than those found via grid search, these additional events are considered to have greater error in magnitude accuracy. However, we were able to use the larger catalog of 88 aftershocks to again apply Aki's (1965) method for b -value estimation and to plot the Gutenberg-Richter relation in order to compare it to the smaller sample size above (Figure 2.8). In this case, the Aki (1965) estimate was $b=1.04\pm 0.40$, which overlaps substantially with the estimate for 38 events and is consistent with the least-squares estimate of $b=1.03$.

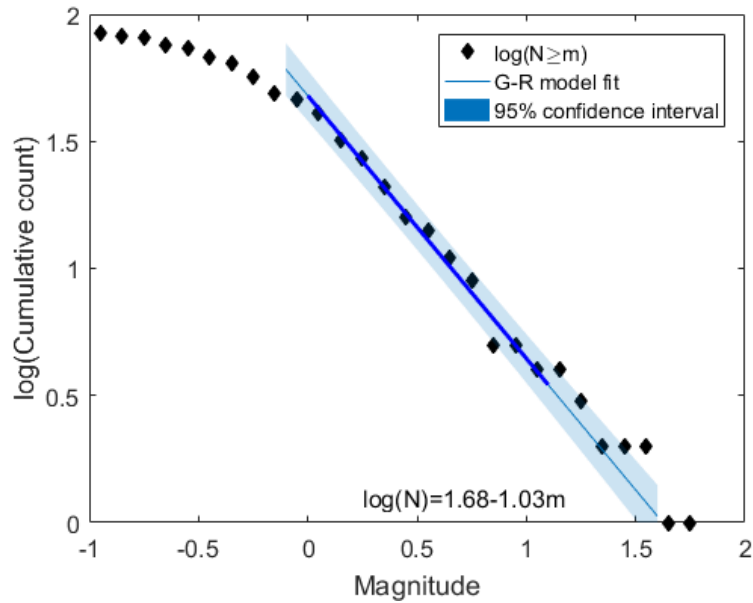


Figure 2.8: Gutenberg-Richter relation showing relative frequency versus magnitude of all detected aftershocks during the deployment period of the local network. Local magnitudes are calculated using Kim (1998) formula for ENA. The best-fit least-squares model is $\log(N)=1.68-1.03m$, with the shaded region indicating the 95% confidence of the fit.

4. Stress Parameter Estimation

We fit the power spectral ratio model to the P-wave and S-wave spectra for the main shock and our primary template aftershock at several nearby regional stations (see Figure 2.1 for locations). A table of the best-fit corner frequencies by station and body wave type is provided in Table 2.4. An example of the mainshock and aftershock spectra and spectral ratio modeling for the station GEDE is shown in Figure 2.9.

Network	Station	Dist. (km)	f_c (Hz)	k	Radius (m)	$\Delta\sigma$ (MPa)
LD	GEDE	70	3.4	0.38	346.0	27.46
PE	PSUB	81	6.2	0.38	212.1	119.27
LD	WUPA	83	3.0	0.38	438.3	13.51
LD	TUPA	110	4.8	0.38	273.9	55.35
LD	MVL	119	5.0	0.38	263.0	62.56
LD	FMMC	126	3.8	0.38	346.0	27.46
LD	LUPA	156	2.2	0.38	597.6	5.33
LD	GEDE	70	3.1	0.26	290.2	46.55
PE	PSUB	81	3.0	0.26	299.9	42.19
LD	WUPA	83	1.7	0.26	529.2	7.68
LD	TUPA	110	1.3	0.26	692.0	3.43
LD	MVL	119	3.8	0.26	236.7	85.73

Table 2.4: Main shock corner frequencies for regional stations listed by distance to mainshock, with corresponding circular fault radius and stress drop estimate using k parameters for P-wave and S-wave (above and below heave line, respectively) from Kaneko and Shearer (2014) and the moment derived by Kim et al (2018) ($2.6e15$ Nm). The shear wave velocity used was 3.46 km/s (Table 2.2). LD: Lamont-Doherty Cooperative Seismographic Network, PE: Pennsylvania State Seismic Network.

We determine median stress drop estimate is 34.82 MPa, and the median fault radius is 323 m. The estimated stress drop (Brune stress parameter) was typical for an intraplate earthquake. In comparison, the 2011 Mineral, VA, earthquake stress drop was variably reported as unusually high (50-75 MPa) (Ellsworth et al., 2011; Wu & Chapman, 2017), even by ENA standards, and as a more typical intraplate value of 5-25 MPa (Hartzell et al., 2013). Wu and Chapman (2017) found the larger aftershocks ($M \geq 2.5$) had the largest stress drops of those examined, which would also be consistent with a larger stress drop for the M4.2 mainshock in Delaware.

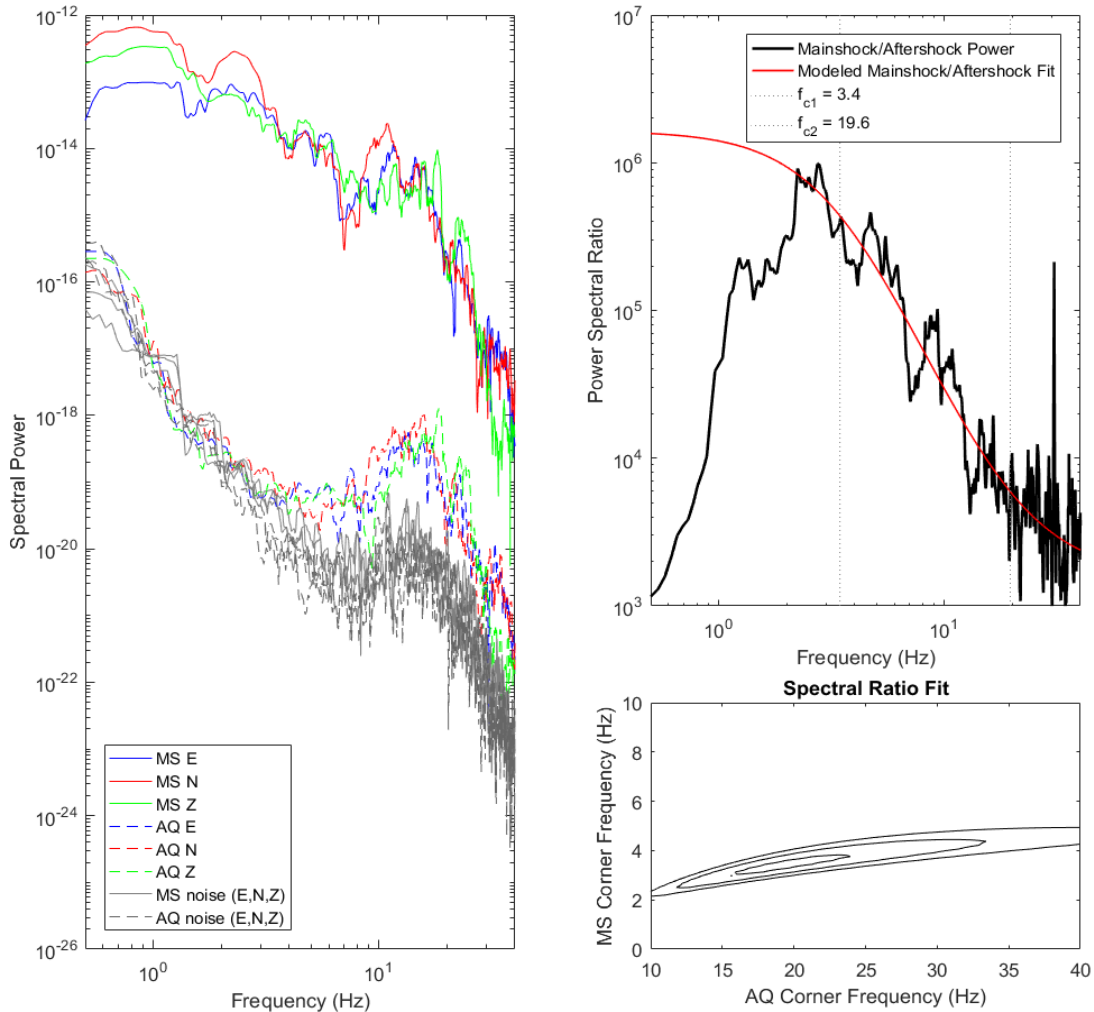


Figure 2.9: (a) Brune model fit to mainshock (“MS”) P-wave spectral power (solid lines) and $M_L 1.6$ aftershock (“AQ”) on 17 December 14:58 (dashed lines) at station GEDE. For both events, blue is east, red is north, and green is vertical channel data. Noise windows prior to each event are in gray. (b) Mainshock spectral power to aftershock spectral power ratio is shown in solid black. The best-fit spectral ratio model using these two events is fit in red. Thin gray lines indicate the two corner frequencies. (c) The spectral ratio tradeoff between mainshock and aftershock corner frequencies for the optimal coefficient a .

Considering the stress drop of 35 MPa is within the expected range for a stable continental region earthquake, we therefore do not attribute stress drop as the cause for the low aftershock productivity in Delaware and do not examine this further.

4. Discussion

1. Productivity

The 30 November 2017 M4.2 Delaware mainshock was followed by a maximum M1.4 aftershock on 17 December 2017 (Table 2.3), giving $\Delta m=2.8$, more than twice the typical difference given by Båth's Law.

We use an extrapolation of the Gutenberg-Richter relation shown above for the detected aftershocks to infer the largest nominal aftershock (Shcherbakov & Turcotte, 2004). We use the Gutenberg-Richter relation, $\log_{10} N(\geq m) = a - bm$, and take $N(\geq m^*) = 1$ for the largest nominal aftershock m^* (Shcherbakov & Turcotte, 2004). Thus, given our coefficients $a=1.57$ and $b=0.94$ for the frequency-magnitude relation shown in Figure 2.7, we have $m^*=1.67$.

The resulting nominal largest aftershock $m^*=1.67$ based on the frequency-magnitude distribution relation of all aftershocks is consistent with the observed largest magnitude M_L1.4, and still results in an unusually large $\Delta m^*=2.53$. The overall low productivity indicated by the Gutenberg-Richter a -value is consistent with the larger-than-typical Δm observed for the sequence.

Båth's Law indicates that the largest aftershock typically has about 50 times less energy than the mainshock, given a 1.2 magnitude unit difference. In the case of the 2017 Delaware earthquake, the largest aftershock was a further 1.33 magnitude units lower

than expected, indicating it has 125 times less energy than expected and 10,000-15,000 times less energy produced than the mainshock.

We used a Bayesian Markov Chain Monte Carlo simulation to optimally determine the log-likelihood of parameters a , b , c , and p in the Omori decay rate equation given by

$$\lambda(t, M_{min}) = 10^{a+b(M_{main}-M_{min})}(t + c)^{-p} \quad 2.5$$

(Appendix 2:). We use the ensemble model of solutions to find the mean and 2σ (95% confidence interval) for each parameter (Figure 2.10), and tradeoffs between these parameters (Figure 2.11). These estimates are compared to values Page et al. (2016) presented for Stable Continental Region (SCR) parameters in a small number of aftershock sequences that followed a $M \geq 6.4$ mainshock, and values given by Ebel (2009) in his estimates for SCR aftershock parameters for 13 aftershock sequences following an $M \geq 5$ mainshock (Table 2.5).

	Bayesian MCMC solution	Page et al. (2016) SCR	Ebel (2009) SCR
a	-3.026 ± 1.102	-2.28	-1.815 ± 0.821
b	0.897 ± 0.276		0.865 ± 0.226
p	0.942 ± 0.425	0.73	1.046 ± 0.221

Table 2.5: Mean and 95% confidence interval ($\pm 2\sigma$) for the ensemble of model solutions for parameters $\{a, b, p\}$, compared with results from Page et al. (2016) and Ebel (2009).

The b -value is consistent with that found by Ebel (2009) and While the b and p values are within the confidence intervals, the a -value is still remarkably low. We note however that our a -value is more consistent with the Page et al. (2016) value for stable oceanic regions of -2.98. The proximity of the continental shelf may play a role in this

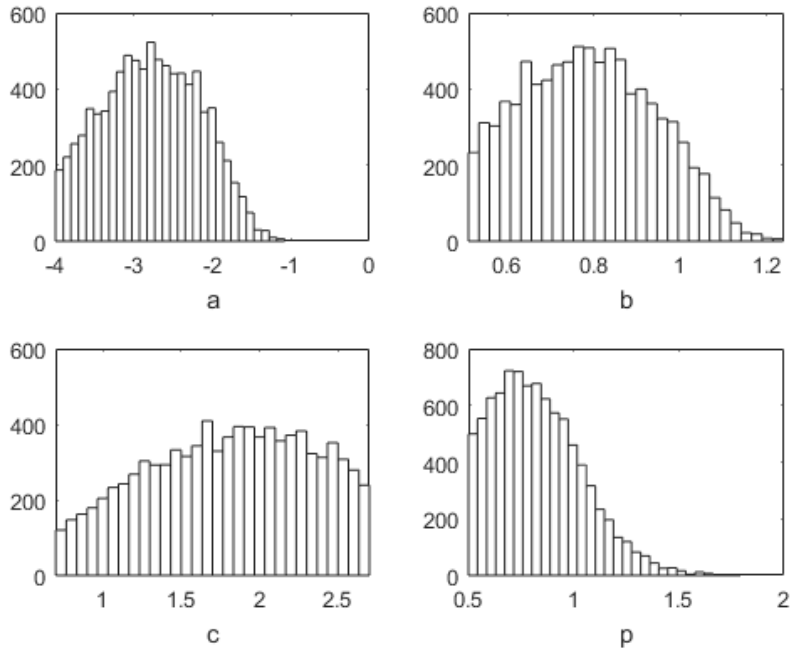


Figure 2.10: a-d) Histograms showing the distribution of values for each parameter in the ensemble of model solutions for the rate equation.

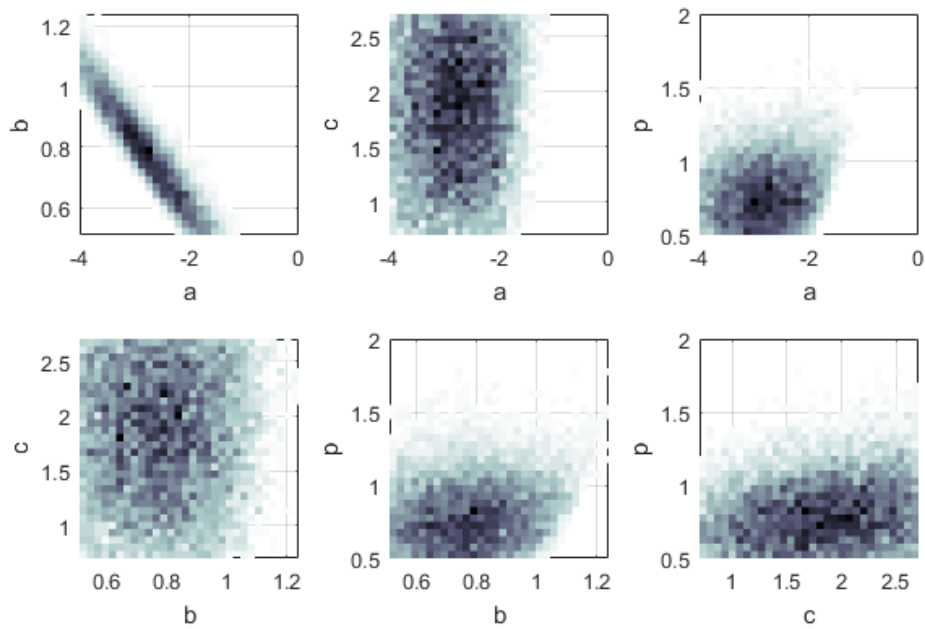


Figure 2.11: Tradeoffs between each pair of parameters. Although b does not have as defined a distribution as a , the two share a strong correlation. Parameters a and p are individually better defined (Figure 2.10) but only have a slight correlation.

factor and is an area for further research. To compare, the 2011 Mineral, Virginia, aftershock sequence had a lower b -value (0.86), a value for the Omori p near 1, and a typical Δm , all consistent with Ebel's (2009) findings for stable continental earthquakes with $M \geq 5$ (Wu et al., 2015; Wu & Chapman, 2017). However, this value for p is inconsistent with that found by Page et al. (2016).

2. Potential Causes

Hatcher provides a detailed map of the surface geology units in the Salisbury Embayment region, with greater detail in the ACP Chesapeake Group sediments than are often provided (2007). The location of the M4.2 main shock is approximately at the interface of the Carolina superterrane and the Brunswick (Charleston) terrane in east-central Delaware (Hatcher Jr. et al., 2007). It is also the inferred northern end of the Taylorsville Rift basin, a Mesozoic rift zone (Hatcher Jr. et al., 2007; Olsen, 1990; Withjack et al., 2012). The half-grabens remaining from rifts in this region have a NE-SW trend following the rifting process that broke up Pangaea in the Triassic-Jurassic (Olsen, 1990; Withjack et al., 1998). Studies suggest that these faults may not be as inactive as previously assumed (Gardner, 1989).

Delaware has an overall NE-SW striking stress field, consistent with the majority of the CEUS (Gardner, 1989; Heidbach et al., 2018; Zoback & Zoback, 1989). The moment tensor for the main shock had three consistent solutions from the National Earthquake Information Center (NEIC), Saint Louis University (SLU), and by Kim et al. (W. Kim et al., 2018). The strikes of the two nodal planes were approximately 0°

and 100° for each of these moment tensors, which are moderately well-aligned for the prevailing stress field at $\sim 45^\circ$.

Kim et al. (2018) proposed a north-striking fault, which would be well-aligned with the background stress to produce aftershocks. Additionally, Kim et al. (2018) find the compressional P-axis from their moment tensor consistent with a NE-striking stress field. However, the locations determined in this paper using local data are not consistent with a northward-striking fault (Figure 2.6). Furthermore, the low aftershock productivity is inconsistent with a fault that is well-aligned with background stress to promote shear failure.

The aftershock locations we find in this paper fall along an apparent central NE-SW fault with stepover faults at either end (Figure 2.6). In this case, the predominant stress field would promote normal stresses and have limited shear stress, which may explain some of the limited aftershock productivity. This fault alignment is supported by the known geology and the general shape and orientation of the half-grabens remaining from Mesozoic rifting. However, the mainshock moment tensor is not consistent with this fault geometry. It is also possible the mainshock did not occur on the central NE-striking portion of the identified fault; location uncertainty for the mainshock is ± 2.5 km (“Event Page M4.1 - 9km ENE of Dover, Delaware,” n.d.; W. Kim et al., 2018).

Low aftershock productivity has also been reported for moderate magnitude earthquakes in South Carolina (Daniels et al., 2019) and Maine (Quiros et al., 2015).

This suggests that aftershock behavior in the intraplate CEUS is not well-modeled by parameters that are derived from modeling California earthquakes and may not be well-modeled by parameters from generic worldwide stable continental regions.

5. Conclusions

The use of a local network increased the total number of detected aftershocks during the period from late on 1 December 2018 – 11 January 2018 by an order of magnitude and lowered the magnitude of completeness for detected events by approximately one magnitude unit, relative to detections with regional stations reported by Kim et al. (2018).

We observed a lower-than-typical aftershock productivity for this sequence, characterized by a significant magnitude difference between the mainshock and largest aftershock, with the subsequent aftershock magnitude distribution following a typical Gutenberg-Richter distribution.

The 2017 Delaware earthquake was followed by an aftershock sequence with a near-nominal b -value for the Gutenberg-Richter distribution. The slope $b=0.98$ indicates the relative proportions of smaller and larger aftershocks were typical, but the a -value of the distribution, related to overall productivity, was lower than we would anticipate.

The difference between the mainshock and largest aftershock magnitudes was $\Delta m=2.8$, in contrast to Båth's Law expected difference $\Delta m=1.2$. A nominal distribution following the Gutenberg-Richter frequency-magnitude relation with a maximum

magnitude of M3 following an M4.2 mainshock would produce approximately 1000 M0 aftershocks.

We detected a total of 88 aftershocks to a completeness of M0, with a maximum magnitude $M_L1.6$. The Delaware earthquake aftershock productivity was therefore approximately an order of magnitude lower than expected given the size of the mainshock.

Our research on this well-recorded aftershock sequence has revealed characteristics that differ from those seen in California and worldwide studies used as a baseline for aftershock modeling. The intraplate location in the Eastern US means that driving forces for earthquakes are likely not a primary result of tectonic motion. By better understanding the causes for this aftershock sequence, scientists will be better prepared to extrapolate the behavior of future aftershock sequences in similar non-plate boundary locations.

We do not find an unusual stress drop and therefore do not consider stress drop to be a contributing factor to the low number of aftershocks. The apparent primary fault follows historic rifting boundaries and is poorly-aligned for shear failure, which may contribute toward lower-than-usual aftershock productivity.

Chapter 3: November 2016 M5.8, Pawnee, Oklahoma

1. Background

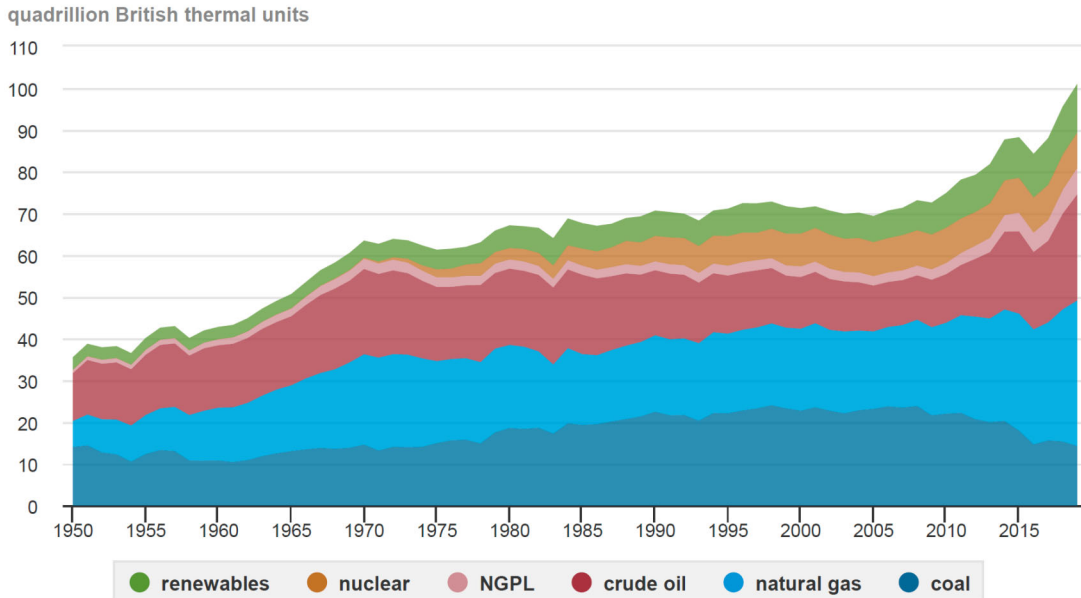
1. Enhanced Oil Recovery and hydrofracturing

Some of the most significant political and economic issues facing the United States include energy independence and the increasing use of clean energy. The Energy Independence and Security Act (EISA) of 2007 was a key driver in national policies toward energy security and renewable resources, providing for research and development funding to improve technologies such as Enhanced Geothermal Systems using Hot Dry Rock (110th Congress, 2007). The American Recovery and Reinvestment Act of 2009 further invested in geothermal technology (111th Congress, 2009).

One consequence has been an increase in the use of natural gas as a fuel source for utilities nationwide in the past decade. Figure 3.1 shows the total BTUs of energy produced from all primary fuel sources in the United States in the past 69 years and the breakdown of production for the six main source types. Over the past decade, coal decreased its share of total energy production while natural gas increased its share of total production. Natural gas is considered a cleaner alternative to coal and often considered a viable “gap” fuel to use while technology develops further and economies of scale bring renewables into a larger market share (Burnham et al., 2012; Levi, 2013).

Crude oil, which had been gradually decreasing in share from around 1980 to the mid-2000s also began to again increase in total energy production.

U.S. primary energy production by major sources, 1950-2019



Note: NGPL is natural gas plant liquids.

Source: U.S. Energy Information Administration, *Monthly Energy Review*, Table 1.2, April 2020, preliminary data for 2019

Figure 3.1: Primary energy production in the US since 1950. NGPL: Natural gas plant liquids.

As easily accessed oil reserves run out, shale oil wells have gone into production or wells started secondary production, which generates higher volumes of wastewater than historical oil drilling ventures (Rubinstein & Mahani, 2015). The essential technology allowing the recent boom in fracking-type oil recovery was the ability to drill horizontally once underground to open a formation, as the general use of high pressure water to fracture rock for permeability has been in use for years (Ellsworth, 2013; Rubinstein & Mahani, 2015).

The primary method of oil and natural gas recovery tied to increased seismic hazard is the use of hydraulic fracturing, or fracking. This method involves pumping large volumes of water into an oil- or gas-containing formation to fracture rock and increase the permeability, allowing the oil to be pumped out. The fracturing provides improved access where previously these resources would be locked in place and pumping was not cost-effective (Rubinstein & Mahani, 2015). For both fracked and depleted conventional sources, the oil or gas that is pumped out is mixed with briny water from the source rock, and must be processed to separate the desired product from the waste. Because wastewater is very impure, it cannot be simply disposed superficially to drain into groundwater and streams, where it may adversely affect the local flora and fauna or human water resources. Instead, the wastewater is pumped back underground, generally into a layer even deeper than the original source rock and below low-permeability sealing layers to protect groundwater reserves (Brown et al., 2012; Rubinstein & Mahani, 2015).

Besides potential adverse effects related to wastewater infiltrating groundwater reserves, the fracturing of rock through injection of water inherently creates microseismicity that at times can be large enough to be felt in the region surrounding an injection site (Rubinstein & Mahani, 2015). Additionally, wastewater disposed of in deep rock formations has been linked to increased seismicity in regions of hydrofracking for oil and gas recovery (Ellsworth, 2013, and additional studies addressed below).

Although some hydraulic fracturing has been linked directly to earthquake activity (Schultz et al., 2015; Skoumal et al., 2015), most increased intraplate seismicity observed to date in the U.S. has been associated with the wastewater injection following oil or gas production (Ellsworth, 2013; Rubinstein & Mahani, 2015). This has been seen in places as varied as Ohio (W. Kim, 2013), Kansas (Choy et al., 2016), Texas (Frohlich et al., 2016), Arkansas (Horton, 2012), and Oklahoma (Ellsworth, 2013; Keranen et al., 2013; Walsh & Zoback, 2015).

The history of injection-induced seismicity began in 1961 at the Rocky Mountain Arsenal near Denver, Colorado. A disposal well for the U.S. Army was drilled 3671 m deep, ending in Precambrian crystalline basement rock (Healy et al., 1968; Raleigh et al., 1976). In the subsequent years, the number of area earthquakes per month correlated strongly with the monthly well pressure. This correlation in time and space is highly statistically improbable naturally and is an effect of pore pressure lowering the effective normal stress, facilitating earthquakes. Additional peaks in earthquakes were observed by Healy et al. (1968) even after wellhead pressure dropped in early 1966, which was attributed to fluid diffusion and the resulting delay before effective normal stress again exceeded shear stress.

McGarr (2014) reports that the maximum seismic moment for induced earthquakes in Oklahoma appears to be limited based on the volume of injected fluid, using supporting examples from several states. However, this was questioned by van der Elst et al. (2016) when they proposed that total injected volume related to total number of events, which in turn related to magnitude of events via size scaling relations of the Gutenberg-

Richter Law. The individual seismic moment for a single earthquake, however, is limited merely by the statistical unlikelihood of large events (large seismic moment) when few total events have occurred (van der Elst et al., 2016). Further study has suggested that the pressurization rate rather than total volume injected or pressure magnitude may have a greater governing effect (French et al., 2016).

Despite the long history knowing the association between fluid injection and earthquakes, it has only very recently become a contributor to earthquake hazard in Oklahoma (Petersen et al., 2016). Given its intraplate tectonic setting, prior to about 2008 Oklahoma averaged just 2.3 earthquakes per year over a magnitude 3.0 (Figure 3.2) (Various, 2021). Between 2008 and 2015, advances in oil and natural gas recovery techniques using hydrofracturing and the disposal of high volumes of associated wastewater via high-rate injection into the subsurface were linked to an exponential increase in the rate of seismicity in Oklahoma (Keranen et al., 2013, 2014; Walsh & Zoback, 2015; Weingarten et al., 2015). The locations of induced earthquakes in Oklahoma have been correlated to wastewater injection wells and are concentrated in the northern and central parts of the state (Figure 3.3).

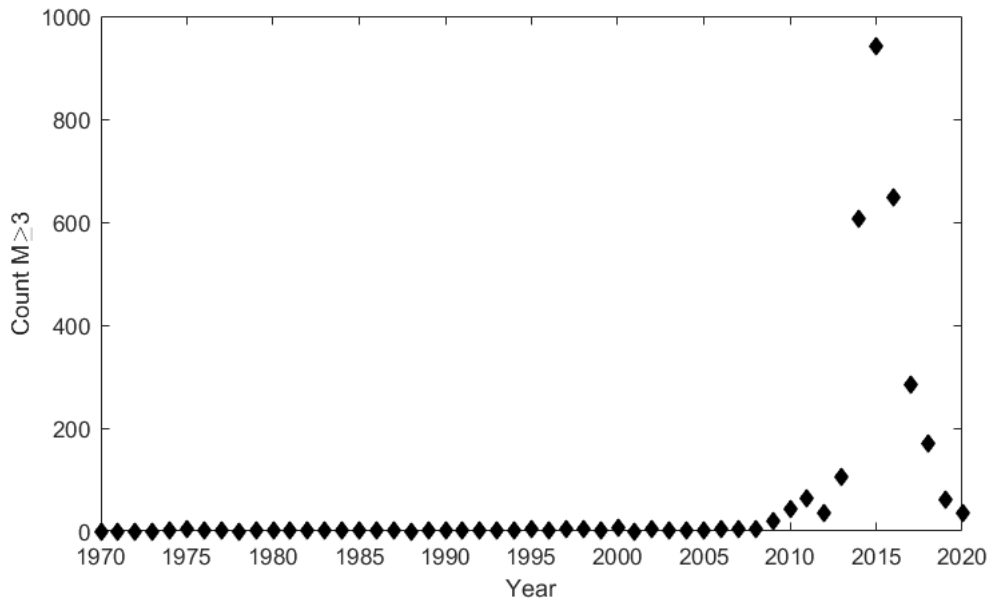


Figure 3.2: Count of earthquakes above the magnitude of completeness ($M_{3.0}$) in Oklahoma by year.

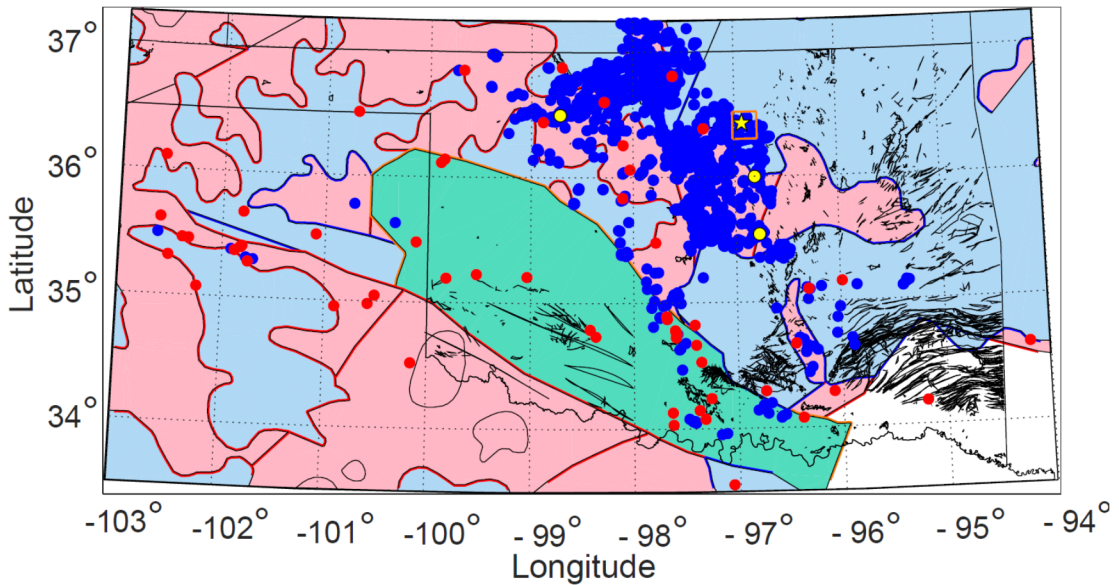


Figure 3.3: Oklahoma geologic provinces with known faults and seismicity $M_{3.0}$ and greater prior to 2007 (red) and after 2008 (blue). Magnitude $M_{\geq 5}$ earthquakes are shown in yellow with the $M_{5.8}$ Pawnee event depicted with a star. Clockwise from west: Fairview ($M_{5.1}$), Cushing ($M_{5.0}$), and Prague ($M_{5.7}$). Green depicts ancient rifts, blue are granitoids, and pink are juvenile crusts. Faults from USGS (mrdata.usgs.gov). Geologic model from Whitmeyer and Karlstrom (2007).

Despite new regulations put in place in late 2015 (Baker, 2015), 2016 continued to have high earthquake hazard. While the total count of $M \geq 3$ earthquakes began to decrease year-on-year, 2016 was still host to several large magnitude earthquakes: M5.0 Cushing, M5.1 Fairview, and M5.8 Pawnee. As a result, the total seismic moment release in 2016 was the largest yet recorded in Oklahoma (Yeck et al., 2017).

Healy et al. (1968) also showed how propagation of the fluid pressure front can result in relatively more large events following cessation of injection because fluids cease to reach smaller, nearby cracks but the pressure front continues to activate longer and more extensive faults with greater potential for large magnitude events. Propagation of the fluid pressure front was more recently reported by Keranen et al. (2014) in observations of Oklahoma seismicity relative to injection wells there.

Long-term effects of fluid diffusion, well injection rates and volumes, proximity to faults, and specific local geology interact in a complex manner governing these earthquakes (Keranen et al., 2014; Rubinstein & Mahani, 2015; Yeck et al., 2017). A change in the pressure of pore fluid can extend to greater distances than the actual distance of fluid diffusion for injected material, which could allow earthquakes to be triggered at much further distances than anticipated by the changes in pressure (Rubinstein & Mahani, 2015).

2. Previous moderate magnitude earthquakes in Oklahoma

The stress orientation that has been measured in Oklahoma is generally E-W to ENE-WSW (Alt & Zoback, 2017). Faulting in the central part of the state is nearly all strike-slip, with some normal faulting observed in the more northern regions (Figure 3.3) (Alt & Zoback, 2017). The earthquakes detected since the onset of induced seismicity fall mainly on linear structures subparallel to the stress orientation (Schoenball & Ellsworth, 2017).

Different patterns of foreshock and aftershock activity have been observed from induced earthquakes in Oklahoma. The Fairview earthquake sequence in February 2016 was very energetic, having several M4 aftershocks and an M5.1 mainshock (Schoenball & Ellsworth, 2017).

2. Introduction

1. Summary

Following the M5.8 earthquake near Pawnee, OK, on 3 September 2016, a group of seismologists from Cornell University installed a temporary local network including 16 broadband seismometers to supplement the regional network for detecting aftershocks. The deployment provided a high detection capability, with several stations within 20 km of the mainshock epicenter to provide an aftershock dataset with a low magnitude of completeness ($M_c = 0.1$). This provided an opportunity to study an

aftershock sequence in a region with induced seismicity where fluids are known to play a role in triggering earthquakes (Ellsworth, 2013; Keranen et al., 2013, 2014). Several additional permanent stations were added in the Pawnee area of Oklahoma in 2017, after the M5.8 occurred, but were not available for immediate aftershock detection in later 2016 (Schoenball & Ellsworth, 2017).

2. Data

A total of 16 broadband seismometers were operational for varying intervals during the period from 4 September 2016 – 6 October 2016. Each seismometer remained in service between 7 and 32 days of the 33-day operation. An average of 11 broadband stations were operating on any given day of the deployment. Table 3.1 shows the fraction of operational time for each station on each day of the temporary deployment. Three of the stations recorded data at 100 Hz (stations OK044, OK050, and OK051) and the remainder recorded at 250 Hz.

3. *Methods*

1. Waveform correlation

We used a matched filter algorithm to identify smaller earthquakes in a 10-km radius region following the M5.8 Pawnee earthquake. While most of these small earthquakes are expected to be aftershocks, the elevated background rate due to induced seismicity precludes assuming that all detections will be aftershocks.

Table 3.1: Fraction of day each local network station was operational for the duration of the temporary deployment. Total fraction of the array operational per day is calculated by summing the proportion of operational time for all 16 stations on a day and dividing by 16. Numbers in bold are stations that were operational for less than 90% of a day. In the last column, numbers in bold indicate days with less than 60% of the array time operational, approximately equal to fewer than 10 out of 16 stations operating.

Date	A012	A013	A014	OK044	OK050	OK051	PW01	PW02	PW03	PW04	PW05	PW06	PW10	PW11	PW12	PW13	Fraction of Array
4-Sep-16	0.09						0.36	0.29	0.18		0.22	0.07					0.07
5-Sep-16	1.00	0.25					1.00	1.00	1.00	0.30	1.00	1.00	0.08	0.07			0.42
6-Sep-16	1.00	1.00	0.97				1.00	0.99	0.98	1.00	0.04	1.00	1.00	1.00			0.62
7-Sep-16	1.00	1.00	1.00				1.00	1.00	1.00	1.00		1.00	1.00	1.00	1.00	1.00	0.75
8-Sep-16	1.00	1.00	1.00				1.00	1.00	1.00	1.00		0.94	0.99	1.00	1.00	1.00	0.75
9-Sep-16	1.00†	1.00	1.00				1.00	1.00	1.00	1.00		1.00	1.00	1.00	1.00	0.62	0.67
10-Sep-16	1.00	1.00	1.00		0.20		1.00	1.00	1.00	1.00		1.00	1.00	1.00	1.00	1.00	0.76
11-Sep-16	1.00	1.00	1.00		1.00	0.24	1.00	1.00	1.00	1.00		1.00	1.00	1.00	1.00	1.00	0.83
12-Sep-16	1.00	1.00	1.00		1.00	1.00	0.99	1.00	1.00	1.00		1.00	1.00	1.00	1.00	1.00	0.87
13-Sep-16					1.00	1.00	1.00	0.99	1.00	0.94		0.97	1.00	0.98	0.99	1.00	0.68
14-Sep-16					1.00	1.00	1.00	1.00	0.99	1.00		1.00	1.00		1.00		0.56
15-Sep-16				1.00	1.00	1.00	1.00	1.00	1.00	1.00	1.00	1.00	1.00		1.00		0.69
16-Sep-16				1.00	1.00	1.00	1.00	1.00	0.62	1.00	1.00	1.00	1.00		1.00	0.93	0.72
17-Sep-16				1.00	1.00	1.00	1.00	1.00		1.00	1.00	1.00	1.00	0.01	1.00	1.00	0.69
18-Sep-16				1.00	1.00	1.00	1.00	1.00		1.00	0.65	1.00	1.00	1.00	1.00	1.00	0.73
19-Sep-16				1.00	1.00	1.00	1.00	1.00		1.00		1.00	1.00	1.00	1.00	1.00	0.69
20-Sep-16				1.00	1.00	1.00	1.00	1.00		1.00		1.00	1.00	1.00	1.00	1.00	0.69
21-Sep-16				1.00	1.00	1.00	1.00	1.00		1.00		1.00	1.00	1.00	1.00	1.00	0.69
22-Sep-16				1.00	1.00	1.00	1.00	1.00		1.00		1.00	1.00	1.00	1.00	1.00	0.69
23-Sep-16				0.95	0.95	0.95	1.00	1.00		1.00		0.98	1.00	1.00	1.00	1.00	0.68
24-Sep-16				1.00	1.00	1.00	1.00	1.00		1.00		1.00	1.00	1.00	1.00	1.00	0.69

25-Sep-16				1.00	1.00	1.00	1.00	1.00		1.00		1.00	1.00	1.00	1.00	1.00	0.69
26-Sep-16				1.00	1.00	1.00	1.00							1.00		1.00	0.38
27-Sep-16				1.00	1.00	1.00	1.00	1.00		1.00		1.00	1.00	1.00	1.00	1.00	0.69
28-Sep-16				0.29	0.29	0.29	1.00	1.00		1.00		1.00	1.00	1.00	1.00	1.00	0.55
29-Sep-16				0.99	0.99	0.99	1.00	1.00		1.00		1.00	1.00	1.00	1.00	1.00	0.69
30-Sep-16				1.00	1.00	1.00	1.00	1.00	0.09	1.00		1.00	1.00	1.00	1.00	1.00	0.69
1-Oct-16				1.00	1.00	1.00	1.00	1.00	1.00	1.00		1.00	1.00	1.00	1.00	1.00	0.75
2-Oct-16				1.00	1.00	1.00	1.00	1.00	1.00	1.00		1.00	1.00	1.00	1.00	1.00	0.75
3-Oct-16				1.00	1.00	1.00	1.00	1.00	1.00	1.00		1.00	1.00	1.00	1.00	1.00	0.75
4-Oct-16				1.00	1.00	1.00	1.00	1.00	1.00	1.00		1.00	1.00	1.00	1.00	1.00	0.75
5-Oct-16				1.00	1.00	1.00	0.62	0.79	1.00	1.00		1.00	1.00	0.78	1.00	1.00	0.70
6-Oct-16									0.64	0.66		0.55	0.57		0.62	0.55	0.22

† Station A012 on 9 September 2016 has data only from the vertical and one horizontal component. This was sufficient to provide data for template matching for detection. When applying the local magnitude formula, amplitude from the single horizontal component was used rather than a computed root sum square amplitude.

We began by using the identified event locations and magnitudes found using an autoregressive detection algorithm (D. Kim & Keranen, 2018) as a basis for template event selection. From this preliminary catalog of events, templates were selected to represent the densest region of identified earthquakes. Because station spacing was small relative to preliminary indications of the fault length, multiple templates were used to allow for the variations in waveforms resulting from differing azimuthal angles from aftershocks to a station. The selected template events all had magnitudes identified by Kim and Keranen (2018) as being above M1.5, which we chose in order to ensure strong signal-to-noise ratios. Data was bandpass filtered from 4-40 Hz for detection of low-magnitude, high-frequency events at close range. We snipped waveforms around the body waves for each selected template, with template durations ranging from 2-6 seconds depending on the specific event and station. Each template waveform was cut to begin 0.5 seconds prior to the P-wave arrival time.

We selected correlation thresholds independently for each template, station, and component. Each threshold was based on the method of correlating the time-reversed template against a nominal day of data to identify the correlation coefficients possible due simply to noise (Slinkard et al., 2014). We used the 99.99th percentile of the distribution of all coefficients from the time-reversed template to remove the possibility of extreme false detections artificially raising thresholds unnecessarily.

For each template event, each component of a station is correlated against all available station data for the 33-day deployment for that component. All times of a correlation coefficient exceeding that station and component's specific threshold were recorded

and saved for further analysis. Those detection times were then compared across components, different templates at a station, and finally for all stations to determine the final list of aftershock events. Aftershocks were defined as those events that were detected by any component with any template at a minimum of four separate stations. A total of 25,005 aftershocks were identified in 33 days based on these criteria.

Detections within 1 second of each other on a single component were considered to be the same event, to account for varying event-to-station travel times. We next use a logical code to compare event detections from different templates at the same station. Duplicate detections of the same event were identified as two detections within one second at the same station. In this case, the earliest time of detection is retained. Next, the code compares detection times within one second for all stations and assembles a list of those that occur on at least four stations. The times of detections per station and times of detections seen on at least four stations are retained, with the latter considered the official list of aftershocks.

Randomly selected detections were plotted for manual inspection to confirm the validity of the detection algorithm. This confirmed that the detections marked by template matching had waveforms that would be categorized as earthquakes based on the observed vertical and horizontal signals, corresponding to P-wave and S-wave motions.

2. Location Search

We assembled P-pick times for each of the stations with a detection time for an aftershock. We began with a preliminary estimate of P-arrival based on the detection time plus 0.5 seconds to account for the time between the start of the template and the template's P-arrival. We took ± 0.5 seconds of vertical component data around the estimated P-arrival and cross-correlated it with ± 0.5 seconds of vertical component data around the P-pick of the template. The peak correlation lag time allows us to optimize our P-pick time for that station derived from the template used for detection. This process is repeated for all templates that had a detection for the aftershock at that station, and the P-pick time with the highest correlation value is retained.

We use a grid search method to determine event locations. The search was centered on the mean latitude and mean longitude of the station locations and extended 10 km to the north, east, and west of the grid center, and 12.5 km to the south. We searched using grid spacing of 100 m horizontally and depth increments of 100 m between 0.1 and 16 km depth. For each grid location (latitude, longitude, depth), we used a crustal velocity model for Oklahoma to predict the P- and S- travel times from the grid point to each network station.

As in Chapter 2, we determined the optimal locations based on the minimum residual between the observed travel times from P- and S-picks and the predicted travel times from each grid location to a station (Section 2.3.2, equations 2.1 and 2.2). The horizontal location with the least residual was determined for each depth in the grid

search, and the depth with the least residual was determined to be the optimal event location.

We used a crustal velocity model initially based on work by Schoenball and Ellsworth (2017). Layer velocities were modified in accordance with (Table 3.2). Although the corresponding V_S is given for each layer V_P , only V_P was used in our search, as we only used P-picks and no S-picks for locating the aftershocks. The top two surface sediment layers for our model were expanded using modeling by Stephenson et al. (2021) at station OK050.

Thickness (km)	V_P (km/s)	V_S (km/s)
0.0051	0.251	0.145
0.0361	1.068	0.617
0.2588	2.70	1.56
0.700	2.95	1.70
0.800	4.15	2.40
6.5	5.80	3.35
13	6.27	3.62
15	6.41	3.70
10	7.00	4.05
14	8.17	4.72
∞	8.32	4.81

Table 3.2: Crustal velocity model for central Oklahoma.

3. Local magnitude determination

We determined local magnitudes for all detected events by finding the converted Wood-Anderson horizontal seismogram amplitude. We use the formula for local magnitude in Oklahoma at short hypocentral distances provide by Greig et al. (2018), using a calibration to Richter magnitudes:

$$M_L = \log A + 1.596 \log R - 0.00175R - 0.1229 + S \quad 3.1$$

where S is an individual station correction term, A is equivalent Wood-Anderson amplitude, and R is the hypocentral distance in km.

4. Results

1. Locations

The grid search using optimal P-arrival time estimates resulted in the aftershock locations shown in Figure 3.4. All events that were located on the boundary of the search region are assumed to be part of general Oklahoma background seismicity and not related to the M5.8 aftershocks, and are therefore excluded from subsequent analyses. This leaves a catalog of over 24,200 aftershocks for analysis. We find that aftershocks follow a pattern of two intersecting faults, consistent with the work of X. Chen et al. (2017), in which the Sooner Lake fault was first identified.

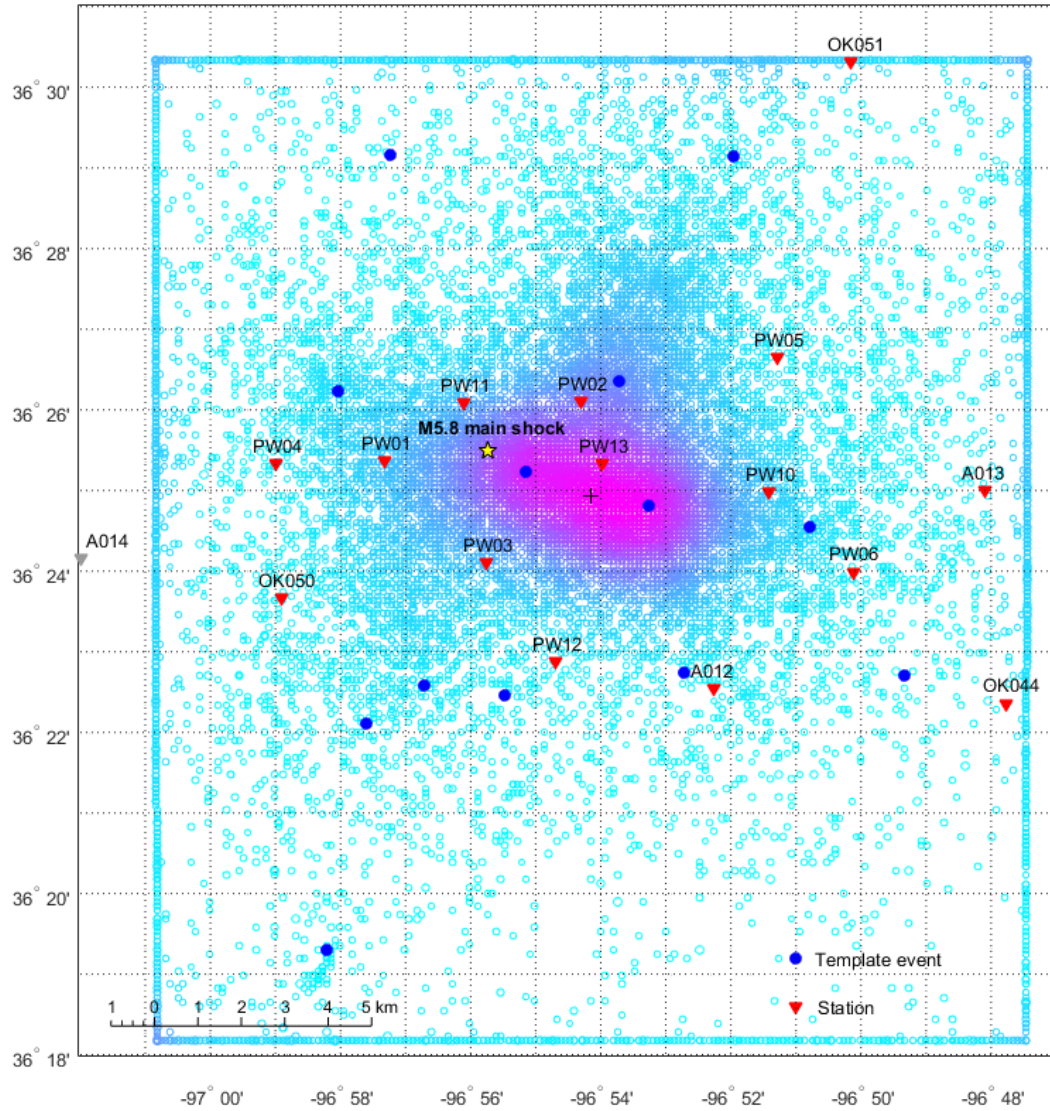


Figure 3.4: Map of detected aftershocks for the M5.8 Pawnee earthquake. The mainshock is shown with a yellow star. Stations are shown as red inverted triangles. Aftershocks used as template events are shown with large blue circles. The shading reflects the density of detected events in an area on the map; thus, the magenta region in the center has the largest concentration of aftershocks. The bounds of the grid used for location search are evident from earthquakes with locations placed on the outer edges. These events are likely located at greater distances in truth.

2. Frequency-magnitude distributions

The frequency-magnitude distribution (FMD) for the total network count of aftershocks detected on a minimum of four stations is shown in Figure 3.5. The combined magnitude of completeness is $M_c=0.2$ and the least-squares linear fit to the FMD is $\log(N)=4.09-1.03m$. The Aki (1965) maximum likelihood estimate for the b -value is 1.0394, with 95% confidence of $b = [1.0147, 1.0640]$, very close to the nominal value 1.0 (equation 1.3). There is consistency between the MLE estimator and the least-squares linear fit estimate for the b -value, confirming the result.

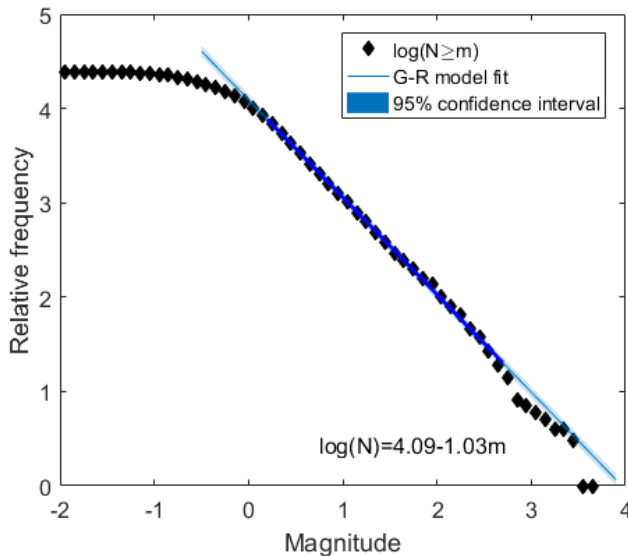


Figure 3.5: Frequency-magnitude distribution of detected aftershocks to the M5.8 Pawnee earthquake in November 2016.

The M5.8 Pawnee earthquake was followed by over 25,000 aftershocks in the subsequent six weeks, with the largest of these having a magnitude $M_L 3.60$. The difference between the largest aftershock and the mainshock, $\Delta m=2.2$, is well above the nominal difference predicted by Båth's Law of $\Delta m=1.2$.

By extrapolating the FMD we found above for the detected aftershocks, we were able to infer the largest notional aftershock we might expect to observe given the aftershock distribution (Shcherbakov & Turcotte, 2004). Using the Gutenberg-Richter relation

$\log_{10} N(\geq m) = a - bm$ and taking $N(\geq m^*) = 1$ for the largest nominal aftershock m^* (Shcherbakov & Turcotte, 2004), we applied our coefficients $a=4.09$ and $b=1.03$. The resulting nominal largest aftershock $m^*=3.97$ based on the FMD of all aftershocks is a little high compared to the observed largest magnitude $M_L3.60$, and still results in a somewhat large $\Delta m^*=1.83$.

The most probable maximum magnitude earthquake in a catalog with $N=25,000$ earthquakes, $M_C=0.2$, and $b=1.03$ is given by the equation

$$\hat{M}_{max} = M_C + \frac{1}{b} \log N \quad 3.2$$

(van der Elst et al., 2016). Unlike the previous formula, this accounts for the greater likelihood of detecting a large event with a large catalog size (which may be governed by duration of study or area or study region). Thus, given the detected aftershock population, the most likely maximum magnitude is $\hat{M}_{max} = 4.47$. By this formulation, the maximum expected to be observed is in line with Båth's Law, but the actual largest magnitude detected is 0.87 units lower.

We stacked the times of aftershock detection for each day of the temporary deployment and observed a peak in detection during the local night hours (Figure 3.6), consistent with other observations of increased detection with lower anthropogenic noise during

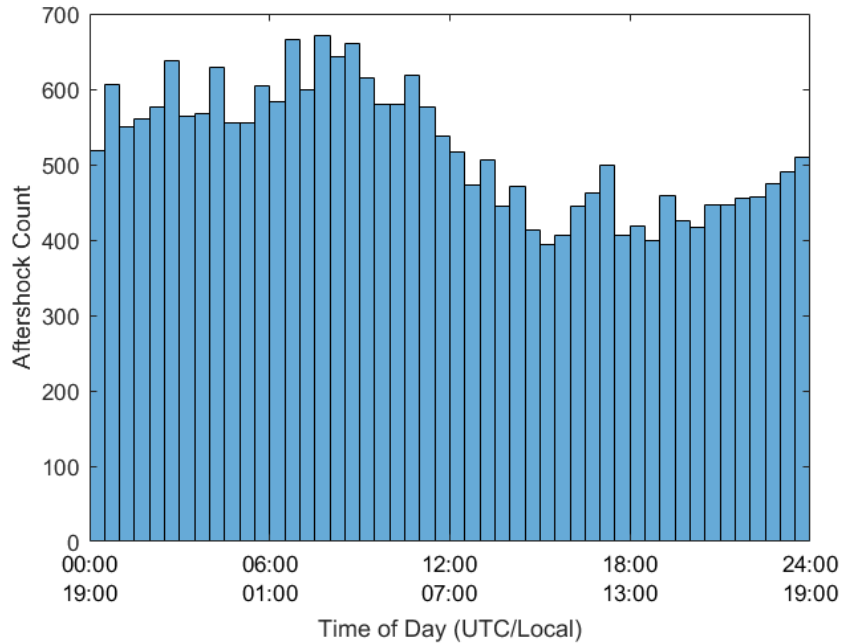


Figure 3.6: Histogram of aftershock time of day in UTC (top) and local time (bottom) for all aftershocks detected on at least 4 stations in the 33-day deployment.

the night (Boese et al., 2015; Green et al., 2017; Groos & Ritter, 2009; McNamara & Buland, 2004). By splitting the catalog into local night (00:00-12:00 UTC or 19:00-07:00 Central Daylight Time (USA) UTC-5) and local day, we can observe the higher relative frequencies of detection, although both groups still have an optimal magnitude of completeness $M_C=0.2$. (Figure 3.7).

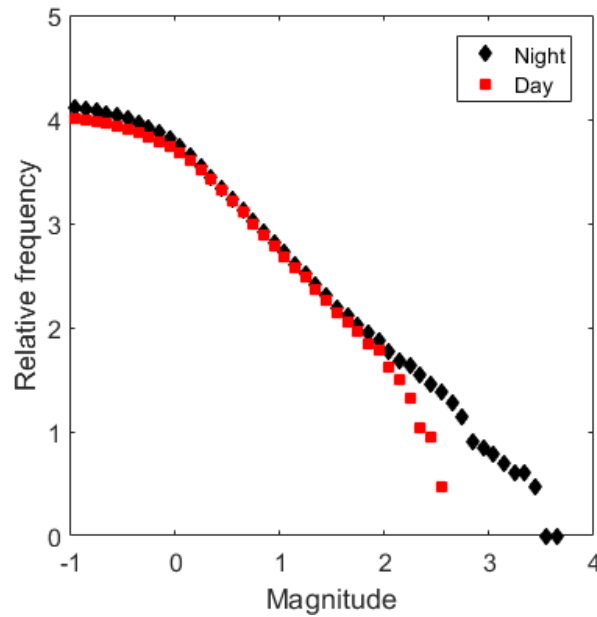


Figure 3.7: FMD for local night (black diamonds) and local day (red squares). Both have $M_c=0.2$, but the night time figure shows slightly higher detections for $M<0$ and for $2.2<M<3.2$.

2. Aftershock decay

The effects of the Omori-Utsu (Omori, 1895a; Utsu, 1961) aftershock decay following the Pawnee earthquake is evident in the daily count of earthquakes. However, this count is also affected by the stations' operation, as greater station availability increases the chances of having four stations able to detect an aftershock. In Figure 3.8, we show the daily count of detections for each individual station. Figure 3.8 also shows the total number of aftershocks detected by at least four network stations (Table 3.1). The total count reflects drops in the total number of detected aftershocks corresponding with days when fewer stations were operational, such as the 1st, 11th, 23rd, and final days of the temporary deployment.

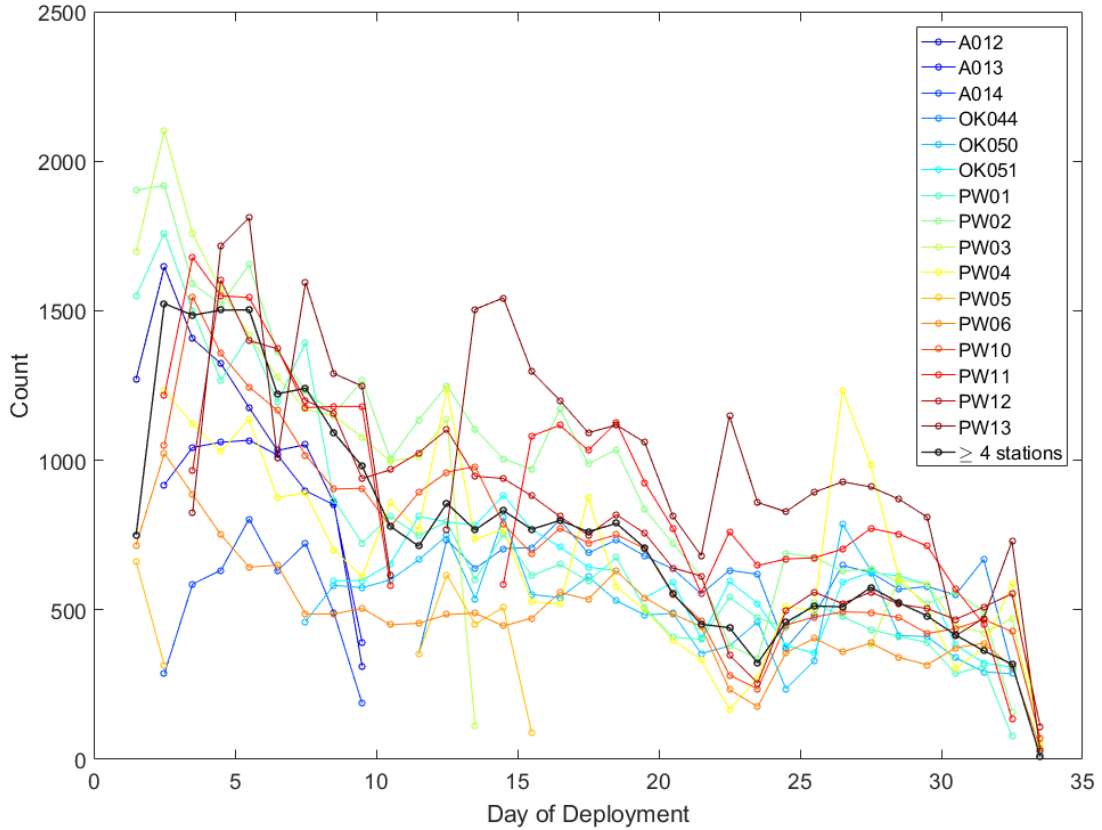


Figure 3.8: Daily count of detected aftershocks per broadband station (colored markers) and scaled (see text) daily count of aftershocks detected on at least 4 stations (black markers). The daily count of aftershocks detected at ≥ 4 stations is smoothed by the scaling to account for nonoperational stations and stations with partial days of operation, such as stations OK044, OK050, and OK051 on day 25 of the deployment. The raw counts for these three stations appears low on day 25 reflecting the data gap that prohibited detection for much of the day.

We use a Bayesian Markov Chain Monte Carlo approach (Appendix 2:) to model aftershock decay with the Reasenberg and Jones (1989) model (equation 3.3).

$$\lambda = \frac{10^{a-b(M_{main}-M_c)}}{(t+c)^p} \quad 3.3$$

The modeling of aftershock decay including all detected aftershocks resulted in parameters that are further from the anticipated range based on previous work (Table

2.5). By removing those events located on the outer edge of the grid search region, we are able to recover an improved ensemble of solutions. This set of parameters compares more favorably with those presented by Page et al. (2016) and Ebel (2009) (Table 2.5). This further supports our understanding of the grid-boundary located events as part of Oklahoma background seismicity and not part of the Pawnee aftershock sequence.

	Including grid boundary	Excluding grid boundary
a	-2.775 ± 0.102	-2.628 ± 0.120
b	1.036 ± 0.017	1.092 ± 0.021
p	0.915 ± 0.023	0.752 ± 0.020

Table 3.3: Mean and 95% confidence interval for the ensemble solution for parameters $\{a, b, p\}$. Left column is solution including all detected aftershocks; right column excludes those detected and located on the grid search boundary (Figure 3.4).

5. Discussion

Unlike induced seismic swarms, where geographic migration of earthquakes relative to a well location is evident and corresponds to pore fluid diffusion (X. Chen et al., 2012; Keranen et al., 2013, 2014), the Pawnee aftershocks do not exhibit any strong migration. This is consistent with a behavior more like tectonic aftershock catalogs rather than a catalog of earthquakes themselves individually induced directly by wastewater injection. Although the mainshock can be linked to injection activities (X. Chen et al., 2017; Goebel et al., 2019; McGarr & Barbour, 2017), aftershocks are a secondary effect of injection but occur in a manner like tectonic aftershocks. This raises the significance of moderate magnitude injection-induced earthquakes, as they are shown to trigger aftershocks that can themselves be felt.

McGarr and Barbour (2017) identify differences in the Pawnee, Fairview, and Cushing sequences in Oklahoma, all of which occurred in 2016. Each large ($M \geq 5$) earthquake occurred at least a year after the peak in injection rate, but Pawnee and Cushing had much greater variability in the prior year than Fairview (McGarr & Barbour, 2017). Based on work by McGarr (2014), they show the cumulative volume injected in the decade prior to each earthquake is proportional to the cumulative seismic moment for each sequence. In Pawnee, the mainshock accounted for 99% of the cumulative moment, due to the low aftershock productivity. In contrast, the Fairview mainshock accounted for only 48% of the cumulative moment. Cushing's mainshock provided 71% of the total moment (McGarr & Barbour, 2017).

Goebel et al. (2019) studied the aftershock deficiency for Pawnee and Cushing as compared to Fairview. They propose that the difference depends on whether rapid mitigation efforts were put in place. In Pawnee and Cushing, mitigation to drop injection rates was quick, whereas in Fairview the drop in injection rate was minimal and only occurred after a couple months. Goebel et al. (2019) suggested that rapid mitigation explains the decrease in statewide seismicity in 2016 while the cumulative moment continued to rise. However, there were numerous foreshocks of the Fairview sequence contributing to the overall productivity and moment release. Therefore, even with greater post-mainshock mitigation, the sequence would still have had different characteristics than Pawnee or Cushing.

6. Conclusions

The M5.8 Pawnee, OK, earthquake is observed to have an unusual aftershock sequence. The largest aftershock is smaller than expected at $M_L 3.6$, and the overall productivity as shown by the Omori a value is lower than expected. There may be a slight relative excess of small events as seen by the b -value found from Bayesian modeling of the aftershock decay rate as compared to b -values seen in other studies for SCR aftershock sequences. However, the observed value is near 1 and therefore close the global average overall, and not exceptional overall. When excluding grid boundary events, the decay rate as given by the exponent p is lower than that seen by Ebel (2009) but comparable to the value reported by Page et al. (2016) (Table 2.5). This value is also within the confidence limits found for p for aftershocks to the M4.2 Delaware earthquake, though the latter had an even lower productivity overall.

Chapter 4: Determining Periodicity in Non-Homogeneous Catalogs

1. Introduction

Periodicities in earthquake catalogs can reveal the response of earthquakes to small, periodic stress changes and allow for inference of conditions on deep faults as a result of knowing those stress changes. In consequence, scientists have for years tried to determine whether periodicities exist within earthquake catalogs. These studies have ranged from global to local and have searched for the influence of both diurnal tides and seasonality as related to snowmelt or rainfall cycles. Presence of sensitivity to tides can give an indication of a region's overall stress state, as that sensitivity indicates a threshold stress where incremental changes due to tidal stresses are sufficient to cause an excess of earthquakes preferentially during those times of day.

Although for years the prevailing view was that tides do not trigger earthquakes (Knopoff, 1964; Schuster, 1897; Simpson, 1967; Vidale et al., 1998), recent improvements to earthquake catalogs have allowed detection of the influence of these stresses under certain circumstances. Shallow subduction zones with large tidal amplitudes, high pore fluid pressure, and low normal stress exhibit sensitivity to tidal stress changes (Cochran et al., 2004; Heaton, 1975). The timing of non-volcanic tremor and the seismic signature of episodic tremor and slip correlate with tidally induced shear stress (Rubinstein et al., 2008; Thomas et al., 2009).

Seasonality in earthquake occurrence has been observed in some regions and linked to groundwater recharge from snowmelt or rainfall (Birhanu et al., 2018; Jónsdóttir et al., 2007; Muço, 1995; Saar & Manga, 2003). Moreover, tectonic earthquake swarm events can be linked to seasonal variable stress loading (Braunmiller et al., 2014).

A commonly-employed method of testing for periodicity is the Schuster Test (Schuster, 1897). However, like most statistical tests it assumes a constant background rate, which makes the test invalid in cases where the seismicity is increasing due to external influences, such as Oklahoma, or cases where seismicity is decreasing, such as aftershock sequences. Heteroscedasticity is any condition in which the variability of the dependent variable changes in relation to the value of the predictor variable. It can also occur when a random variable population has subsets with different variabilities from one another. In cases of heteroscedasticity altering the underlying seismic rate function of a region, a straightforward application of the Schuster test cannot be used to meaningfully analyze periodicity in a full catalog of earthquakes.

Given an interest in determining when and how earthquakes are affected by periodic stress changes, developing methodologies to determine whether periodicities are present in seismic catalogs is of broad interest. In this chapter, I first introduce existing methods of Schuster (1897) and Ader and Avouac (2013), which I use as the baseline for testing whether periodicity is present in a catalog. I derive the expected value for the Schuster test $\ln(p)$ -value for the explicit cases when seismicity rates change linearly and exponentially with time (Appendix 4:). In the case of an Omori-type hyperbolic

(inverse with time) decay, an analytic solution to $E[\ln(p)]$ does not exist, but numerical solutions are possible.

2. Classic Periodicity Analysis

The Schuster test, as developed by Schuster (1897), and the Schuster spectrum of Ader and Avouac (2013) are commonly employed to determine whether variations in seismicity at specific periods are significant and whether any other potential periodicities exist within tested catalogs. The Schuster test involves calculating a phase angle between 0 and 2π for every event in a given catalog based on the time of event relative to the start of the catalog and a particular period being investigated. It then computes a probability of the observed distribution of phase angles occurring naturally rather than occurring due to the presence of periodicity in event timing at the period in question, designating this probability the Schuster p -value. In a purely random catalog, with sufficient events included, there will be a random, approximately equal distribution of events at every phase angle because of the random and on average equal distribution in time (Figure 4.1a). In contrast, a catalog with true periodicity will have an event excess at some phases and a corresponding event deficit at the remaining phases (Figure 4.1b). The p -value indicates the probability that the observed phase distribution occurred naturally; thus very small p -values correspond to highly unlikely cases and it can be concluded that the tested period is significant, or a true periodicity in occurrence times is present in the data.

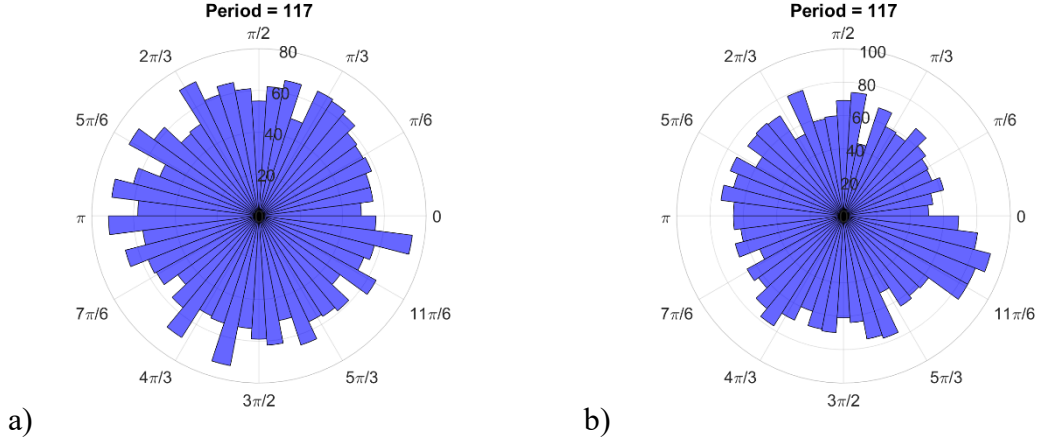


Figure 4.1: Example histograms of phase angle distributions for (a) non-periodic and (b) periodic synthetic catalogs. The non-periodic catalog has approximately equal distribution of phase angles for events and the net random walk will end near the origin. The periodic catalog has a bias toward a phase angle of $11\pi/6$ radians, resulting in the net random walk from all events ending some distance from the origin in that direction.

From Schuster (1897), for an event at time t_k , testing a period T , the phase angle for the event is

$$\theta_k = 2\pi \frac{t_k}{T} \quad 4.1$$

The distribution of all phase angles in the catalog behaves like a random walk, wherein the pure uniform distribution of phase angles will result in a net random walk ending reasonably near the origin. The distance of the random walk D comprised of N steps in directions θ_k is calculated as the norm of the sum of the cosines of θ_k and the sum of the sines of θ_k , as

$$D = \sqrt{\left(\sum_{k=1}^N \cos \theta_k\right)^2 + \left(\sum_{k=1}^N \sin \theta_k\right)^2} \quad 4.2$$

The probability that the resulting walk's distance from the origin is drawn from a uniform (non-periodic) occurrence rate is

$$p = e^{-\frac{D^2}{N}} \quad 4.3$$

where N is the number of events in the analyzed catalog and p is the p -value of the test (Schuster, 1897).

The expected value for the Schuster log probability for a single tested cycle depends only on the number of events in the catalog, N . This is because an increasing number of events increases the length of the random walk and consequentially, the likelihood that the walk ends far from the origin. The equation for this expected value is

$$\langle \ln p \rangle = -\frac{1 + N}{N} \quad 4.4$$

A Schuster spectrum will compute a total of m Schuster tests across the range (T_{min} , T_{max}), where δ_m is the minimum p -value of all m tests and $\langle \delta_m \rangle$ is the expected minimum p -value (Ader and Avouac, 2013). Given that $m \approx \frac{t}{T_{min}}$, where t is the total duration of the catalog, the authors show that $\langle \delta_m \rangle = \frac{T}{t}$. A Schuster p -value is therefore considered significant if it is smaller than $0.01 \cdot \langle \delta_m \rangle$, or below the 99% confidence level of this expected minimum level for a p -value, which is dependent on the specific period being tested.

Ader and Avouac (2013) acknowledge the challenges of testing individual periods and unintentionally obtaining false positives from the Schuster test through small p -values.

Their presentation of testing a full spectrum of values for T resolves this by providing a context for each significant p -value within the spectrum around it. The spectrum may, for example, range from 1/24 day (1 hour) to 365 days, When a substantial portion of the spectrum of tested periods show significance with very small p -values, the authors propose that these are a byproduct of other mechanisms in place within the analyzed catalog. They address the case of aftershocks and similar heteroscedastic earthquake rates skewing the spectrum of results to have numerous false positives, or artificially small p -values, and point out that significance cannot be assumed from the results.

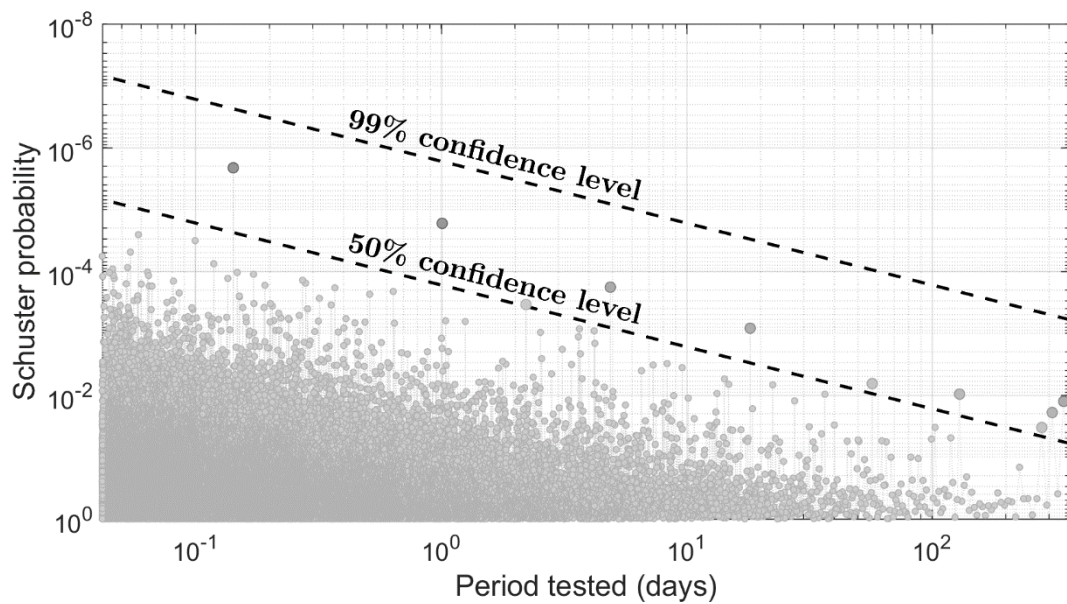


Figure 4.2: A synthetic catalog with a homogenous Poisson process earthquake rate has no significant periodicities detected at any period tested. The catalog has no background rate change and no periodic signature.

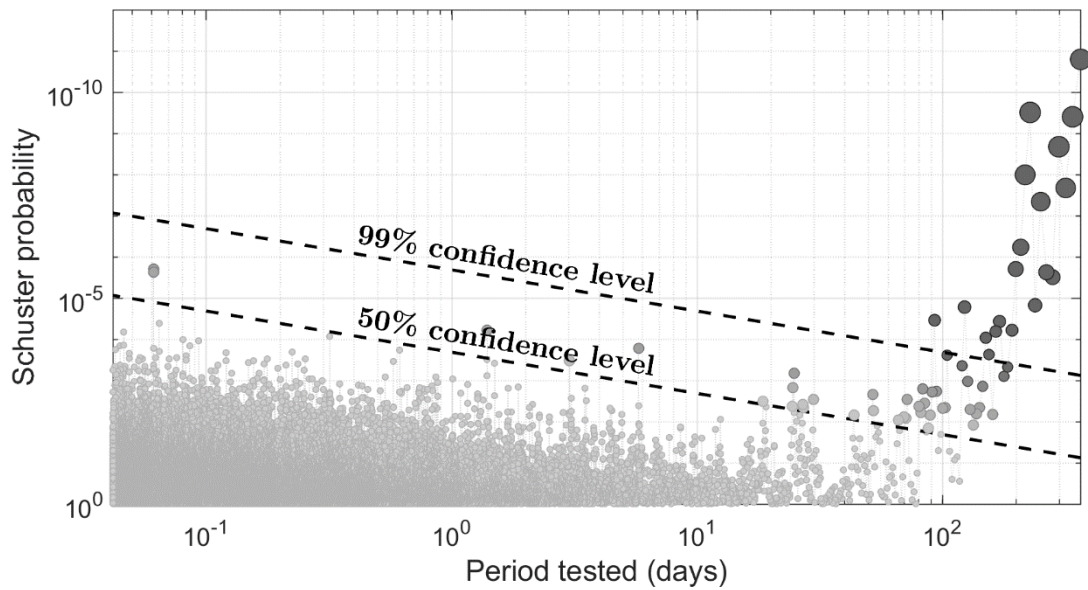


Figure 4.3: A synthetic catalog with an exponentially increasing background earthquake rate has numerous significant periodicities detected for long periods, despite known random non-periodic generation of event times.

The differences observed between a non-periodic catalog with no change in rate (Figure 4.2) and a synthetic exponentially increasing catalog (Figure 4.3; description of the generation of synthetic catalogs is provided in Appendix 3:) is clearly observed for periods longer than about 30 days for the examples given. In neither case is periodicity present in the synthetic data for any period, including any periods between 30 and 365 days. Naïve application of Schuster analysis to data sets similar to the example in Figure 4.3 can yield false positives for periodicity at varying time scales, particularly long periods, which is not consistent with natural physical mechanisms for these periods.

One of the key problems with an increasing earthquake rate is the way in which the changing number of events by definition forces an increasing distribution for larger

assigned phases when testing longer periods. For the tested period $T=365$ days, it is easy to see how fewer earthquakes will occur at the start of a year versus the end of the year given the increase in rate, leading to an increase in number of events for each phase angle increasing from 0 to 2π . However, all periods tested where the rate of increase is faster than the length of the period tested will show a similar increase between the calculated phases 0 and 2π .

The larger number of events assigned higher phase values (Figure 4.1b) results in the random walk distance from all events tending to grow as the sum of the sines of phases do not cancel (as they would for a homogeneous dataset). Correspondingly, as the random walk distance D grows, the p -value obtained from the test drops and is more likely to indicate significance at the 99% confidence level, regardless of true significance.

As the tested period decreases from the example maximum 365.25, the distribution of phase angles tends to become more even, because seismicity rate increases become negligible over short time periods. These periods are progressively less affected by the observation of false positives by the Schuster test.

3. Expected $\ln(p)$ values of Schuster Test

We analytically derive the expected value for the Schuster $\ln(p)$ -value in the cases where the underlying rate of events is first linearly increasing and then when it is

exponentially increasing, following the manner used by Ader and Avouac (2013) for sinusoidally varying seismicity. The full derivation is presented in Appendix 4:.

The expected value for $\ln(p)$ derived by Ader and Avouac (2013) for sinusoidally varying seismicity is:

$$\langle \ln p \rangle = -\frac{Na^2}{4} \quad 4.5$$

In the case of a strictly periodic catalog, the expected log-probability for a cycle T is a function solely of the amplitude of oscillation a and of the catalog number of events N .

For the case of the linear increase in event rate, the rate function will have a form of:

$$R(t_k) = C + at_k \quad 4.6$$

where a is the rate of change of the background earthquake rate and C is the initial rate at time 0. The sign of a will be positive or negative depending on whether the rate is increasing or decreasing. This results in an expected value for the probability following:

$$\langle \ln p \rangle = -1 - \frac{(N-1)a^2T^2}{\pi^2(2+aT)^2} \quad 4.7$$

where N is the number of events in a given analyzed catalog, as before, and T is the period being tested. In the case of a linearly changing rate, the Schuster test probability will be a function not only of N and the rate of change a , but also of the square of the period being tested, T . This can be related to the significant upward tail observed for longer periods tested on a non-homogeneous catalog.

Similarly, when we examine the case of an exponential increase in event rate, the rate of background seismicity will have the following form:

$$R(t_k) = e^{(\alpha+\beta t_k)} \quad 4.8$$

where α and β are the parameters describing the exponential growth or decay function.

This results in an expected value for the Schuster probability given by:

$$\langle \ln p \rangle = -\frac{4\pi^2 + NT^2\beta^2}{4\pi^2 + T^2\beta^2} \quad 4.9$$

The exponential case as seen in equation (4.9) presents the same situation as seen with the linearly changing seismicity rate, in which the expected value grows not only with N and the rate of increase β but also with the square of the period tested, T . This accounts for the significant upward tail observed in the figures such as Figure 4.3, where p -values grow extremely small for larger periods T . For $T < 1$ day, the catalog size typically remains the dominant factor in determining the p -value. Figure 4.4 shows these expected values for the Schuster $\ln(p)$ spectrum at a range of values for T and for notional rate increases, in the four respective cases of 1) constant rate, 2) sinusoidal (true periodic) rate, 3) linearly increasing rate, and 4) exponentially increasing rate.

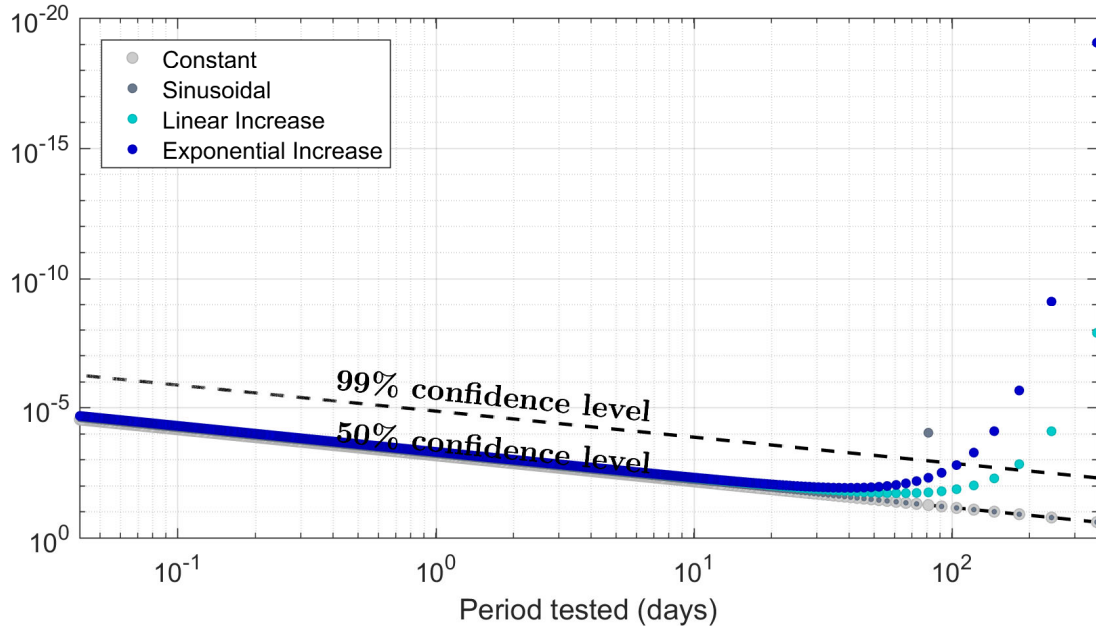


Figure 4.4: Sample $e^{(\ln p)}$ for different event rates. The rates of growth for the linear event rate, a , and the exponential event rate, β , are fixed for each given synthetic data set. Values for these parameters are for demonstration purposes, as is the selection of a sinusoid at $T=80$ days. All four synthetic catalogs are generated with the same number of events, N . The driver to the growth in $E[\ln(p)]$ is therefore the period being tested, T (equations 5.7 and 5.9).

We can easily see from the rate functions in equations (4.6) and (4.8) that when either rate change parameter a or β goes to zero, the resulting function $R(t)$ reduces to a constant baseline earthquake rate (in the linear case, C ; in the exponential case, $e^a=C$).

4. Discussion

Artificially significant p-values may be observed when using the Schuster test if there is a rate of increase or decrease in the catalog.

If the rate changes faster than the period being tested, then with sufficient sample size, the period will artificially appear significant. For example, when testing the

significance of a yearly periodicity and the rate has a significant difference from start to end over the course of a year, then the period will appear significant.

If the period being tested is short, such as a day (like for tidal periodicity), it is highly unlikely that an increase will occur in that short a time span, given the types of observed increases in seismic event detection (e.g., network coverage changes or induced earthquakes). If the period tested is short, but a rate decrease is occurring due to aftershock decay, the rate of detectable events may be observably different from 00:00 to 23:59, particularly in the first few days when the decline is steep. This could create a false positive when looking for tidal periods. The caveat, however, is that the decay only remains steep for a few days excepting great earthquakes. Due to this inherent data limitation, statistical tests may still avoid any false identification of the presence of short period signals.

The derived analytical solutions and numerical solutions only apply to cases when the rate follows a continuous, fixed rate function. We have described here solutions for the linear, exponential, and hyperbolic cases, though solutions could be derived for other rate functions. However, random, erratic changing rates or rates that increase or decrease with slopes that change over time, such as a piece-wise function, would not be well-modeled by the expected values for $E[\ln(p)]$ derived here. Nonetheless, the general principles described above regarding when one might expect to see false positives or not based on the slope of the rate change relative to the period being tested may still apply.

5. Conclusions

When the rate is changing at a scale faster than the periods of interest, investigators need to apply the method presented herein. If period of interest (hourly to daily) is below or similar to rate of change, the original Schuster spectrum will be sufficient as that portion of events will not be affected by the influence of the period T . Similarly, if the rate of change is sufficiently slow then even studies investigating periods on the order of months or years may not be affected. Naïve application of Schuster analysis can yield false positives for periodicity at varying time scales, particularly long periods when the rate change is observable over the duration of the period tested. When investigating periodicity, one must account for the expected bias in distribution of phases for events at each tested period resulting from the change in occurrence rate.

Chapter 5: Moderate Magnitude CEUS Earthquakes

1. Summary on other locations

1. 2015 Michigan M4.2

To help understand whether our observations of anomalously low aftershock productivity were unique to Delaware, we conducted a similar analysis for the aftershocks of the 2 May 2015 M4.2 earthquake outside Kalamazoo, MI. The same method of template matching was used on one month of data from the nearest permanent regional station (L46A). In this period, I did not detect any aftershocks at a station distance of about 75 km. Based on regional template matching done by Kim et al. (2018), where the nearest regional station was approximately 70 km from the mainshock epicenter, the magnitude of completeness at that distance should be approximately M1. Therefore, the failure to detect aftershocks to the Kalamazoo, MI, earthquake places an upper bound on the largest aftershock of about M1.

2. Highlights of all M4+ since 2000

Preliminary review of $M \geq 4$ earthquakes in the past ten years suggests that some have typical productivity sequences. These have a few dozen aftershocks recorded in ComCat and the largest aftershock close to 1.2 magnitude units below the mainshock magnitude, close to a nominal Båth's value (Various, 2021). Other CEUS mainshocks

will have few aftershocks with low magnitudes or no aftershocks recorded at all. Currently we lack understanding of the driving factors for this.

2. Areas for future research

1. Aftershock statistical parameters (b , a , c , p)

Following the introduction of a statistical model for aftershock rates by Reasenber and Jones in 1989, further research has shown that generic model parameters for California seismicity vary depending on the region within the state (Hardebeck et al., 2019). Because of this, it is likely that generic parameters for stable continental regions used for the entirety of the CEUS (e.g., Page et al., 2016) will not accurately model aftershock rates in varying regions encompassing several different intraplate seismic zones as well as earthquakes in stable continental interior regions outside of common seismic zones.

By testing the correlation of aftershock parameters for productivity (a), relative frequency of magnitudes (b), and speed of aftershock decay (p) with factors including fault type, stress drop, local stress field, and local 1D geology models to the hypocenter, it may be possible to better quantify starting models for aftershock forecasting based on these factors for a new mainshock. Lack of correlations will allow better quantification of the uncertainty in the model parameters.

2. Waveform cross correlation to expand detection of aftershocks

In intraplate regions with low seismicity, increased detection of earthquakes is particularly important. Without frequent earthquakes to develop a robust catalog to analyze and model for parameters in governing laws such as the Gutenberg-Richter Law and Omori's Law, these intraplate regions of the CEUS have forecasts that remain largely dependent on parameters from generalized areas, which may not accurately reflect their unique environment and therefore will be less accurate. Methods such as template matching allow improved detection of small earthquakes to provide and expand aftershock catalogs, thereby providing the necessary data to model within each region individually (Frank & Abercrombie, 2018; Gibbons & Ringdal, 2006; Schaff & Waldhauser, 2010).

Applying methods of template matching for earthquake detection can build improved aftershock catalogs for additional moderate magnitude earthquakes in a range of tectonic and geologic settings across the CEUS. The method of template matching can lower the magnitude of completeness for a study region by one or more magnitude units, depending on the availability and proximity of regional stations.

3. Categorizing CEUS events

Future research suited to extend this dissertation would include work toward improving the understanding of aftershock parameters displayed throughout the CEUS. Establishing a suite of aftershock parameters based on any governing factors (e.g., geology, fault type, event depth, stress drop, and stress alignment) would allow USGS

Operational Aftershock Forecasts to use better initial parameters in their aftershock forecasting rather than broadly generic ones for stable continental regions (“Aftershock Forecast Overview,” n.d.; van der Elst et al., 2020; Field et al., 2016; Michael et al., 2019; Thompson et al., 2019)

Figure 5.1 shows magnitude 4 and greater earthquakes from 2001-2020 in Eastern North America, including 34 in the United States and six in Canada, and the nearest permanent seismic stations to a selection of these U.S. events.

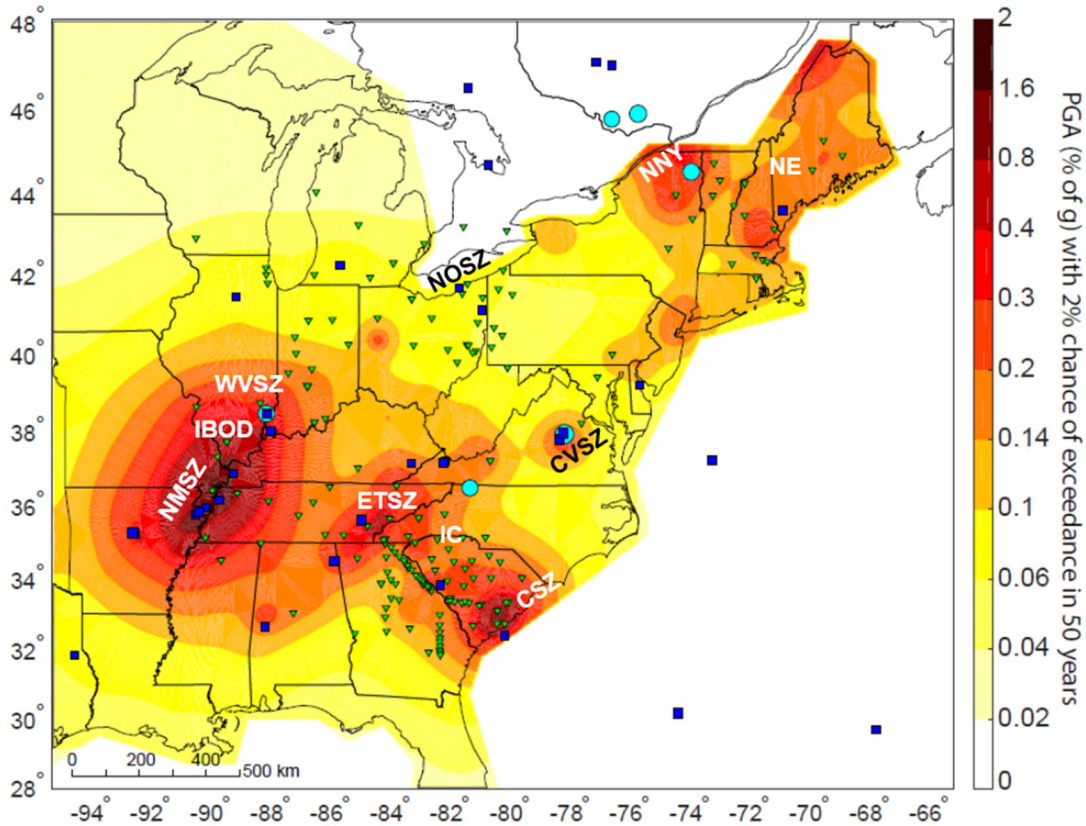


Figure 5.1: $M \geq 4$ earthquakes in the Eastern US and Canada from 2001-2020 (Various, 2021). Size of marker is proportional to magnitude of event, with cyan circles showing $M \geq 5$ and greater events and blue squares showing $4 \leq M < 5$ events. Inverted triangles show 3-component network stations within 2 degrees of earthquakes selected for template matching analysis. Shading on the map indicates the 2% probability of exceedance in 50 years peak ground accelerations for site class D from the National Hazard model (Rukstales & Petersen, 2019). Full names of region abbreviations appear in Table 3.

A selection of the $M \geq 4$ earthquakes shown in Figure 5.1 and within the U.S. is listed in Table 5.1 with the date and depth of each event. Certain M4-M5 events are excluded for various reasons as follows:

- The earthquakes occurring in central Arkansas are part of the Guy-Greenbrier earthquake swarm sequence, a result of wastewater injection and an area that has previously been studied in great detail with a catalog that can be leveraged for purposes of comparisons between aftershock parameters (Horton, 2012; Huang & Beroza, 2015).
- $M \geq 4$ aftershocks within one year of larger mainshocks (such as in the case of Mineral, VA) are excluded from recommended primary analysis.

By building a database of aftershock catalogs and modeling the parameters for each, one could characterize the spatial variability observed in aftershock sequences. The improved magnitude of completeness in detected aftershocks may refine the b -values of the Gutenberg-Richter relation in each location. In various other studies throughout the world, some aftershock sequences or regions have been shown to have b -values below 1, indicating an excess of larger magnitude events (Schorlemmer et al., 2005; Wiemer & Wyss, 2002). In contrast, other sequences have b -values above 1, indicating a relative excess of smaller magnitude events.

Epicenter	Region	Magnitude	Depth
Weber City, Virginia	Central Virginia Seismic Zone	4.5	10.0
South Carolina	Charleston Seismic Zone	4.0	2.4
Decatur, Tennessee	Eastern Tennessee Seismic Zone	4.4	7.9
Mount Vernon, Indiana	Illinois Basin - Ozark Dome	4.6	16.1
Edgefield, South Carolina	Inland Carolinas	4.1	5.2
Southern Maine	New England	4.7	16.1
Blytheville, Arkansas	New Madrid Seismic Zone	4.0	23.7
Eastlake, Ohio	Northeast Ohio Seismic Zone	4.0	2.0
New York - Adirondacks	Northeastern New York	5.3	4.8
Eutaw, Alabama	Stable Continental Region	4.3	5.0
West Virginia	Stable Continental Region	4.3	1.0
Ottawa, Illinois	Stable Continental Region	4.2	10.0
Galesburg, Michigan	Stable Continental Region	4.2	4.5
Mount Carmel, Illinois	Wabash Valley Seismic Zone	5.2	14.3
Mineral, Virginia	Central Virginia Seismic Zone	5.8	6.0
Fort Payne, Alabama	Eastern Tennessee Seismic Zone	4.6	19.8
Hazard, Kentucky	Eastern Tennessee Seismic Zone	4.2	17.0
Virginia-N. Carolina border	Inland Carolinas	5.1	4.1
Manila, Arkansas	New Madrid Seismic Zone	4.2	10.0
Caraway, Arkansas	New Madrid Seismic Zone	4.1	15.5
Bardwell, Kentucky	New Madrid Seismic Zone	4.0	2.5
Ridgely, Tennessee	New Madrid Seismic Zone	4.0	15.0
Youngstown-Akron, Ohio	Northeast Ohio Seismic Zone	4.0	5.0
Greenbrier, Arkansas	Stable Continental Region	4.3	7.7
Timpson, Texas	Stable Continental Region	4.1	5.0

Table 5.1: Magnitudes and hypocentral locations of 25 CEUS earthquakes plotted in Figure 5.1, excluding M4+ aftershocks of larger events in this list, as well as the Guy-Greenbrier, AR, sequence and the 2017 Delaware earthquake (previously analyzed). Shaded events are in duplicate regions and would serve to improve understanding and resolve bounds on aftershock parameters, but studies of the first 14 events to encompass a wide variety of regions are recommended first.

A selection of the events from Table 5.1 are listed in Table 5.2 with a summary of aftershock activity as observed from ANSS ComCat (Various, 2021). The difference

between the mainshock magnitudes and their largest aftershocks varies, with some of these CEUS events fitting with Båth’s Law and others in great contrast, as was shown in Delaware in Chapter 2. Productivity also varies within this selection of detected aftershocks.

Time	Depth (km)	Event Location	M_w	Largest Aftershock	Δm	N
8/9/2020 12:07:37	7.58	North Carolina-Virginia	5.1	3.2	1.9	79
6/10/2019 14:50:44	2	Ohio-Eastlake	4.0	2.6	1.4	7
12/12/2018 09:14:43	7.87	Tennessee-Decatur	4.4	3.0	1.1	13
5/2/2015 16:23:06	1.6	Michigan-Galesburg	4.2		>3.2	0
2/15/2014 03:23:38	8.2	South Carolina-Edgefield	4.1	3.0	1.1	1
11/10/2012 17:08:13	17.1	Kentucky-Hazard	4.2	2.7	1.5	9
10/16/2012 23:12:23	10	Maine	4.67	2.7	2.0	1
12/31/2011 20:04:57	5.4	Ohio-Youngstown	4.0		>3.0	0
8/23/2011 17:51:03	7.7	Virginia-Mineral	5.8	4.5, 4.2	1.3	43

Table 5.2: CEUS earthquakes with $M \geq 0$ since 2010, shown with respective depth, magnitude, largest aftershock magnitude, and number of aftershocks in ComCat.

Only through studying multiple aftershock sequences can one fully identify what may be a natural variation and what is a distribution centered higher or lower than 1. With improved constraints on b -value variations, one can identify areas more or less prone to large magnitude aftershocks and tailor communications to the public accordingly. Constraints on a decay sequence p parameter helps forecasters understand how long a region may expect to continue to experience aftershocks, and the productivity of the sequence will guide communications on how many aftershocks in general are expected.

3. Conclusions

CEUS earthquakes are observed to have aftershock sequences that behave differently not only from California and other tectonic regions, but also from each other within the CEUS. Analysis is further complicated by low station coverage. With only one or two magnitude units covered by standard catalog completeness, analysis capacity is limited. Waveform correlation is a recognized method to improve event detection in these regions. Furthermore, when temporary networks are deployed following a moderate magnitude mainshock, delays in installation and operational challenges with temporary stations can lead to heterogeneous network coverage even at the local range.

This area of research has much that can be done to expand studies and improve understanding of aftershock characteristics in the intraplate U.S. setting. Recent events are a good starting point for analysis, given their inherent better data coverage and access. However, in the future, this could even be expanded to include analysis of many moderate magnitude earthquakes from throughout the 20th century if analog data digitization efforts are successful (Richards & Hellweg, 2020)

Appendix 1: Tables of P- and S-picks: M4.2 Delaware Aftershocks

Table A1.1: Table of P-picks for detected aftershocks to the M4.2 Delaware 30 November 2017 mainshock.

Index	DVN1	DVN2	DVN3	DVN4	DVN5	DVN12	DVN13	DVN14	DVN15	DVN16	DVB1	DVB2	DVB3	DVB4
1	--	--	12/01/2017 21:41:36.313	12/01/2017 21:41:35.607	--	--	--	--	--	--	--	12/01/2017 21:41:34.966	--	--
2	--	--	--	--	--	--	--	--	--	--	--	12/01/2017 21:59:52.659	--	--
3	--	--	12/01/2017 23:27:34.585	--	12/01/2017 23:27:34.800	--	--	--	--	--	--	12/01/2017 23:27:33.188	--	--
4	--	--	--	--	--	--	--	--	--	--	--	12/02/2017 00:16:08.226	--	--
5	--	--	--	--	12/02/2017 00:24:35.308	--	--	--	--	--	--	12/02/2017 00:24:32.610	--	--
6	--	--	12/02/2017 00:57:42.754	12/02/2017 00:57:41.514	12/02/2017 00:57:43.001	--	--	--	--	--	--	12/02/2017 00:57:41.303	--	--
7	--	--	--	--	--	--	--	--	--	--	--	12/02/2017 03:12:15.063	--	--
8†	--	--	12/02/2017 10:24:47.155	12/02/2017 10:24:46.426	12/02/2017 10:24:47.455	--	--	--	--	--	--	12/02/2017 10:24:45.847	--	--
9	--	--	--	--	--	--	--	--	--	--	--	12/02/2017 12:39:21.573	--	--
10	--	--	12/02/2017 14:36:16.925	12/02/2017 14:36:16.763	12/02/2017 14:36:17.182	--	--	--	--	--	--	12/02/2017 14:36:15.574	--	--
11	--	--	--	--	--	--	--	--	--	--	--	12/02/2017 16:33:16.648	--	--
12	--	--	--	12/02/2017 16:57:41.049	--	--	--	--	--	--	--	12/02/2017 16:57:39.792	--	--
13	--	--	12/02/2017 18:38:45.714	12/02/2017 18:38:44.940	12/02/2017 18:38:45.821	--	--	--	--	--	--	12/02/2017 18:38:44.313	--	--
14	--	--	--	--	--	--	--	--	--	--	--	12/02/2017 19:13:15.936	--	--
15	--	--	--	12/03/2017 01:24:00.393	--	--	--	--	--	--	--	12/03/2017 01:23:59.025	--	--
16	--	--	--	--	--	--	--	--	--	--	--	12/03/2017 14:25:06.847	--	--

17	--	--	--	--	--	--	--	--	--	--	--	12/03/2017 14:38:37.575	--	--
18	--	--	12/04/2017 02:31:29.202	12/04/2017 02:31:28.426	12/04/2017 02:31:28.416	--	--	--	--	--	--	12/04/2017 02:31:27.785	--	--
19	--	--	--	--	--	--	--	--	--	--	--	12/04/2017 08:41:28.427	--	--
20	--	--	--	--	--	--	--	--	--	--	--	12/04/2017 09:24:19.338	--	--
21	--	--	12/04/2017 12:13:41.849	12/04/2017 12:13:41.626	12/04/2017 12:13:42.056	--	--	--	--	--	--	12/04/2017 12:13:40.435	--	--
22	--	--	12/04/2017 19:10:39.430	--	--	--	--	--	--	--	--	12/04/2017 19:10:38.044	--	--
23	--	--	12/05/2017 01:24:01.816	12/05/2017 01:24:01.140	12/05/2017 01:24:02.128	--	--	--	--	--	--	12/05/2017 01:24:00.437	--	--
24	--	--	--	--	--	--	--	--	--	--	--	12/05/2017 10:24:24.672	--	--
25	--	--	--	--	--	--	--	--	--	--	--	12/05/2017 13:31:11.629	--	--
26	--	--	--	--	--	--	--	--	--	--	--	12/05/2017 22:23:35.450	--	--
27	--	--	12/06/2017 03:30:11.570	12/06/2017 03:30:11.449	--	--	--	--	--	--	--	12/06/2017 03:30:10.150	--	--
28	--	--	--	--	--	--	--	--	--	--	--	12/06/2017 13:55:12.576	--	--
29	--	--	--	12/07/2017 00:09:29.247	12/07/2017 00:09:30.250	--	--	--	--	--	--	12/07/2017 00:09:28.622	--	--
30	--	--	12/07/2017 00:44:03.885	12/07/2017 00:44:03.580	12/07/2017 00:44:04.138	--	--	--	--	--	--	12/07/2017 00:44:02.535	--	--
31	--	--	--	12/07/2017 01:49:07.881	12/07/2017 01:49:08.919	--	--	--	--	--	--	12/07/2017 01:49:07.309	--	--
32	--	--	--	--	--	--	--	--	--	--	--	12/07/2017 01:54:49.790	--	--
33	--	--	--	--	--	--	--	--	--	--	--	12/07/2017 10:33:44.396	--	--
34	--	--	12/07/2017 18:53:55.181	--	12/07/2017 18:53:55.391	--	--	--	--	--	--	12/07/2017 18:53:53.771	--	--
35	12/07/2017 19:39:45.108	--	12/07/2017 19:39:41.875	12/07/2017 19:39:41.061	12/07/2017 19:39:42.080	--	--	--	--	--	--	12/07/2017 19:39:40.454	--	--
36	--	--	--	12/08/2017 06:14:12.079	--	--	--	--	--	--	--	12/08/2017 06:14:11.718	--	--
37	--	--	12/08/2017 12:17:50.993	--	12/08/2017 12:17:51.250	--	--	--	--	--	--	12/08/2017 12:17:49.640	--	--

38	--	--	12/08/2017 14:19:51.961	--	12/08/2017 14:19:52.151	--	--	--	--	--	--	12/08/2017 14:19:50.556	--	--
39†	12/09/2017 19:27:04.571	--	12/09/2017 19:27:01.194	12/09/2017 19:27:00.563	12/09/2017 19:27:01.604	--	--	--	--	--	--	12/09/2017 19:26:59.896	--	--
40	--	--	12/09/2017 20:26:20.723	12/09/2017 20:26:20.657	--	--	--	--	--	--	--	12/09/2017 20:26:19.380	--	--
41	--	--	--	--	--	--	--	--	--	--	--	12/10/2017 20:17:24.737	--	--
42	--	--	--	--	--	--	--	--	--	--	--	12/11/2017 05:45:06.317	--	--
43	--	--	--	--	--	--	--	--	--	--	--	12/11/2017 20:11:44.167	--	--
44‡	12/11/2017 22:02:45.406	12/11/2017 22:02:44.745	12/11/2017 22:02:42.230	12/11/2017 22:02:41.412	12/11/2017 22:02:42.465	12/11/2017 22:02:45.114	--	12/11/2017 22:02:44.038	--	--	--	12/11/2017 22:02:40.835	12/11/2017 22:02:43.758	12/11/2017 22:02:45.498
45	--	--	--	--	--	--	--	--	--	--	--	12/11/2017 23:42:04.854	--	--
46	--	--	--	12/12/2017 04:24:59.257	12/12/2017 04:25:01.446	--	--	--	--	--	--	12/12/2017 04:24:58.863	--	--
47	--	--	--	--	--	--	--	--	--	--	--	12/12/2017 07:20:36.661	--	--
48‡	12/13/2017 00:45:30.007	12/13/2017 00:45:29.379	12/13/2017 00:45:26.856	12/13/2017 00:45:26.037	12/13/2017 00:45:27.077	--	12/13/2017 00:45:29.592	12/13/2017 00:45:28.577	--	12/13/2017 00:45:31.352	--	12/13/2017 00:45:25.456	--	12/13/2017 00:45:30.098
49	--	--	--	--	--	--	--	--	--	--	--	12/13/2017 13:58:12.189	--	--
50	--	--	--	--	--	--	--	--	--	--	--	12/13/2017 22:03:39.759	--	--
51	--	--	--	--	--	--	--	--	--	--	--	12/14/2017 02:14:50.378	--	--
52	--	--	--	--	--	--	--	--	--	--	--	12/14/2017 08:13:38.960	--	--
53	--	--	--	12/14/2017 13:50:32.703	--	--	--	--	--	--	--	12/14/2017 13:50:31.291	--	--
54	--	--	12/14/2017 17:50:53.969	12/14/2017 17:50:53.688	--	--	--	--	--	--	--	12/14/2017 17:50:52.537	--	--
55	--	--	--	--	--	--	--	--	--	--	--	12/14/2017 21:56:08.361	--	--
56†	12/14/2017 23:09:56.227	--	12/14/2017 23:09:52.870	12/14/2017 23:09:52.099	--	--	--	--	--	--	--	12/14/2017 23:09:51.560	--	--
57	--	--	12/15/2017 00:47:54.662	--	--	--	--	--	--	--	--	12/15/2017 00:47:53.361	--	--
58	--	--	--	--	--	--	--	--	--	--	--	12/15/2017 01:54:19.206	--	--

59†	--	--	--	12/15/2017 07:24:11.600	12/15/2017 07:24:12.637	--	--	--	--	--	--	12/15/2017 07:24:10.992	--	--
60	--	--	--	--	--	--	--	--	--	--	--	12/15/2017 22:20:46.865	--	--
61	--	--	--	--	--	--	--	--	--	--	--	12/16/2017 01:15:03.628	--	--
62	--	--	--	--	--	--	--	--	--	--	--	12/16/2017 07:29:09.678	--	--
63	--	--	--	--	--	--	--	--	--	--	--	12/16/2017 11:35:59.055	--	--
64†‡	12/17/2017 14:58:48.697	12/17/2017 14:58:48.069	12/17/2017 14:58:45.531	12/17/2017 14:58:44.732	12/17/2017 14:58:45.766	12/17/2017 14:58:48.428	12/17/2017 14:58:48.278	12/17/2017 14:58:47.374	12/17/2017 14:58:49.940	12/17/2017 14:58:50.098	--	12/17/2017 14:58:44.157	12/17/2017 14:58:46.948	12/17/2017 14:58:48.792
65‡	12/17/2017 16:07:10.246	12/17/2017 16:07:09.530	12/17/2017 16:07:06.963	12/17/2017 16:07:06.283	12/17/2017 16:07:07.303	12/17/2017 16:07:10.063	--	12/17/2017 16:07:08.902	12/17/2017 16:07:11.680	--	--	12/17/2017 16:07:05.622	12/17/2017 16:07:08.515	12/17/2017 16:07:10.337
66	--	--	--	--	12/18/2017 08:37:57.674	--	--	--	--	--	--	12/18/2017 08:37:56.255	--	--
67	--	--	--	--	--	--	--	--	--	--	--	12/18/2017 08:38:05.176	--	--
68	--	--	12/19/2017 10:35:01.832	12/19/2017 10:35:01.154	12/19/2017 10:35:02.150	--	--	--	--	--	--	12/19/2017 10:35:00.464	--	--
69	--	--	--	--	--	--	--	--	--	--	--	12/19/2017 13:35:46.237	--	--
70	--	--	12/23/2017 00:57:48.599	12/23/2017 00:57:47.980	12/23/2017 00:57:49.011	--	--	--	--	--	--	12/23/2017 00:57:47.313	--	--
71	--	--	--	--	--	--	--	--	--	--	--	12/23/2017 05:48:52.188	--	--
72	12/23/2017 13:29:56.453	--	12/23/2017 13:29:53.184	12/23/2017 13:29:52.427	12/23/2017 13:29:53.406	--	--	--	--	--	--	12/23/2017 13:29:51.775	--	--
73‡	--	--	12/23/2017 16:21:53.940	12/23/2017 16:21:53.096	12/23/2017 16:21:54.162	--	--	--	--	--	--	12/23/2017 16:21:52.543	--	--
74	--	--	--	--	--	--	--	--	--	--	--	12/24/2017 11:53:09.155	--	--
75	--	--	--	--	--	--	--	--	--	--	--	12/27/2017 13:20:09.248	--	--
76	--	--	12/27/2017 14:11:47.214	12/27/2017 14:11:46.332	12/27/2017 14:11:47.392	--	--	--	--	--	--	12/27/2017 14:11:45.771	--	--
77	--	--	12/27/2017 14:32:25.747	--	12/27/2017 14:32:25.956	--	--	--	--	--	--	12/27/2017 14:32:24.316	--	--
78	--	--	--	--	--	--	--	--	--	--	--	12/27/2017 23:36:31.231	--	--
79	--	--	12/28/2017 05:39:24.899	12/28/2017 05:39:24.720	12/28/2017 05:39:25.408	--	--	--	--	--	--	12/28/2017 05:39:23.780	--	--

80	--	--	12/28/2017 09:42:27.475	12/28/2017 09:42:26.668	12/28/2017 09:42:27.696	--	--	--	--	--	--	12/28/2017 09:42:26.023	--	--
81	--	--	--	--	--	--	--	--	--	--	--	12/29/2017 06:31:51.340	--	--
82†	--	--	12/31/2017 00:11:21.492	12/31/2017 00:11:20.672	12/31/2017 00:11:21.713	--	--	--	--	--	--	12/31/2017 00:11:20.105	--	--
83	--	--	--	--	--	--	--	--	--	--	--	01/01/2018 19:49:26.290	--	--
84	01/01/2018 22:37:44.979	--	01/01/2018 22:37:41.713	--	01/01/2018 22:37:41.994	--	--	--	--	--	--	01/01/2018 22:37:40.358	--	--
85	--	--	01/02/2018 05:36:21.796	01/02/2018 05:36:21.015	01/02/2018 05:36:22.064	--	--	--	--	--	--	01/02/2018 05:36:20.470	--	--
86	--	--	--	--	--	--	--	--	--	--	--	01/08/2018 04:44:57.414	--	--
87	--	--	--	--	--	--	--	--	--	--	--	01/09/2018 18:01:09.916	--	--
88	--	--	--	--	--	--	--	--	--	--	--	01/11/2018 10:15:28.417	--	--

† Event used as a template for aftershock detection.

‡ Event detected by Kim et al. (2018).

Table A1.2: Table of S-picks for detected aftershocks to the M4.2 Delaware 30 November 2017 mainshock.

Index	DVN1	DVN2	DVN3	DVN4	DVN5	DVN12	DVN13	DVN14	DVN15	DVN16	DVB1	DVB2	DVB3	DVB4
1	--	--	12/01/2017 21:41:38.459	--	--	--	--	--	--	--	--	12/01/2017 21:41:36.124	--	--
2	--	--	--	--	--	--	--	--	--	--	--	12/01/2017 21:59:53.774	--	--
3	--	--	12/01/2017 23:27:36.464	--	--	--	--	--	--	--	--	12/01/2017 23:27:34.321	--	--
4	--	--	--	--	--	--	--	--	--	--	--	12/02/2017 00:16:09.310	--	--
5	--	--	--	--	--	--	--	--	--	--	--	12/02/2017 00:24:33.714	--	--
6	--	--	12/02/2017 00:57:44.773	--	--	--	--	--	--	--	--	12/02/2017 00:57:42.479	--	--
7	--	--	--	--	--	--	--	--	--	--	--	12/02/2017 03:12:15.942	--	--
8	--	--	12/02/2017 10:24:49.022	--	12/02/2017 10:24:49.612	--	--	--	--	--	--	12/02/2017 10:24:46.988	--	--
9	--	--	--	--	--	--	--	--	--	--	--	12/02/2017 12:39:22.744	--	--
10	--	--	12/02/2017 14:36:19.102	12/02/2017 14:36:17.653	12/02/2017 14:36:19.384	--	--	--	--	--	--	12/02/2017 14:36:16.722	--	--
11	--	--	--	--	--	--	--	--	--	--	--	12/02/2017 16:33:17.771	--	--
12	--	--	--	--	--	--	--	--	--	--	--	12/02/2017 16:57:40.922	--	--
13	--	--	12/02/2017 18:38:47.886	12/02/2017 18:38:46.482	12/02/2017 18:38:48.195	--	--	--	--	--	--	12/02/2017 18:38:45.407	--	--
14	--	--	--	--	--	--	--	--	--	--	--	12/02/2017 19:13:17.079	--	--
15	--	--	--	--	--	--	--	--	--	--	--	12/03/2017 01:24:00.198	--	--
16	--	--	--	--	--	--	--	--	--	--	--	12/03/2017 14:25:07.974	--	--
17	--	--	--	--	--	--	--	--	--	--	--	12/03/2017 14:38:38.698	--	--
18	--	--	12/04/2017 02:31:31.373	12/04/2017 02:31:29.966	12/04/2017 02:31:30.156	--	--	--	--	--	--	12/04/2017 02:31:28.922	--	--
19	--	--	--	--	--	--	--	--	--	--	--	12/04/2017 08:41:29.549	--	--

20	--	--	--	--	--	--	--	--	--	--	--	12/04/2017 09:24:20.226	--	--
21	--	--	--	--	--	--	--	--	--	--	--	12/04/2017 12:13:41.580	--	--
22	--	--	--	--	--	--	--	--	--	--	--	12/04/2017 19:10:39.219	--	--
23	--	--	12/05/2017 01:24:03.957	--	--	--	--	--	--	--	--	12/05/2017 01:24:01.616	--	--
24	--	--	--	--	--	--	--	--	--	--	--	12/05/2017 10:24:25.782	--	--
25	--	--	--	--	--	--	--	--	--	--	--	12/05/2017 13:31:12.751	--	--
26	--	--	--	--	--	--	--	--	--	--	--	12/05/2017 22:23:36.573	--	--
27	--	--	--	--	--	--	--	--	--	--	--	12/06/2017 03:30:11.289	--	--
28	--	--	--	--	--	--	--	--	--	--	--	12/06/2017 13:55:13.488	--	--
29	--	--	--	--	--	--	--	--	--	--	--	12/07/2017 00:09:29.747	--	--
30	--	--	12/07/2017 00:44:06.040	12/07/2017 00:44:04.607	--	--	--	--	--	--	--	12/07/2017 00:44:03.677	--	--
31	--	--	--	12/07/2017 01:49:09.399	--	--	--	--	--	--	--	12/07/2017 01:49:08.443	--	--
32	--	--	--	--	--	--	--	--	--	--	--	12/07/2017 01:54:50.664	--	--
33	--	--	--	--	--	--	--	--	--	--	--	12/07/2017 10:33:45.413	--	--
34	--	--	12/07/2017 18:53:56.672	--	12/07/2017 18:53:57.822	--	--	--	--	--	--	12/07/2017 18:53:54.898	--	--
35	--	--	12/07/2017 19:39:44.039	12/07/2017 19:39:42.601	--	--	--	--	--	--	--	12/07/2017 19:39:41.575	--	--
36	--	--	--	--	--	--	--	--	--	--	--	12/08/2017 06:14:12.612	--	--
37	--	--	12/08/2017 12:17:53.155	--	12/08/2017 12:17:53.442	--	--	--	--	--	--	12/08/2017 12:17:50.709	--	--
38	--	--	12/08/2017 14:19:54.140	--	12/08/2017 14:19:54.344	--	--	--	--	--	--	12/08/2017 14:19:51.611	--	--
39	--	--	12/09/2017 19:27:03.306	12/09/2017 19:27:02.157	--	--	--	--	--	--	--	12/09/2017 19:27:01.045	--	--
40	--	--	12/09/2017 20:26:22.889	--	--	--	--	--	--	--	--	12/09/2017 20:26:20.592	--	--

41	--	--	--	--	--	--	--	--	--	--	--	12/10/2017 20:17:25.845	--	--
42	--	--	--	--	--	--	--	--	--	--	--	12/11/2017 05:45:07.462	--	--
43	--	--	--	--	--	--	--	--	--	--	--	12/11/2017 20:11:45.301	--	--
44	--	--	12/11/2017 22:02:43.473	12/11/2017 22:02:42.854	--	12/11/2017 22:02:48.966	--	12/11/2017 22:02:47.066	--	--	--	12/11/2017 22:02:41.952	12/11/2017 22:02:46.590	12/11/2017 22:02:49.741
45	--	--	--	--	--	--	--	--	--	--	--	12/11/2017 23:42:05.939	--	--
46	--	--	--	--	--	--	--	--	--	--	--	12/12/2017 04:24:59.772	--	--
47	--	--	--	--	--	--	--	--	--	--	--	12/12/2017 07:20:37.662	--	--
48	--	--	12/13/2017 00:45:29.000	12/13/2017 00:45:27.507	12/13/2017 00:45:29.262	--	--	12/13/2017 00:45:31.747	--	12/13/2017 00:45:36.469	--	12/13/2017 00:45:26.563	12/13/2017 00:45:31.190	12/13/2017 00:45:34.191
49	--	--	--	--	--	--	--	--	--	--	--	12/13/2017 13:58:13.135	--	--
50	--	--	--	--	--	--	--	--	--	--	--	12/13/2017 22:03:40.893	--	--
51	--	--	--	--	--	--	--	--	--	--	--	12/14/2017 02:14:51.498	--	--
52	--	--	--	--	--	--	--	--	--	--	--	12/14/2017 08:13:40.086	--	--
53	--	--	--	12/14/2017 13:50:57.087	--	--	--	--	--	--	--	12/14/2017 13:50:32.489	--	--
54	--	--	--	--	--	--	--	--	--	--	--	12/14/2017 17:50:53.644	--	--
55	--	--	--	--	--	--	--	--	--	--	--	12/14/2017 21:56:09.468	--	--
56	12/14/2017 23:09:59.499	--	--	12/14/2017 23:09:53.599	--	--	--	--	--	--	--	12/14/2017 23:09:52.630	--	--
57	--	--	--	--	--	--	--	--	--	--	--	12/15/2017 00:47:54.520	--	--
58	--	--	--	--	--	--	--	--	--	--	--	12/15/2017 01:54:20.305	--	--
59	--	--	12/15/2017 07:24:14.071	--	--	--	--	--	--	--	--	12/15/2017 07:24:12.130	--	--
60	--	--	--	--	--	--	--	--	--	--	--	12/15/2017 22:20:47.966	--	--
61	--	--	--	--	--	--	--	--	--	--	--	12/16/2017 01:15:04.730	--	--

62	--	--	--	--	--	--	--	--	--	--	--	12/16/2017 07:29:10.802	--	--
63	--	--	--	--	--	--	--	--	--	--	--	12/16/2017 11:36:00.191	--	--
64	--	--	12/17/2017 14:58:47.669	12/17/2017 14:58:46.226	12/17/2017 14:58:47.919	12/17/2017 14:58:52.272	12/17/2017 14:58:52.103	12/17/2017 14:58:50.388	12/17/2017 14:58:54.954	12/17/2017 14:58:55.034	--	12/17/2017 14:58:45.238	12/17/2017 14:58:49.895	12/17/2017 14:58:53.053
65	--	--	12/17/2017 16:07:09.112	--	12/17/2017 16:07:09.551	12/17/2017 16:07:13.934	--	--	--	--	--	12/17/2017 16:07:06.772	--	12/17/2017 16:07:14.530
66	--	--	--	--	--	--	--	--	--	--	--	12/18/2017 08:37:57.158	--	--
67	--	--	--	--	--	--	--	--	--	--	--	12/18/2017 08:38:06.059	--	--
68	--	--	12/19/2017 10:35:03.995	12/19/2017 10:35:02.736	--	--	--	--	--	--	--	12/19/2017 10:35:01.637	--	--
69	--	--	--	--	--	--	--	--	--	--	--	12/19/2017 13:35:47.340	--	--
70	--	--	12/23/2017 00:57:50.759	12/23/2017 00:57:49.622	12/23/2017 00:57:51.262	--	--	--	--	--	--	12/23/2017 00:57:48.503	--	--
71	--	--	--	--	--	--	--	--	--	--	--	12/23/2017 05:48:53.065	--	--
72	--	--	12/23/2017 13:29:54.570	--	--	--	--	--	--	--	--	12/23/2017 13:29:52.913	--	--
73	--	--	12/23/2017 16:21:56.060	12/23/2017 16:21:54.279	--	--	--	--	--	--	--	12/23/2017 16:21:53.636	--	--
74	--	--	--	--	--	--	--	--	--	--	--	12/24/2017 11:53:10.283	--	--
75	--	--	--	--	--	--	--	--	--	--	--	12/27/2017 13:20:10.343	--	--
76	--	--	12/27/2017 14:11:49.370	12/27/2017 14:11:47.880	--	--	--	--	--	--	--	12/27/2017 14:11:46.889	--	--
77	--	--	12/27/2017 14:32:27.956	--	--	--	--	--	--	--	--	12/27/2017 14:32:25.433	--	--
78	--	--	--	--	--	--	--	--	--	--	--	12/27/2017 23:36:32.336	--	--
79	--	--	--	12/28/2017 05:39:25.907	--	--	--	--	--	--	--	12/28/2017 05:39:24.896	--	--
80	--	--	12/28/2017 09:42:29.618	12/28/2017 09:42:28.217	--	--	--	--	--	--	--	12/28/2017 09:42:27.167	--	--
81	--	--	--	--	--	--	--	--	--	--	--	12/29/2017 06:31:52.470	--	--
82	--	--	12/31/2017 00:11:23.639	12/31/2017 00:11:22.172	12/31/2017 00:11:23.902	--	--	--	--	--	--	12/31/2017 00:11:21.210	--	--

83	--	--	--	--	--	--	--	--	--	--	--	01/01/2018 19:49:27.402	--	--
84	--	--	01/01/2018 22:37:43.826	01/01/2018 22:37:42.425	--	--	--	--	--	--	--	01/01/2018 22:37:41.500	--	--
85	--	--	01/02/2018 05:36:23.912	01/02/2018 05:36:22.517	--	--	--	--	--	--	--	01/02/2018 05:36:21.589	--	--
86	--	--	--	--	--	--	--	--	--	--	--	01/08/2018 04:44:58.578	--	--
87	--	--	--	--	--	--	--	--	--	--	--	01/09/2018 18:01:11.033	--	--
88	--	--	--	--	--	--	--	--	--	--	--	01/11/2018 10:15:29.608	--	--

Appendix 2: Bayesian Markov Chain Monte Carlo Algorithm

The Bayesian MCMC algorithm works iteratively to generate an sequence of samples of potential model parameters, $\{m\}$. After an initial number of steps, N_{BURN} , during which the parameter values bear the imprint of the starting values, the MCMC converges to sample model parameters in proportion to their posterior probability given the observed aftershock magnitudes and timings, *i.e.* $P(\{m\}|\{d\})$. We use this technique to solve for the ensemble of parameters to fit the observed aftershock characteristics using an aftershock rate equation

$$R(t) = \frac{10^{a+b(M_{main}-M_c)}}{(t+c)^p} \quad \text{A.1}$$

in which M_{main} is the magnitude of the mainshock, M_c is the magnitude of completeness, a is the productivity of the sequence, b indicates the relative magnitude distribution of the sequence, c is a time offset before decay, and p is the decay rate.

The likelihood of any observed aftershock, $P(d_i|\{a, b, c, p\})$ is related to the rate equation above and given by:

$$L(a, p) = \sum_{j=1}^{N_d} (a + b(M_{main} - M_{min}) - p \log(t + c)) - \int_{t_1}^{t_{N_d}} 10^{a+b(M_{main}-M_{min})} (t+c)^{-p} dt \quad \text{A.2}$$

The likelihood of an observed sequence, $\{d\}$, of N_d aftershocks, is then given by the product of the individual $P(d_i|\{a, b, c, p\})$. The posterior model probabilities are given by Bayes' theorem:

$$P(\{a, b, c, p\}|\{d\}) \propto P(\{a, b, c, p\}) \prod_{i=1}^{N_d} P(d_i|\{a, b, c, p\}) \quad \text{A.3}$$

Prior knowledge of potential values for the parameters a, b, c , and p is introduced via the *a priori* probability $P(\{a, b, c, p\})$, and determines the bounds used for each parameter in the MCMC modeling, as follows.

a : Productivity. $[-4, 0]$. Derived from Page et al. (2016) estimates of productivity (a -value) for differing regions, particularly for their estimate for Stable Continental Regions (SCR). Across all regions studied, Page et al. (2016) found a -values from -1.97 to -2.98, with SCRs at -2.28. Bounds were left large around any potential value to allow for unknown behavior in this parameter.

b : Relative magnitudes. $\left[\left(1 - \frac{z}{\sqrt{N}}\right)\beta, \left(1 + \frac{z}{\sqrt{N}}\right)\beta\right]$. Derived from Aki (1965) maximum likelihood estimator of the 95% confidence interval for the population b -value (Section 1.2.1, equation 1.4).

c : Time offset. $[t_1-1, t_1+1]$. Derived by determining the time offset in days between the first recorded aftershock and the mainshock, t_1 , and providing a range of possible values +/- 1 day from that time difference.

p : Decay rate. $[0.5, 2]$. Derived from published works on the Omori-Utsu p -exponent, using the widest range reasonable given literature (Ebel, 2009; Shcherbakov et al., 2004; Utsu et al., 1995).

First, an initial model is determined by randomly selecting a value from within the input range for each parameter. The log-likelihood of the model is calculated using equation A.3 and saved as the current value L_0 .

In the MCMC, we select at random which of the four parameters will be perturbed, and a new value for that parameter is generated by perturbing the current value by δv percent, where δv is drawn from a normal distribution, $P(\delta v) = \frac{1}{2\pi} \exp\left(-\frac{\delta v^2}{2\sigma^2}\right)$. The standard deviation, σ , of the model parameter perturbations is set to 0.10 for the smaller data set from Delaware (Chapter 2) and to 0.02 for the larger data set from Oklahoma (Chapter 3).

The log-likelihood is recalculated for the updated parameter value, with the likelihood saved as L_i . This value is then compared to the previous value of L_{i-1} and the proposed (updated) model is accepted with an acceptance probability $\alpha(L_i|L_{i-1})$ given by the Metropolis criterion (Metropolis et al., 1953; Mosegaard & Tarantola, 1995):

$$\alpha(L_i|L_{i-1}) = \begin{cases} 1 & \text{if } L_i > L_{i-1} \\ \exp(L_i - L_{i-1}) & \text{otherwise} \end{cases} \quad \text{A.4}$$

If the proposed transition to state i is accepted, the model parameter values for $\{a, b, c, p\}$ are set to the values proposed in step i . If the proposed transition is rejected, the parameter values remain unchanged from their values at step $i - 1$.

The algorithm is set to run for a total of $N_{STEPS} = 10^6$ steps, with a burn-in period of $N_{BURN} = 10^4$ during which no models are saved to the ensemble. To reduce memory requirements and avoid repetition of very similar (highly correlated) proposed models, only every $N_{THIN} = 100th$ model is saved to the ensemble solution used in subsequent analysis. After all the iterations have been completed and the ensemble has been generated, distributions for each of the four parameters are available and can be examined to determine maximum-likelihood values, posterior mean values, uncertainties, and trade-offs between parameter values. Marginal posterior distributions for each parameter can also be calculated.

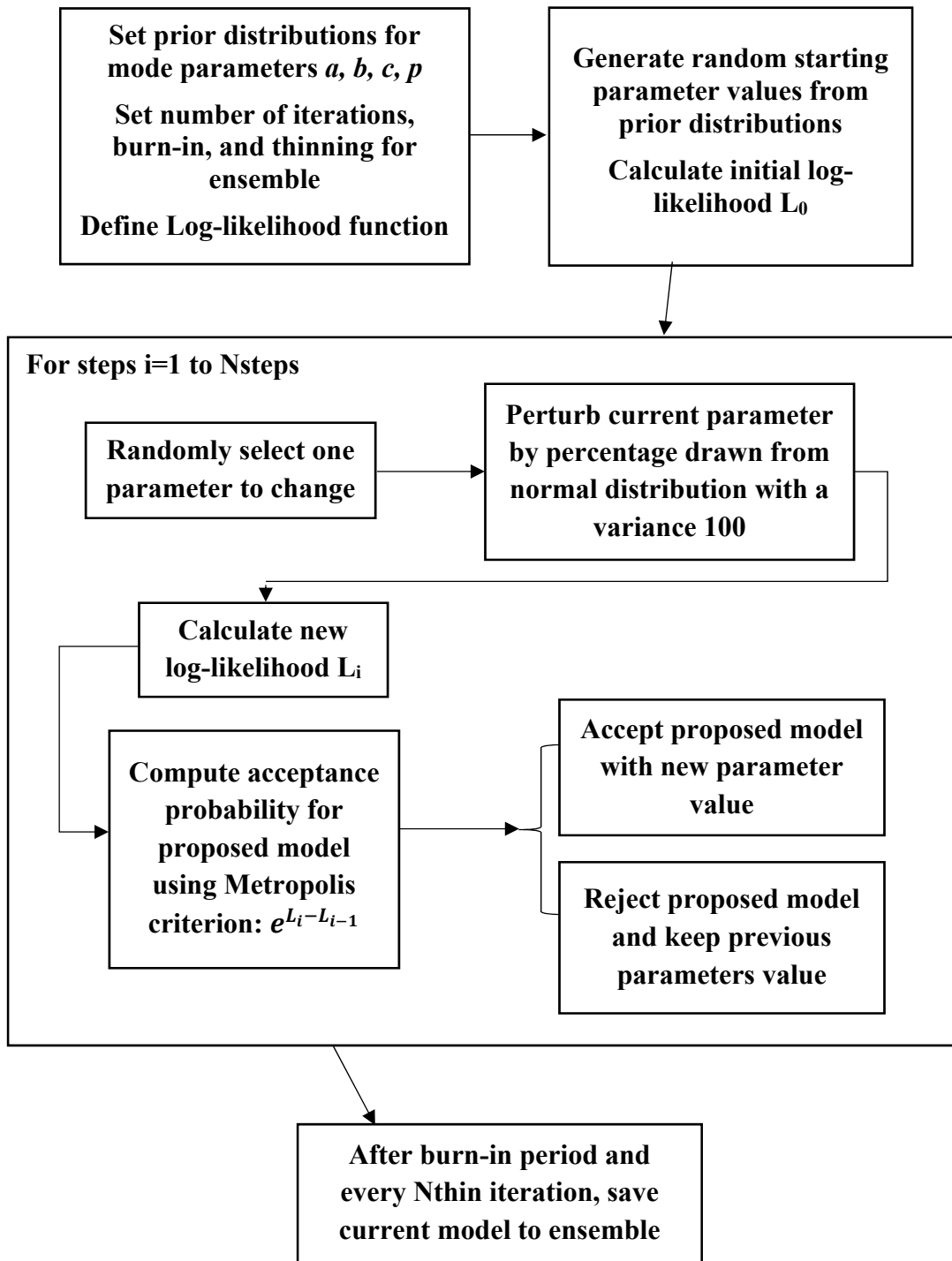


Figure A2.1: Flowchart of MCMC algorithm.

Appendix 3: Synthetic Catalog Generation

Because earthquake timing is generally modeled as a Poisson process (Vidale et al., 1998; Zaliapin et al., 2008), we initially generate random times P from an exponential distribution using a λ_{max} value, corresponding to the maximum rate or smallest interevent time desired. We then compute the cumulative sum of times at each event to build a catalog of event times. This catalog is then thinned to match the growth curve of $\lambda = e^{\alpha+\beta t}$ by generating a uniform random variable U for each catalog event and comparing it to a normalized value for the time of the event. Only when the corresponding uniform random event falls below the rate growth curve is a simulated event from P added to the final simulated exponentially growing catalog. Thus, if $U < \frac{e^{\alpha+\beta P_i}}{\lambda_{max}}$, P_i is added to the simulated catalog for analysis.

The values for the parameters α , β , and λ_{max} used to generate the synthetic catalogs for Chapter 3 are selected based on their fit to the motivating example of increasing seismicity in Oklahoma.

We generate a random oscillating catalog in a similar manner. A catalog Q is randomly generated using the indicated λ_{max} value, and then thinned to follow an oscillation with the desired period, in our case $T=183$ for a semiannual period (Figure 4.4, Section 4.3). A uniform random variable is again generated for each catalog event and compared to a normalized value for the event from Q . When the uniform random event falls below the oscillating rate curve, the simulated event from Q is included in the final simulated

oscillating catalog. Thus, if $U < \frac{\lambda(1+\alpha\cos\cos\frac{2\pi Q_k}{T})}{\lambda_{max}}$, Q_k is added to the simulated catalog for analysis.

Appendix 4: Derivation of Expected Schuster $\ln(p)$ Value

We analytically derive the expected value for the Schuster p -value in the cases where the underlying rate of events is linearly increasing and exponentially increasing, following the manner used by Ader and Avouac (2013) for sinusoidally varying seismicity. In our first situation, we have the linear case as follows:

The normalized increasing seismicity rate will follow the function

$$R(t_k) = 1 + at_k \quad \text{A.1}$$

where t_k is the time for event k in a catalog of N events and a is the rate of increase in seismicity. The probability distribution function for each event t_k , corresponding to one step in the direction $\theta_k = 2\pi \frac{t_k}{T}$ in the Schuster test, is defined as

$$p(t) = \frac{2}{2T + aT^2} (1 + at) \quad \text{A.2}$$

where T is the period being tested. With X and Y defined as the coordinates of the endpoint of the random walk defined by N events, we have

$$X = \sum_{k=1}^N \cos \theta_k \quad \text{and} \quad Y = \sum_{k=1}^N \sin \theta_k \quad \text{A.3}$$

where $\theta_k = (2\pi t_k/T)$. Using these with the above pdf we can determine the expected value for each coordinate in the following manner:

$$\langle X \rangle = \frac{2}{2T + aT^2} \sum_{k=1}^N \int_0^T \cos \left[\frac{2\pi t_k}{T} \right] (1 + at_k) dt_k = 0 \quad \text{A.4}$$

$$\langle Y \rangle = \frac{2}{2T + aT^2} \sum_{k=1}^N \int_0^T \sin \left[\frac{2\pi t_k}{T} \right] (1 + at_k) dt_k = -\frac{aTN}{\pi(2 + aT)} \quad \text{A.5}$$

In order to determine the variance for these coordinates, we calculate the second moments for X and Y , which requires using the following expansion:

$$\left(\sum_{k=1}^N \cos \theta_k \right)^2 = \sum_{k=1}^N (\cos \theta_k)^2 + \sum_{i=1}^N \sum_{j=1}^N \cos \theta_i \cos \theta_j, i \neq j \quad \text{A.6}$$

This can be further decomposed into

$$\sum_{k=1}^N (\cos \theta_k)^2 + \sum_{i=1}^N \sum_{j=1}^N \frac{1}{2} [\cos(\theta_i - \theta_j) + \cos(\theta_i + \theta_j)], i \neq j \quad \text{A.7}$$

This, and its equivalent expression for the square of $Y = \sum_{k=1}^N \sin \theta_k$ allow the following expressions for the second moments of X and Y . We use $\psi = \theta_i - \theta_j$ and $\varphi = \theta_i + \theta_j$ for notation.

$$\begin{aligned} & \sum_{k=1}^N \int (\cos \theta_k)^2 p(\theta_k) d\theta_k \\ & + \frac{1}{2} \sum_{i=1}^N \sum_{j=1}^N \left[\int \cos(\psi) p(\psi) d\psi + \int \cos(\varphi) p(\varphi) d\varphi \right] \end{aligned} \quad \text{A.8}$$

$$\begin{aligned}
& \sum_{k=1}^N \int (\sin \theta_k)^2 p(\theta_k) d\theta_k \\
& + \frac{1}{2} \sum_{i=1}^N \sum_{j=1}^N \left[\int \cos(\psi) p(\psi) d\psi - \int \cos(\varphi) p(\varphi) d\varphi \right]
\end{aligned} \tag{A.9}$$

Unlike the sinusoidal case shown in Ader and Avouac's derivations (2013) where φ and ψ are identical, due to a symmetric pdf for each step in time, for the linearly growing pdf we must solve for each pdf of φ and ψ . Using the cumulative distribution function technique, we find the pdfs for the sum and difference of two random variables with the pdf given in equation A.2 above:

$$\begin{aligned}
& P(\psi): P(X_1 - X_2) \leq \Psi \\
& = \begin{cases} \left(\frac{2}{2T + aT^2} \right)^2 \int_0^{T+\psi} \int_{x_1-\psi}^T (1 + ax_1)(1 + ax_2) dx_2 dx_1, & -T < \psi < 0 \\ 1 - \left(\frac{2}{2T + aT^2} \right)^2 \int_{\psi}^T \int_0^{x_1-\psi} (1 + ax_1)(1 + ax_2) dx_2 dx_1, & 0 < \psi < T \end{cases}
\end{aligned} \tag{A.10}$$

$$p(\psi) = \begin{cases} \frac{2(T + \psi)(6 + 6aT + a^2(2T^2 + T\psi - \psi^2))}{3T^2(2 + aT)^2}, & -T < \psi < 0 \\ \frac{2(T - \psi)(6 + 6aT + a^2(2T^2 - T\psi - \psi^2))}{3T^2(2 + aT)^2}, & 0 < \psi < T \end{cases} \tag{A.11}$$

$$\begin{aligned}
& P(\varphi): P(X_1 + X_2) \leq \Phi \\
& = \begin{cases} \left(\frac{2}{2T + aT^2} \right)^2 \int_0^{\varphi} \int_0^{\varphi-x_1} (1 + ax_2)(1 + ax_1) dx_2 dx_1, & 0 < \varphi < T \\ 1 - \left(\frac{2}{2T + aT^2} \right)^2 \int_{\varphi-T}^T \int_{\varphi-x_1}^T (1 + ax_2)(1 + ax_1) dx_2 dx_1, & T < \varphi < 2T \end{cases}
\end{aligned} \tag{A.12}$$

$$p(\varphi) = \begin{cases} \frac{2\varphi(6 + 6a\varphi + a^2\varphi^2)}{3T^2(2 + aT)^2}, & 0 < \varphi < T \\ -\frac{2(2T - \varphi)(-6 - 6a\varphi + a^2(2T^2 - 2T\varphi - \varphi^2))}{3T^2(2 + aT)^2}, & T < \varphi < 2T \end{cases} \quad \text{A.13}$$

We then evaluate the second moment of X by substituting in the applicable probability functions from equations A.11 and A.13 with the expansions given in equation A.8 and the fact that all angles are equal to $2\pi \frac{t_k}{T}$ in order to evaluate each integral component.

$$\begin{aligned} \langle X^2 \rangle &= \sum_{k=1}^N \int_0^T \left(\cos \frac{2\pi t_k}{T} \right)^2 (1 + at_k) dt_k + \quad \text{A.14} \\ &\frac{1}{2} \sum_{i=1}^N \sum_{j=1}^N \left[\int_{-T}^0 \cos \left[\frac{2\pi\psi}{T} \right] \left(\frac{2(T + \psi)(6 + 6aT + a^2(2T^2 + T\psi - \psi^2))}{3T^2(2 + aT)^2} \right) d\psi \right. \\ &\quad + \int_0^T \cos \left[\frac{2\pi\psi}{T} \right] \left(\frac{2(T - \psi)(6 + 6aT + a^2(2T^2 - T\psi - \psi^2))}{3T^2(2 + aT)^2} \right) d\psi \\ &\quad + \int_0^T \cos \left[\frac{2\pi\varphi}{T} \right] \left(\frac{2\varphi(6 + 6a\varphi + a^2\varphi^2)}{3T^2(2 + aT)^2} \right) d\varphi \\ &\quad \left. + \int_T^{2T} \cos \left[\frac{2\pi\varphi}{T} \right] \left(-\frac{2(2T - \varphi)(-6 - 6a\varphi + a^2(2T^2 - 2T\varphi - \varphi^2))}{3T^2(2 + aT)^2} \right) d\varphi \right] \end{aligned}$$

$$\langle X^2 \rangle = \frac{N}{2} + \frac{N(N-1)}{2} \left[\left(\frac{a^2T^2}{2\pi^2(2+aT)^2} - \frac{a^2T^2}{2\pi^2(2+aT)^2} \right) + \left(\frac{aT(4+aT)}{2\pi^2(2+aT)^2} - \frac{aT(4+3aT)}{2\pi^2(2+aT)^2} \right) \right] \quad \text{A.15}$$

$$\langle X^2 \rangle = \frac{N}{2} \quad \text{A.16}$$

Similarly we use the probability functions from equations A.11 and A.13 with the expansions given in equations A.9 and A.8 for to solve for the second moment of Y :

$$\langle Y^2 \rangle = \frac{N}{2} + \frac{N(N-1)}{2} \left[\left(\frac{a^2 T^2}{2\pi^2(2+aT)^2} - \frac{a^2 T^2}{2\pi^2(2+aT)^2} \right) - \left(\frac{aT(4+aT)}{2\pi^2(2+aT)^2} - \frac{aT(4+3aT)}{2\pi^2(2+aT)^2} \right) \right] \quad \text{A.17}$$

$$\langle Y^2 \rangle = \frac{N}{2} + \frac{N(N-1)}{2} \frac{2a^2 T^2}{\pi^2(2+aT)^2} \quad \text{A.18}$$

The variance for each coordinate can then be obtained easily using the relation between first and second moments (equations A.4, A.5, A.16, and A.18).

$$\text{Var}(X) = \langle X^2 \rangle - \langle X \rangle^2 = \frac{N}{2} \quad \text{A.19}$$

$$\text{Var}(Y) = \frac{N}{2} + \frac{N(N-1)}{2} \frac{2a^2 T^2}{\pi^2(2+aT)^2} - \frac{N^2 a^2 T^2}{\pi^2(2+aT)^2} \quad \text{A.20}$$

$$\text{Var}(Y) = \frac{N}{2} - N \left[\frac{a^2 T^2}{\pi^2(2+aT)^2} \right] \quad \text{A.21}$$

We generated 1000 simulated linearly increasing catalogs at each of a range of potential periods T . For each simulated event, a phase angle is determined in the same manner as above, and the coordinates for the end walk are defined in the same manner as the sum of the cosines and sines of those angles. We compared the expected analytical values for $\langle X \rangle$, $\langle Y \rangle$, σ_X , and σ_Y , which depend on the catalog length N , with the mean and standard deviation of the simulated coordinates X and Y . The resulting distributions of simulated and analytical values are presented in Figure A3.1.

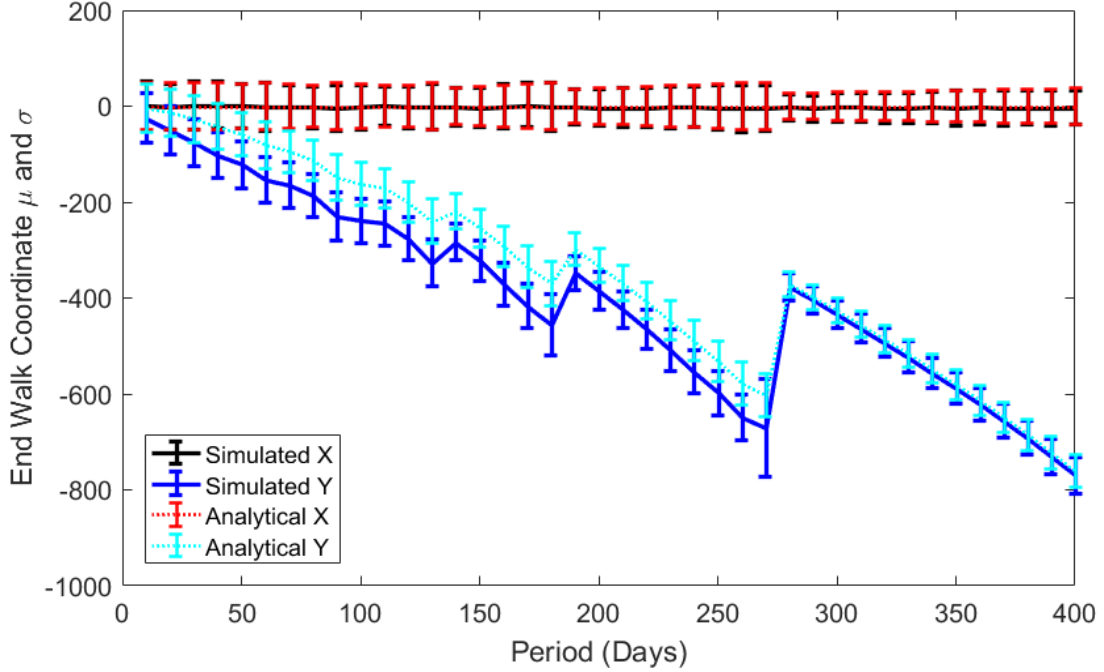


Figure A3.1: Comparison of means and standard deviations observed in simulated linearly increasing catalogs with those derived analytically and calculated for the applicable period and catalog length tested. The “zig-zag” feature seen here is an artifact of the event times included fitting to include only an integer number of cycles of T for each period tested. Therefore, as the catalog becomes long enough such that $\text{mod}(t/T)$ fits another complete cycle, the endpoint Y of the random walk becomes more predictable.

The simulations confirm our analytical solutions and allow us to show the expected

value for the Schuster p -value, which was previously defined as $p = e^{-\frac{D^2}{N}}$. Using the

fact that $\langle D^2 \rangle = \langle X^2 \rangle + \langle Y^2 \rangle$, we have

$$\langle \ln p \rangle = \frac{-1}{N} \left(\frac{N}{2} + \frac{N}{2} + N(N-1) \left[\frac{a^2 T^2}{\pi^2 (2 + aT)^2} \right] \right) \quad \text{A.22}$$

$$\langle \ln p \rangle = -1 - \frac{(N-1)a^2 T^2}{\pi^2 (2 + aT)^2} \quad \text{A.23}$$

In the case of a strictly periodic catalog as demonstrated by Ader and Avouac, the expected probability was a function solely of the amplitude of oscillation α and of the

catalog size N . In the case of a linearly increasing rate, the Schuster test probability will be a function not only of N and the rate of increase a , but also of the square of the period being tested. This can be related to the significant upward tail observed for longer periods tested on a non-homogeneous catalog.

...

We can follow the same method of derivation to obtain the first and second moments for the X and Y coordinates when the seismicity rate is growing exponentially, following

$$R(t_k) = e^{(\alpha + \beta t_k)} \quad \text{A.24}$$

We therefore have the first moments, or expected value for X and Y are:

$$\langle X \rangle = \frac{NT^2\beta^2}{4\pi^2 + T^2\beta^2} \quad \text{A.25}$$

$$\langle Y \rangle = -\frac{2N\pi T\beta}{4\pi^2 + T^2\beta^2} \quad \text{A.26}$$

The second moments will be:

$$\langle X^2 \rangle = \frac{N(8\pi^2 + T^2\beta^2)}{16\pi^2 + T^2\beta^2} + \frac{N(N-1)T^4\beta^4}{(4\pi^2 + T^2\beta^2)^2} \quad \text{A.27}$$

$$\langle Y^2 \rangle = \frac{8N\pi^2}{16\pi^2 + T^2\beta^2} + \frac{4N(N-1)\pi^2 T^2\beta^2}{(4\pi^2 + T^2\beta^2)^2} \quad \text{A.28}$$

which in turn provide the following expressions for the variances:

$$\text{Var}(X) = \frac{16N\pi^4(8\pi^2 + 5T^2\beta^2)}{(4\pi^2 + T^2\beta^2)^2(16\pi^2 + T^2\beta^2)} \quad \text{A.29}$$

$$\text{Var}(Y) = \frac{4N\pi^2(32\pi^4 + T^4\beta^4)}{(4\pi^2 + T^2\beta^2)^2(16\pi^2 + T^2\beta^2)} \quad \text{A.30}$$

We can again compare these analytically derived values for mean and standard deviation to those found by simulating exponentially increasing catalogs, assigning phases, determining the sum of coordinates for the end point of the random walk, and finding the mean and standard deviation of those end points in X and Y for 1000 simulated catalogs, at various values of T . As with the linearly increasing case, the exponentially increasing simulation confirms our derived results (Figure A3.2).

Using the second moments we are able to solve for the expected value of $\langle \ln p \rangle$, the Schuster p -value as before.

$$\langle \ln p \rangle = \frac{-1}{N} \left(\frac{N(4\pi^2 + NT^2\beta^2)}{4\pi^2 + T^2\beta^2} \right) \quad \text{A.31}$$

$$\langle \ln p \rangle = -\frac{4\pi^2 + NT^2\beta^2}{4\pi^2 + T^2\beta^2} \quad \text{A.32}$$

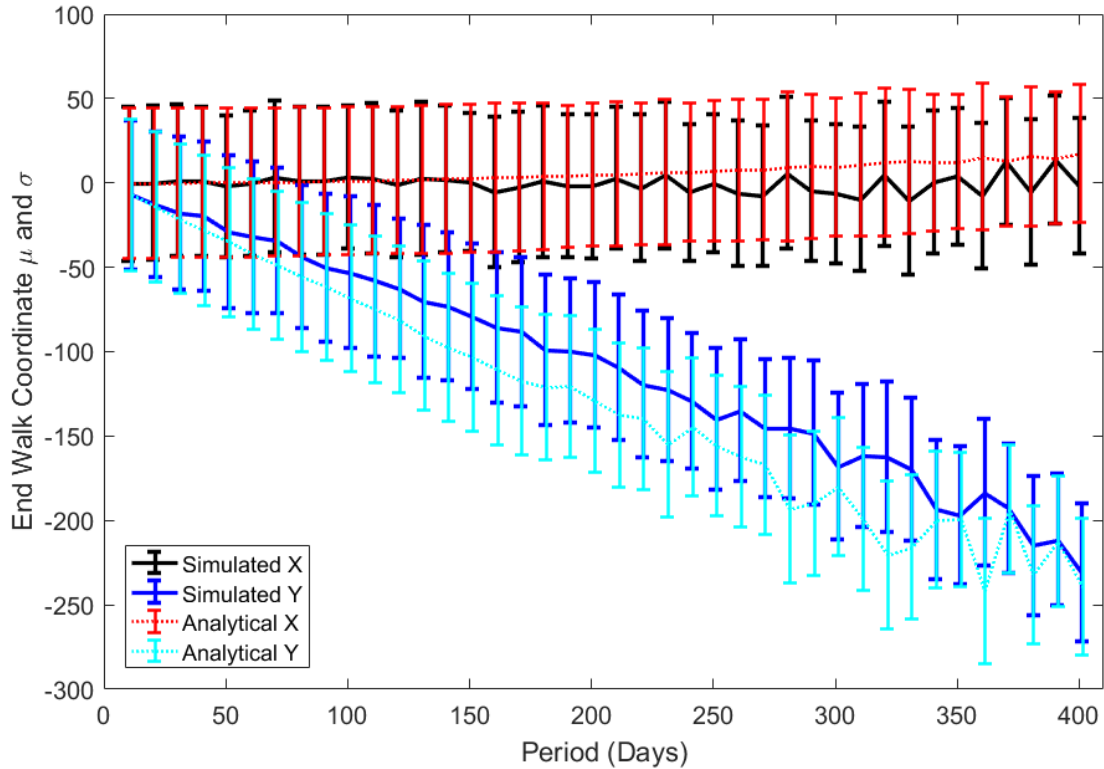


Figure A3.2: Comparison of means and standard deviations observed in simulated exponentially increasing catalogs with those derived analytically and calculated for the applicable period and catalog length tested.

This case presents the same situation as seen with the linearly increasing seismicity rate in equation A.23, in which the expected value grows not only with N and the rate of increase β but also with the square of the period tested, T . This accounts for the significant upward tail observed in the figures such as Figure 4.3, where p -values grow extremely small for larger periods T . For $T < 1$, or when the tested period is shorter than the timescale of the rate change, the catalog size remains the dominant factor in determining the p -value.

...

In principle, we can follow this method of derivation to obtain $\langle \ln p \rangle$ for a case of Omori-Utsu style aftershock decay (Omori, 1895b; Utsu, 1961); however, the hyperbolic form of this rate equation does not have analytical solutions for the first and second moments. Instead, this case can be approached numerically. The rate function for aftershock decay will be of the following form:

$$R(t_j) = \frac{k}{(c + t_j)^p} \quad \text{A.33}$$

where $c > 0$, $k > 0$, and $0.5 < p < 1.5$. This leads to the probability distribution function for each event t_j , corresponding to one step in the direction $\theta_j = 2\pi \frac{t_j}{T}$ in the Schuster test, being defined as:

$$p(t_j) = \left(\frac{1-p}{k(-c^{1-p} + (c+T)^{1-p})} \right) \left(\frac{k}{(c+t_j)^p} \right) \quad \text{A.34}$$

The formulas for the first and second moments used in numerical integration use the definition of X and Y as the endpoints of the random walk as given in equations A.4 and A.5. The first moments are:

$$\langle X \rangle = \left(\frac{1-p}{k(-c^{1-p} + (c+T)^{1-p})} \right) \sum_{j=1}^N \int_0^T \cos \left[\frac{2\pi t_j}{T} \right] \left(\frac{k}{(c+t_j)^p} \right) dt_j \quad \text{A.35}$$

$$\langle Y \rangle = \left(\frac{1-p}{k(-c^{1-p} + (c+T)^{1-p})} \right) \sum_{j=1}^N \int_0^T \sin \left[\frac{2\pi t_j}{T} \right] \left(\frac{k}{(c+t_j)^p} \right) dt_j \quad \text{A.36}$$

and the second moments are:

$$\langle X^2 \rangle = \left(\frac{1-p}{k(-c^{1-p} + (c+T)^{1-p})} \right) \int_0^T \left(\sum_{j=1}^N \cos \left[\frac{2\pi t_j}{T} \right] \right)^2 \left(\frac{k}{(c+t_j)^p} \right) dt_j \quad \text{A.37}$$

$$\langle Y^2 \rangle = \left(\frac{1-p}{k(-c^{1-p} + (c+T)^{1-p})} \right) \int_0^T \left(\sum_{j=1}^N \sin \left[\frac{2\pi t_j}{T} \right] \right)^2 \left(\frac{k}{(c+t_j)^p} \right) dt_j \quad \text{A.38}$$

As before, the expansion from equations A.6 and A.7 can be applied to the second moments. To obtain the probabilities $p(\psi)$ and $p(\varphi)$ we again use the CDF method, using numerical solutions for the following integrals:

$$P(\psi): P(X_1 - X_2) \leq \Psi$$

$$= \begin{cases} \left(\frac{1-p}{k(-c^{1-p} + (c+T)^{1-p})} \right)^2 \int_0^{T+\psi} \int_{x_1-\psi}^T \left(\frac{k}{(c+x_1)^p} \right) \left(\frac{k}{(c+x_2)^p} \right) dx_2 dx_1 \\ \quad -T < \psi < 0 \\ \\ 1 - \left(\frac{1-p}{k(-c^{1-p} + (c+T)^{1-p})} \right)^2 \int_{\psi}^T \int_0^{x_1-\psi} \left(\frac{k}{(c+x_1)^p} \right) \left(\frac{k}{(c+x_2)^p} \right) dx_2 dx_1 \\ \quad 0 < \psi < T \end{cases} \quad \text{A.39}$$

$$P(\varphi): P(X_1 + X_2) \leq \Phi$$

$$= \begin{cases} \left(\frac{1-p}{k(-c^{1-p} + (c+T)^{1-p})} \right)^2 \int_0^{\varphi} \int_0^{\varphi-x_1} \left(\frac{k}{(c+x_1)^p} \right) \left(\frac{k}{(c+x_2)^p} \right) dx_2 dx_1 \\ \quad 0 < \varphi < T \\ \\ 1 - \left(\frac{1-p}{k(-c^{1-p} + (c+T)^{1-p})} \right)^2 \int_{\varphi-T}^T \int_{\varphi-x_1}^T \left(\frac{k}{(c+x_1)^p} \right) \left(\frac{k}{(c+x_2)^p} \right) dx_2 dx_1 \\ \quad T < \varphi < 2T \end{cases} \quad \text{A.40}$$

We can then numerically solve the resultant integrals for the moment expansion, using the $p(\psi)$ and $p(\varphi)$ just obtained and $p(\theta)$ from equation A.34.

References

- 110th Congress. Energy Independence and Security Act of 2007 (2007).
- 111th Congress. American Recovery and Reinvestment Act of 2009 (2009).
Retrieved from <https://www.gpo.gov/fdsys/pkg/BILLS-111hr1enr/pdf/BILLS-111hr1enr.pdf>
- Ader, T. J., & Avouac, J.-P. (2013). Detecting periodicities and declustering in earthquake catalogs using the Schuster spectrum, application to Himalayan seismicity. *Earth and Planetary Science Letters*, 377–378, 97–105.
<https://doi.org/10.1016/j.epsl.2013.06.032>
- Aftershock Forecast Overview. (n.d.). Retrieved January 3, 2021, from <https://earthquake.usgs.gov/data/oaf/overview.php>
- Aki, K. (1965). Maximum likelihood estimate of b in the formula $\log N = a - bM$ and its confidence limits. *Bulletin of the Earthquake Research Institute*, 43, 237–239.
- Allmann, B. P., & Shearer, P. M. (2007). Spatial and temporal stress drop variations in small earthquakes near Parkfield, California. *Journal of Geophysical Research: Solid Earth*, 112(4), 1–17. <https://doi.org/10.1029/2006JB004395>
- Allmann, B. P., & Shearer, P. M. (2009). Global variations of stress drop for moderate to large earthquakes. *Journal of Geophysical Research: Solid Earth*, 114(1), 1–22. <https://doi.org/10.1029/2008JB005821>
- Alt, R. C., & Zoback, M. D. (2017). In situ stress and active faulting in Oklahoma. *Bulletin of the Seismological Society of America*, 107(1), 216–228.
<https://doi.org/10.1785/0120160156>
- Baker, T. (2015). Media Advisory - Oil and Gas Disposal Well Volume Reduction Plan. Oklahoma City, OK: Oklahoma Corporation Commission. Retrieved from www.occeweb.com
- Båth, M. (1965). Lateral inhomogeneities of the upper mantle. *Tectonophysics*, 2(6), 483–514. [https://doi.org/10.1016/0040-1951\(65\)90003-X](https://doi.org/10.1016/0040-1951(65)90003-X)
- Birhanu, Y., Wilks, M., Biggs, J., Kendall, J. M., Ayele, A., & Lewi, E. (2018). Seasonal patterns of seismicity and deformation at the Alutu geothermal reservoir, Ethiopia, induced by hydrological loading. *Journal of Volcanology and Geothermal Research*, 356, 175–182.
<https://doi.org/10.1016/j.jvolgeores.2018.03.008>

- Boese, C. M., Wotherspoon, L., Alvarez, M., & Malin, P. (2015). Analysis of anthropogenic and natural noise from multilevel borehole seismometers in an urban environment, Auckland, New Zealand. *Bulletin of the Seismological Society of America*, *105*(1), 285–299. <https://doi.org/10.1785/0120130288>
- Braunmiller, J., Nábělek, J. L., & Tréhu, A. M. (2014). A seasonally modulated earthquake swarm near Maupin, Oregon. *Geophysical Journal International*, *197*(3), 1736–1743. <https://doi.org/10.1093/gji/ggu081>
- Brown, D. W., Duchane, D. V., Heiken, G., & Hrisco, V. T. (2012). The Enormous Potential for Hot Dry Rock Geothermal Energy. In *Mining the Earth's Heat: Hot Dry Rock Geothermal Energy* (Vol. XVIII, pp. 17–40). Springer. <https://doi.org/10.1007/978-3-540-67316-3>
- Brune, J. N. (1970). Tectonic stress and the spectra of seismic shear waves from earthquakes. *Journal of Geophysical Research*, *75*(26), 4997–5009.
- Burnham, A., Han, J., Clark, C. E., Wang, M., Dunn, J. B., & Palou-Rivera, I. (2012). Life-cycle greenhouse gas emissions of shale gas, natural gas, coal, and petroleum. *Environmental Science and Technology*, *46*(2), 619–627. <https://doi.org/10.1021/es201942m>
- Chen, K.-C., Chiu, J.-M., & Yang, Y.-T. (1996). Shear-wave velocity of the sedimentary basin in the upper Mississippi embayment using S-to-P converted waves. *Bulletin of the Seismological Society of America*, *86*(3), 848–856.
- Chen, X., Shearer, P. M., & Abercrombie, R. E. (2012). Spatial migration of earthquakes within seismic clusters in Southern California: Evidence for fluid diffusion. *Journal of Geophysical Research: Solid Earth*, *117*(4), 1–7. <https://doi.org/10.1029/2011JB008973>
- Chen, X., Nakata, N., Pennington, C., Haffener, J., Chang, J. C., He, X., Zhan, Z., Ni, S., & Walter, J. I. (2017). The Pawnee earthquake as a result of the interplay among injection, faults and foreshocks. *Scientific Reports*, *7*(4945), 1–18. <https://doi.org/10.1038/s41598-017-04992-z>
- Choy, G. L., Rubinstein, J. L., Yeck, W. L., McNamara, D. E., Mueller, C. S., & Boyd, O. S. (2016). A Rare Moderate-Sized (M w 4.9) Earthquake in Kansas: Rupture Process of the Milan, Kansas, Earthquake of 12 November 2014 and Its Relationship to Fluid Injection. *Seismological Research Letters*, *87*(6), 1433–1441. <https://doi.org/10.1785/0220160100>
- Cochran, E. S., Vidale, J. E., & Tanaka, S. (2004). Earth Tides Can Trigger Shallow Thrust Fault Earthquakes. *Science*, *306*, 1164–1166. <https://doi.org/10.1126/science.1103961>

- Cochran, E. S., Skoumal, R. J., McPhillips, D., Ross, Z. E., & Keranen, K. M. (2020). Activation of optimally and unfavourably oriented faults in a uniform local stress field during the 2011 Prague, Oklahoma, sequence. *Geophysical Journal International*, 222(1), 153–168. <https://doi.org/10.1093/gji/ggaa153>
- Console, R., Lombardi, A. M., Murru, M., & Rhoades, D. (2003). Båth's law and the self-similarity of earthquakes. *Journal of Geophysical Research: Solid Earth*, 108(B2). <https://doi.org/10.1029/2001jb001651>
- Daniels, C., Peng, Z., Wu, Q., Ni, S., Meng, X., Yao, D., Wagner, L. S., & Fischer, K. M. (2019). The 15 February 2014 Mw 4.1 South Carolina earthquake sequence: Aftershock productivity, hypocentral depths, and stress drops. *Seismological Research Letters*, 91(1), 452–464. <https://doi.org/10.1785/0220190034>
- Dreiling, J., Isken, M. P., & Mooney, W. D. (2017). Comparison of synthetic pseudoabsolute response spectral acceleration (PSA) for four crustal regions within central and Eastern North America (CENA). *Bulletin of the Seismological Society of America*, 107(1), 169–179. <https://doi.org/10.1785/0120160121>
- Ebel, J. E. (2009). Analysis of aftershock and foreshock activity in stable continental regions: Implications for aftershock forecasting and the Hazard of strong earthquakes. *Seismological Research Letters*, 80(6), 1062–1068. <https://doi.org/10.1785/gssrl.80.6.1062>
- Ellsworth, W. L. (2013). Injection-Induced Earthquakes. *Science*, 341(6142), 1–8. <https://doi.org/10.1126/science.1225942>
- Ellsworth, W. L., Imanishi, K., Luetgert, J. H., Kruger, J., & Hamilton, J. (2011). The Mw 5.8 Virginia Earthquake of August 23, 2011 and its Aftershocks: A Shallow High Stress Drop Event. In *AGU Fall Meeting Abstracts* (Vol. 2011, pp. S14B-05). AA(USGS, Menlo Park, CA, USA;), AB(Geological Survey of Japan, AIST, Tsukuba, Japan;), AC(USGS, Menlo Park, CA, USA;), AD(USGS, Menlo Park, CA, USA;), AE(USGS, Menlo Park, CA, USA;). Retrieved from <https://ui.adsabs.harvard.edu/abs/2011AGUFM.S14B..05E>
- van der Elst, N. J., Page, M. T., Weiser, D. A., Goebel, T. H. W., & Hosseini, S. M. (2016). Induced earthquake magnitudes are as large as (statistically) expected. *Journal of Geophysical Research: Solid Earth*, 121, 4575–4590. <https://doi.org/10.1002/2016JB012818>
- van der Elst, N. J., Hardebeck, J. L., & Michael, A. J. (2020). *Potential duration of aftershocks of the 2020 southwestern Puerto Rico earthquake*. U.S. Geological Survey Open-File Report 2020-1009. Retrieved from <https://doi.org/10.3133/ofr20201009>

- Event Page M4.1 - 9km ENE of Dover, Delaware. (n.d.). Retrieved December 4, 2020, from <https://earthquake.usgs.gov/earthquakes/eventpage/us1000bjkn/executive#executive>
- Felzer, K. R., Becker, T. W., Abercrombie, R. E., Ekström, G., & Rice, J. R. (2002). Triggering of the 1999 Mw 7.1 Hector Mine earthquake by aftershocks of the 1992 Mw 7.3 Landers earthquake. *Journal of Geophysical Research*, *107*(B9), ESE 6-1-ESE 6-13. <https://doi.org/10.1029/2001jb000911>
- Field, E. H., Jordan, T. H., Jones, L. M., Michael, A. J., Blanpied, M. L., Abrahamson, N., Ackerman, S., Barnes, J., Bostrom, A., Campbell, K. W., Earle, P., Fitzenz, D., Gerstenberger, M., Hardebeck, J. L., Holland, A. A., Jaiswal, K., Lackey, C., Lissade, H., Luco, N., et al. (2016). The potential uses of operational earthquake forecasting. *Seismological Research Letters*, *87*(2A), 313–322. <https://doi.org/10.1785/0220150174>
- Frank, W. B., & Abercrombie, R. E. (2018). Adapting the matched-filter search to a wide-aperture network: An aftershock sequence and an earthquake swarm in Connecticut. *Bulletin of the Seismological Society of America*, *108*(1), 524–532. <https://doi.org/10.1785/0120170190>
- French, M. E., Zhu, W., & Banker, J. (2016). Fault slip controlled by stress path and fluid pressurization rate. *Geophysical Research Letters*, *43*(9), 4330–4339. <https://doi.org/10.1002/2016GL068893>
- Frohlich, C., DeShon, H. R., Stump, B., Hayward, C., Hornbach, M., & Walter, J. I. (2016). A Historical Review of Induced Earthquakes in Texas. *Seismological Research Letters*, *87*(4), 1022–1038. <https://doi.org/10.1785/0220160016>
- Gardner, T. W. (1989). Neotectonism along the Atlantic passive continental margin: A review. *Geomorphology*, *2*(1–3), 71–97. [https://doi.org/10.1016/0169-555X\(89\)90007-X](https://doi.org/10.1016/0169-555X(89)90007-X)
- Gibbons, S. J., & Ringdal, F. (2006). The detection of low magnitude seismic events using array-based waveform correlation. *Geophysical Journal International*, *165*(1), 149–166. <https://doi.org/10.1111/j.1365-246X.2006.02865.x>
- Goebel, T. H. W., Rosson, Z., Brodsky, E. E., & Walter, J. I. (2019). Aftershock deficiency of induced earthquake sequences during rapid mitigation efforts in Oklahoma. *Earth and Planetary Science Letters*, *522*, 135–143. <https://doi.org/10.1016/j.epsl.2019.06.036>
- Green, D. N., Bastow, I. D., Dashwood, B., & Nippres, S. E. J. (2017). Characterizing broadband seismic noise in Central London. *Seismological Research Letters*, *88*(1), 113–124. <https://doi.org/10.1785/0220160128>

- Greig, D. W., Yenier, E., Baturan, D., & Karimi, S. (2018). Determination of local magnitude distance corrections for Northern Oklahoma. *Seismological Research Letters*, *89*(5), 1786–1795. <https://doi.org/10.1785/0220170225>
- Gridded Population of the World, Version 4 (GPWv4): Population Density, Revision 11. (2018).
- Groos, J. C., & Ritter, J. R. R. (2009). Time domain classification and quantification of seismic noise in an urban environment. *Geophysical Journal International*, *179*(2), 1213–1231. <https://doi.org/10.1111/j.1365-246X.2009.04343.x>
- Gutenberg, B., & Richter, C. F. (1944). Frequency of earthquakes in California. *Bulletin of the Seismological Society of America*, *34*(4), 185–188.
- Hansen, H. J. (1988). Buried rift basin underlying coastal plain sediments, central Delmarva Peninsula, Maryland. *Geology*, *16*(9), 779–782. [https://doi.org/10.1130/0091-7613\(1988\)016<0779:BRBUCP>2.3.CO;2](https://doi.org/10.1130/0091-7613(1988)016<0779:BRBUCP>2.3.CO;2)
- Hardebeck, J. L. (2010). Aftershocks are well aligned with the background stress field, contradicting the hypothesis of highly heterogeneous crustal stress. *Journal of Geophysical Research: Solid Earth*, *115*(12), 1–10. <https://doi.org/10.1029/2010JB007586>
- Hardebeck, J. L., Llenos, A. L., Michael, A. J., Page, M. T., & van der Elst, N. J. (2019). Updated California aftershock parameters. *Seismological Research Letters*, *90*(1), 262–270. <https://doi.org/10.1785/0220180240>
- Hartzell, S., Mendoza, C., & Zeng, Y. (2013). Rupture model of the 2011 Mineral, Virginia, earthquake from teleseismic and regional waveforms. *Geophysical Research Letters*, *40*(21), 5665–5670. <https://doi.org/10.1002/2013GL057880>
- Hatcher Jr., R. D., Carlson, M. P., McBride, J. H., & Catalán, J. R. M. (2007). Geologic terranes of the south-eastern U. S. In *4-D Framework of Continental Crust* (Memoir 200, p. Plate 1). Geological Society of America. <https://doi.org/https://doi.org/10.1130/MEM200>
- Healy, J. H., Rubey, W. W., Griggs, D. T., & Raleigh, C. B. (1968). The Denver Earthquakes. *Science*, *161*(3848), 1301–1310. <https://doi.org/10.1126/science.161.3848.1301>
- Heaton, T. H. (1975). Tidal triggering of earthquakes. *Geophysical Journal of the Royal Astronomical Society*, *43*(2566), 307–326.
- Heidbach, O., Rajabi, M., Cui, X., Fuchs, K., Müller, B., Reinecker, J., Reiter, K., Tingay, M., Wenzel, F., Xie, F., Ziegler, M. O., Zoback, M. Lou, & Zoback, M. D. (2018). The World Stress Map database release 2016: Crustal stress pattern

- across scales. *Tectonophysics*, 744(April), 484–498.
<https://doi.org/10.1016/j.tecto.2018.07.007>
- Herrmann, R. B. (1979). Surface wave focal mechanisms for eastern North American earthquakes with tectonic implications. *Journal of Geophysical Research*, 84(8), 3543–3552. <https://doi.org/10.1029/JB084iB07p03543>
- Horton, S. (2012). Disposal of hydrofracking waste fluid by injection into subsurface aquifers triggers earthquake swarm in central Arkansas with potential for damaging earthquake. *Seismological Research Letters*, 83(2), 250–260.
<https://doi.org/10.1785/gssrl.83.2.250>
- Hough, S. E. (2012). Initial assessment of the intensity distribution of the 2011 Mw 5.8 Mineral, Virginia, earthquake. *Seismological Research Letters*, 83(4), 649–657. <https://doi.org/10.1785/0220110140>
- Huang, Y., & Beroza, G. C. (2015). Temporal variation in the magnitude-frequency distribution during the Guy-Greenbrier earthquake sequence. *Geophysical Research Letters*, 42, 6639–6646.
<https://doi.org/10.1002/2015GL065170>.Received
- Jones, E. (2018). East vs West Coast Earthquakes. Retrieved June 11, 2021, from <https://www.usgs.gov/media/images/east-vs-west-coast-earthquakes>
- Jónsdóttir, K., Tryggvason, A., Roberts, R., Lund, B., Soosalu, H., & Bödvarsson, R. (2007). Habits of a glacier-covered volcano: Seismicity patterns and velocity structure of Katla volcano, Iceland. *Annals of Glaciology*, 45(2001), 169–177.
<https://doi.org/10.3189/172756407782282499>
- Kanamori, H., & Anderson, D. L. (1975). Theoretical basis of some empirical relations in seismology. *Bulletin of the Seismological Society of America*, 65(5), 1073–1095.
- Kaneko, Y., & Shearer, P. M. (2014). Seismic source spectra and estimated stress drop derived from cohesive-zone models of circular subshear rupture. *Geophysical Journal International*, 197(2), 1002–1015.
<https://doi.org/10.1093/gji/ggu030>
- Keranen, K. M., Savage, H. M., Abers, G. A., & Cochran, E. S. (2013). Potentially induced earthquakes in Oklahoma, USA: Links between wastewater injection and the 2011 Mw5.7 earthquake sequence. *Geology*, 41(6), 699–702.
<https://doi.org/10.1130/G34045.1>
- Keranen, K. M., Weingarten, M., Abers, G. A., Bekins, B. A., & Ge, S. (2014). Sharp increase in central Oklahoma seismicity since 2008 induced by massive wastewater injection. *Science*, 345(6195), 448–451.

<https://doi.org/10.1126/science.1255802>

- Kim, D., & Keranen, K. (2018). Aftershocks of the 2016 Pawnee Earthquake Recorded by a Dense Nodal Array. *AGU Fall Meeting Abstracts, S41C-0554*.
- Kim, W. (1998). The ML Scale in Eastern North America. *Bulletin of the Seismological Society of America, 88*(4), 935–951.
- Kim, W. (2013). Induced seismicity associated with fluid injection into a deep well in Youngstown, Ohio. *Journal of Geophysical Research: Solid Earth, 118*(7), 3506–3518. <https://doi.org/10.1002/jgrb.50247>
- Kim, W., Gold, M., Ramsay, J., Meltzer, A., Wunsch, D., Baxter, S., Lekic, V., Goodling, P., Pearson, K., Wagner, L. S., Roman, D., & Pratt, T. L. (2018). The Mw 4.2 Delaware earthquake of 30 November 2017. *Seismological Research Letters, 89*(6), 2447–2460. <https://doi.org/10.1785/0220180124>
- Knopoff, L. (1964). Earth tides as a triggering mechanism for earthquakes. *Bulletin of the Seismological Society of America, 54*(6), 1865-1870.
- LeTourneau, P. M. (2003). Stratigraphic Architecture and Paleomagnetic Reversal Stratigraphy of the Late Triassic Taylorsville Basin, Virginia and Maryland. *The Great Rift Valleys of Pangea in Eastern North America. Volume 2. Sedimentology, Stratigraphy and Paleontology*, 12–58. Retrieved from <http://www.ldeo.columbia.edu/~letour/research/reprints/letour2003.pdf>
- Levi, M. (2013). Climate consequences of natural gas as a bridge fuel. *Climatic Change, 118*(3–4), 609–623. <https://doi.org/10.1007/s10584-012-0658-3>
- Madariaga, R. (1976). Dynamics of an expanding circular fault. *Bulletin of the Seismological Society of America, 66*(3), 639–666. <https://doi.org/10.1086/622062>
- McGarr, A. F. (2014). Maximum magnitude earthquakes induced by fluid injection. *Journal of Geophysical Research: Solid Earth, 119*, 1008–1019. <https://doi.org/10.1002/2013JB010597>
- McGarr, A. F., & Barbour, A. J. (2017). Wastewater Disposal and the Earthquake Sequences During 2016 Near Fairview, Pawnee, and Cushing, Oklahoma. *Geophysical Research Letters, 44*(18), 9330–9336. <https://doi.org/10.1002/2017GL075258>
- McNamara, D. E., & Buland, R. P. (2004). Ambient noise levels in the continental United States. *Bulletin of the Seismological Society of America, 94*(4), 1517–1527. <https://doi.org/10.1785/012003001>
- Metropolis, N., Rosenbluth, A. W., Rosenbluth, M. N., Teller, A. H., & Teller, E.

- (1953). Equation of state calculations by fast computing machines. *The Journal of Chemical Physics*, 21(6), 1087–1092. <https://doi.org/10.1063/1.1699114>
- Michael, A. J., McBride, S. K., Hardebeck, J. L., Barall, M., Martinez, E., Page, M. T., van der Elst, N. J., Field, E. H., Milner, K. R., & Wein, A. M. (2019). Statistical seismology and communication of the USGS operational aftershock forecasts for the 30 November 2018 Mw 7.1 Anchorage, Alaska, earthquake. *Seismological Research Letters*, 91(1), 153–173. <https://doi.org/10.1785/0220190196>
- Miller, K. G., Browning, J. V., Sugarman, P. J., Monteverde, D. H., Andreasen, D. C., Lombardi, C., Thornburg, J., Fan, Y., & Kopp, R. E. (2017). Lower to mid-Cretaceous sequence stratigraphy and characterization of CO₂ storage potential in the Mid-Atlantic U.S. Coastal Plain. *Journal of Sedimentary Research*, 87(6), 609–629. <https://doi.org/10.2110/jsr.2017.33>
- Mosegaard, K., & Tarantola, A. (1995). Monte Carlo sampling of solutions to inverse problems. *Journal of Geophysical Research*, 100(B7), 12431–12447. <https://doi.org/10.1029/94jb03097>
- Muço, B. (1995). The seasonality of Albanian earthquakes and cross-correlation with rainfall. *Physics of the Earth and Planetary Interiors*, 88(3–4), 285–291. [https://doi.org/10.1016/0031-9201\(94\)02988-N](https://doi.org/10.1016/0031-9201(94)02988-N)
- Nagarajaiah, S., & Erazo, K. (2016). Structural monitoring and identification of civil infrastructure in the United States. *Structural Monitoring and Maintenance*, 3(1), 51–69. <https://doi.org/10.12989/smm.2016.3.1.051>
- Nava, F. A., Márquez-Ramírez, V. H., Zúñiga, F. R., Ávila-Barrientos, L., & Quinteros, C. B. (2017). Gutenberg-Richter b-value maximum likelihood estimation and sample size. *Journal of Seismology*, 21(1), 127–135. <https://doi.org/10.1007/s10950-016-9589-1>
- Olsen, P. E. (1990). Tectonic, Climatic, and Biotic Modulation of Lacustrine Ecosystems - Examples from Newark Supergroup of Eastern North America. In B. Katz (Ed.), *Lacustrine Basin Exploration: Case Studies and Modern Analogs* (pp. 209–224). American Association of Petroleum Geologists.
- Olsson, R. K., Gibson, T. G., Hansen, H. J., & Owens, J. P. (1988). Geology of the northern Atlantic coastal plain: Long Island to Virginia. In R. E. Sheridan & J. A. Grow (Eds.), *The Atlantic Continental Margin: U.S.* (pp. 87–105). Boulder, Colorado: The Geological Society of America.
- Omori, F. (1895a). On the After-shocks of Earthquakes. *The Journal of the College of Science, Imperial University of Tokyo, Japan*, 7, 111–153.

- Omori, F. (1895b). On the aftershocks of earthquakes. *The Journal of the College of Science, Imperial University, Japan*, 7(2), 111–200.
- Page, M. T., van Der Elst, N. J., Hardebeck, J. L., Felzer, K. R., & Michael, A. J. (2016). Three ingredients for improved global aftershock forecasts: Tectonic region, time-dependent catalog incompleteness, and intersequence variability. *Bulletin of the Seismological Society of America*, 106(5), 2290–2301. <https://doi.org/10.1785/0120160073>
- Pazzaglia, F. J., & Gardner, W. (1994). Late Cenozoic flexural deformation of the middle U.S. Atlantic passive margin. *Journal of Geophysical Research*, 99(B6), 12,143–12,157.
- Petersen, M. D., Mueller, C. S., Moschetti, M. P., Hoover, S. M., Llenos, A. L., Ellsworth, W. L., Michael, A. J., Rubinstein, J. L., McGarr, A. F., & Rukstales, K. S. (2016). *2016 One-Year Seismic Hazard Forecast for the Central and Eastern United States from Induced and Natural Earthquakes. U.S. Geological Survey Open-File Report 2016-1035*. <https://doi.org/10.3133/OFR20161035>
- Pratt, T. L. (2018). Characterizing and imaging sedimentary strata using depth-converted spectral ratios: An example from the Atlantic Coastal Plain of the Eastern United States. *Bulletin of the Seismological Society of America*, 108(5A), 2801–2815. <https://doi.org/10.1785/0120180046>
- Pratt, T. L., & Fitzpatrick, J. (2018). East vs West Coast Earthquakes. Retrieved June 11, 2021, from <https://www.usgs.gov/news/east-vs-west-coast-earthquakes>
- Pratt, T. L., Horton, J. W., Muñoz, J., Hough, S. E., Chapman, M. C., & Olgun, C. G. (2017). Amplification of Earthquake Ground Motions in Washington, DC, and Implications for Hazard Assessments in Central and Eastern North America. *Geophysical Research Letters*, 44(24), 12,150–12,160. <https://doi.org/10.1002/2017GL075517>
- Raleigh, C. B., Healy, J. H., & Bredehoeft, J. D. (1976). An Experiment in Earthquake Control at Rangely, Colorado. *Science*, 191(4233), 1230–1237. <https://doi.org/10.1126/science.191.4233.1230>
- Reasenber, P. A., & Jones, L. M. (1989). Earthquake hazard after a mainshock in California. *Science*, 243(4895), 1173–1176. <https://doi.org/10.1126/science.243.4895.1173>
- Richards, P. G., & Hellweg, M. (2020). Challenges and opportunities in turning large U.S. Archives of analog seismograms into a modern usable resource. *Seismological Research Letters*, 91(3), 1531–1541. <https://doi.org/10.1785/0220200053>

- Richter, C. F. (1958). *Elementary seismology*. (J. Gilluly & A. O. Woodford, Eds.), *A Series of books in geology*. San Francisco: W.H. Freeman.
<https://doi.org/10.5408/0022-1368-7.1.21>
- Rubinstein, J. L., & Mahani, A. B. (2015). Myths and Facts on Wastewater Injection, Hydraulic Fracturing, Enhanced Oil Recovery, and Induced Seismicity. *Seismological Research Letters*, *86*(4), 1060–1067.
<https://doi.org/10.1785/0220150067>
- Rubinstein, J. L., La Rocca, M., Vidale, J. E., Creager, K. C., & Wech, A. G. (2008). Tidal modulation of nonvolcanic tremor. *Science*, *319*(5860), 186–189.
<https://doi.org/10.1126/science.1150558>
- Rukstales, K. S., & Petersen, M. D. (2019). Data Release for 2018 Update of the U.S. National Seismic Hazard Model: U.S. Geological Survey data release.
<https://doi.org/https://doi.org/10.5066/P9WT5OVB>
- Saar, M. O., & Manga, M. (2003). Seismicity induced by seasonal groundwater recharge at Mt. Hood, Oregon. *Earth and Planetary Science Letters*, *214*(3–4), 605–618. [https://doi.org/10.1016/S0012-821X\(03\)00418-7](https://doi.org/10.1016/S0012-821X(03)00418-7)
- Schaff, D. P., & Waldhauser, F. (2010). One magnitude unit reduction in detection threshold by cross correlation applied to Parkfield (California) and China seismicity. *Bulletin of the Seismological Society of America*, *100*(6), 3224–3238.
<https://doi.org/10.1785/0120100042>
- Schoenball, M., & Ellsworth, W. L. (2017). Waveform-Relocated Earthquake Catalog for Oklahoma and Southern Kansas Illuminates the Regional Fault Network. *Seismological Research Letters*, *88*(5), 1252–1258.
<https://doi.org/10.1785/0220170083>
- Scholz, C. H., Aviles, C. A., & Wesnousky, S. G. (1985). Scaling differences between large interplate and intraplate earthquakes. *Bulletin of the Seismological Society of America*, *76*(1), 65–70.
- Schorlemmer, D., Wiemer, S., & Wyss, M. (2005). Variations in earthquake-size distribution across different stress regimes. *Nature*, *437*, 539–542.
<https://doi.org/10.1038/nature04094>
- Schultz, R., Stern, V., Novakovic, M., Atkinson, G. M., & Gu, Y. J. (2015). Hydraulic fracturing and the Crooked Lake Sequences: Insights gleaned from regional seismic networks. *Geophysical Research Letters*, *42*, 2750–2758.
<https://doi.org/10.1002/2015GL063455>
- Schuster, A. (1897). On Lunar and Solar Periodicities of Earthquakes. *Proceedings of the Royal Society of London (1854-1905)*, *61*(1), 455–465.

<https://doi.org/10.1098/rspl.1897.0060>

- Shcherbakov, R., & Turcotte, D. L. (2004). A modified form of Båth's law. *Bulletin of the Seismological Society of America*, 94(5), 1968–1975. <https://doi.org/10.1785/012003162>
- Shcherbakov, R., Turcotte, D. L., & Rundle, J. B. (2004). A generalized Omori's law for earthquake aftershock decay. *Geophysical Research Letters*, 31(11), 1–5. <https://doi.org/10.1029/2004GL019808>
- Shcherbakov, R., Turcotte, D. L., & Rundle, J. B. (2005). Aftershock statistics. *Pure and Applied Geophysics*, 162(6–7), 1051–1076. <https://doi.org/10.1007/s00024-004-2661-8>
- Shearer, P. M. (2009). *Introduction to Seismology* (2nd ed.). New York: Cambridge University Press.
- Simpson, J. F. (1967). Earth tides as a triggering mechanism for earthquakes. *Earth and Planetary Science Letters*, 2, 473–478.
- Skoumal, R. J., Brudzinski, M. R., & Currie, B. S. (2015). Earthquakes induced by hydraulic fracturing in Poland township, Ohio. *Bulletin of the Seismological Society of America*, 105(1), 189–197. <https://doi.org/10.1785/0120140168>
- Slinkard, M., Schaff, D. P., Mikhailova, N., Heck, S., Young, C., & Richards, P. G. (2014). Multistation validation of waveform correlation techniques as applied to broad regional monitoring. *Bulletin of the Seismological Society of America*, 104(6), 2768–2781. <https://doi.org/10.1785/0120140140>
- Soto-Cordero, L., Meltzer, A., & Stachnik, J. C. (2018). Crustal structure, intraplate seismicity, and seismic hazard in the mid-Atlantic United States. *Seismological Research Letters*, 89(1), 241–252. <https://doi.org/10.1785/0220170084>
- Spoljaric, N. (1973). Normal faults in basement rocks of the northern coastal plain, Delaware. *Bulletin of the Geological Society of America*, 84(8), 2781–2784. [https://doi.org/10.1130/0016-7606\(1973\)84<2781:NFIBRO>2.0.CO;2](https://doi.org/10.1130/0016-7606(1973)84<2781:NFIBRO>2.0.CO;2)
- Stephenson, W. J., Odum, J. K., Hartzell, S. H., Leeds, A. L., & Williams, R. A. (2021). Shear-Wave Velocity Site Characterization in Oklahoma from Joint Inversion of Multimethod Surface Seismic Measurements: Implications for Central U.S. Ground-Motion Prediction. *Bulletin of the Seismological Society of America*, (Xx). <https://doi.org/10.1785/0120200348>
- Stover, C. W., & Coffman, J. L. (1993). *Seismicity of the United States, 1568-1989*. (R. W. Scott Jr., Ed.) (Revised). Denver: United States Government Printing Office.

- Sumy, D. F., Neighbors, C. J., Cochran, E. S., & Keranen, K. M. (2017). Low stress drops observed for aftershocks of the 2011 Mw 5.7 Prague, Oklahoma, earthquake. *Journal of Geophysical Research: Solid Earth*, *122*(5), 3813–3834. <https://doi.org/10.1002/2016JB013153>
- Thomas, A. M., Nadeau, R. M., & Bürgmann, R. (2009). Tremor-tide correlations and near-lithostatic pore pressure on the deep San Andreas fault. *Nature*, *462*(7276), 1048–1051. <https://doi.org/10.1038/nature08654>
- Thompson, E. M., McBride, S. K., Hayes, G. P., Allstadt, K. E., Wald, L. A., Wald, D. J., Knudsen, K. L., Worden, C. B., Marano, K. D., Jibson, R. W., & Grant, A. R. R. (2019). USGS near-real-time products—and their use—for the 2018 Anchorage earthquake. *Seismological Research Letters*, *91*(1), 94–113. <https://doi.org/10.1785/0220190207>
- Utsu, T. (1961). A statistical study on the occurrence of aftershocks. *Geophysics*, *30*, 521–605.
- Utsu, T., Ogata, Y., & Matsu'ura, R. S. (1995). The Centenary of the Omori Formula for a Decay Law of Aftershock Activity. *J. Phys. Earth*, *43*, 1–33. Retrieved from https://astp.jst.go.jp/modules/search/index.php?page=DocumentDetail&journalId=0022-3743_43_1_The+Centenary+of+the+Omori+Formula+for+a+Decay+Law+of+Aftershock+Activity._N%252FA
- Various. (2021). Advanced National Seismic System (ANSS) Comprehensive Catalog of Earthquake Events and Products. *Earthquake Hazards Program*. U.S. Geological Survey. <https://doi.org/https://doi.org/10.5066/F7MS3QZH>
- Vere-Jones, D. (1969). A note on the statistical interpretation of Bath's law. *Bulletin of the Seismological Society of America*, *59*(4), 1535–1541.
- Vidale, J. E., Agnew, D. C., Johnston, M. J. S., & Oppenheimer, D. H. (1998). Absence of earthquake correlation with Earth tides: An indication of high preseismic fault stress rate. *Journal of Geophysical Research*, *103*(B10), 24567. <https://doi.org/10.1029/98JB00594>
- Walsh, F. R., & Zoback, M. D. (2015). Oklahoma's recent earthquakes and saltwater disposal. *Science Advances*, *1*(5), e1500195–e1500195. <https://doi.org/10.1126/sciadv.1500195>
- Weingarten, M., Ge, S., Godt, J. W., Bekins, B. A., & Rubinstein, J. L. (2015). High-rate injection is associated with the increase in U.S. mid-continent seismicity. *Science*, *348*(6241), 1336–1340. <https://doi.org/10.1126/science.aab1345>

- Whitmeyer, S. J., & Karlstrom, K. E. (2007). Tectonic model for the Proterozoic growth of North America. *Geosphere*, 3(4), 220–259.
<https://doi.org/10.1130/GES00055.1>
- Wiemer, S., & Wyss, M. (2002). Mapping spatial variability of the frequency-magnitude distribution of earthquakes. *Advances in Geophysics*, 45(C).
[https://doi.org/10.1016/S0065-2687\(02\)80007-3](https://doi.org/10.1016/S0065-2687(02)80007-3)
- Withjack, M. O., Schlische, R. W., & Olsen, P. E. (1998). Diachronous rifting, drifting, and inversion on the passive margin of central eastern North America: an analog for other passive margins. *AAPG Bulletin*, 82(5A), 817–835.
<https://doi.org/10.1306/1d9bc60b-172d-11d7-8645000102c1865d>
- Withjack, M. O., Schlische, R. W., Malinconico, M. L., & Olsen, P. E. (2012). Rift-basin development: Lessons from the Triassic-Jurassic Newark Basin of Eastern North America. *Geological Society Special Publication*, 369(1), 301–321.
<https://doi.org/10.1144/SP369.13>
- Wu, Q., & Chapman, M. C. (2017). Stress-drop estimates and source scaling of the 2011 Mineral, Virginia, mainshock and aftershocks. *Bulletin of the Seismological Society of America*, 107(6), 2703–2720.
<https://doi.org/10.1785/0120170098>
- Wu, Q., Chapman, M. C., & Beale, J. N. (2015). The aftershock sequence of the 2011 Mineral, Virginia, earthquake: Temporal and spatial distribution, focal mechanisms, regional stress, and the role of Coulomb stress transfer. *Bulletin of the Seismological Society of America*, 105(5), 2521–2537.
<https://doi.org/10.1785/0120150032>
- Yeck, W. L., Hayes, G. P., McNamara, D. E., Rubinstein, J. L., Barnhart, W. D., Earle, P., & Benz, H. M. (2017). Oklahoma experiences largest earthquake during ongoing regional wastewater injection hazard mitigation efforts. *Geophysical Research Letters*, 44(2), 711–717.
<https://doi.org/10.1002/2016GL071685>
- Yoon, C. E., O'Reilly, O., Bergen, K. J., & Beroza, G. C. (2015). Earthquake detection through computationally efficient similarity search. *Science Advances*, 1, 1–13. <https://doi.org/10.1126/sciadv.1501057>
- Zaliapin, I., Gabrielov, A., Keilis-Borok, V., & Wong, H. (2008). Clustering analysis of seismicity and aftershock identification. *Physical Review Letters*, 101(1), 4–7.
<https://doi.org/10.1103/PhysRevLett.101.018501>
- Zoback, M. Lou, & Zoback, M. D. (1989). Tectonic stress field of the continental United States. In L. C. Pakiser & W. D. Mooney (Eds.), *Geophysical framework of the continental United States* (Memor 172, pp. 523–539). Boulder, Colorado:

